Unlimited Sensing of Multiband Signals

A DISSERTATION PRESENTED
BY
GAL SHTENDEL
TO
THE DEPARTMENT OF ELECTRICAL AND ELECTRONIC ENGINEERING

IN PARTIAL FULFILLMENT OF THE REQUIREMENTS
FOR THE DEGREE OF
DOCTOR OF PHILOSOPHY
IN THE SUBJECT OF
ELECTRICAL AND ELECTRONIC ENGINEERING

IMPERIAL COLLEGE LONDON
LONDON, UK,
OCTOBER 2025

Thesis advisor: Dr Ayush Bhandari Gal Shtendel

Unlimited Sensing of Multiband Signals

Abstract

Analog-to-digital converters (ADCs) underpin modern information systems, where a signal's time and amplitude are quantized. While time quantization can be lossless for certain signal models, amplitude quantization is a bottleneck that limits dynamic range and resolution. The Unlimited Sensing Framework (USF) is a sampling paradigm that reconstructs signals from the quantization error rather than from quantized amplitudes. This leads to high dynamic range (HDR) and high digital resolution (HDRes) acquisition with fewer bits.

This thesis develops the USF for multiband signals, which are sums of narrowband components across a wide spectrum, common in radar, communications, and audio applications. In multiband settings, HDR is crucial to capture both weak and strong signal components, while HDRes is essential for accurate recovery from sub-Nyquist measurements, due to the wide span of the spectral support.

Conceptually, the goal is to exploit the Fourier structure of multiband signals within the USF. However, this is nontrivial: the nonlinear mechanism that enables HDR also distorts the waveform, so the observed sequence is neither bandlimited nor exhibits a simple spectral pattern. This thesis addresses this challenge through theory, algorithm design, and hardware validation. It analyses single- and multi-channel architectures, establishes conditions under which a multiband structure enables stable sub-Nyquist recovery in the USF, and derives corresponding reconstruction methods. Hardware experiments corroborate the theory and demonstrate practical feasibility.

Collectively, the results show that the USF can exploit Fourier structure to enable low-power, HDR, sub-Nyquist sensing architectures. A key advantage is improved effective resolution without increasing bit depth, which is particularly valuable for sub-Nyquist schemes, where fewer measurements demand high-resolution ADCs. The findings have implications for radar, communications, and related systems, bridging the gap between sampling theory and deployable solutions.

Copyright Declaration

The copyright of this thesis rests with the author. Unless otherwise indicated, its contents are licensed under a Creative Commons Attribution-NonCommercial 4.0 International Licence (CC BY-NC).

Under this licence, you may copy and redistribute the material in any medium or format. You may also create and distribute modified versions of the work. This is on the condition that: you credit the author and do not use it, or any derivative works, for a commercial purpose.

When reusing or sharing this work, ensure you make the licence terms clear to others by naming the licence and linking to the licence text. Where a work has been adapted, you should indicate that the work has been changed and describe those changes.

Please seek permission from the copyright holder for uses of this work that are not included in this licence or permitted under UK Copyright Law.

Declaration of Originality

I hereby confirm that the work presented in this thesis is entirely my own and represents original research. All sources of information, including ideas and data from both published and unpublished works of others, have been properly cited and acknowledged. This thesis has not been submitted, nor will it be submitted, to any other academic institution in pursuit of a different degree or qualification.

Contents

1 Introduction and Roadmap **13**
- 1.1 Introduction . . . 14
- 1.2 Research Objectives . . . 19
- 1.3 Thesis Contributions . . . 20
- 1.4 Thesis Outline and a List of Publications . . . 22

2 Background **26**
- 2.1 Analog-to-Digital Conversion . . . 27
- 2.2 Sub-Nyquist Sampling . . . 30
- 2.3 The Unlimited Sensing Framework . . . 40

3 Unlimited Sensing of Bandpass Signals **59**
- 3.1 Introduction and Contributions . . . 60
- 3.2 Towards Computational Demodulation via Modulo Undersampling . . . 62
- 3.3 Theory and Algorithms . . . 65
- 3.4 Experiments . . . 79
- 3.5 Conclusion . . . 84

4 Unlimited Sensing of Multiband Signals **86**
- 4.1 Introduction and Contributions . . . 87
- 4.2 Single-Channel Acquisition and Recovery . . . 91
- 4.3 Multiphase Acquisition and Recovery . . . 100
- 4.4 Conclusion . . . 117

5 Unlimited Sensing for Continuous-wave Time-of-Flight and Second Order Bandpass Sampling **119**
- 5.1 HDR-ToF: HDR Time-of-Flight Imaging via Modulo Acquisition . . . 120
- 5.2 Dual-channel Unlimited Sampling for Bandpass Signals . . . 130

6 Conclusion **141**
6.1 Motivation and Research Problem 141
6.2 Summary of Contributions 143
6.3 Limitations and Scope 144
6.4 Open Problems and Future Work 145

Appendix A **147**

References **150**

List of figures

1.1 Decomposition of high-dynamic-range input signal into quantized signal and quantization noise . . . 15
1.2 The trade-off between dynamic range and digital resolution . . . 16
1.3 The spectrum of a multiband signal . . . 18
1.4 Illustration of the near-far problem . . . 19
1.5 The spectrum of a multiband signal before and after modulo encoding . . . 20
1.6 Four Fourier-structured signal classes that are relevant for this work . . . 21
1.7 Roadmap and contributions of this thesis . . . 22

2.1 The conventional digitization pipeline . . . 27
2.2 Analog-to-digital converters . . . 28
2.3 The effect of timing jitter . . . 29
2.4 High dynamic range and clipped samples . . . 30
2.5 I /Q architecture for demodulation . . . 33
2.6 The allowed sampling rates based on the bandpass sampling theorem . . . 35
2.7 The computation of the baseband function $x(t)$ . . . 36
2.8 Multiband sampling using periodic nonuniform sampling pattern . . . 37
2.9 The modulo acquisition pipeline . . . 42
2.10 The modulo ADC ($\mathscr{M}$ –ADC) . . . 43
2.11 The modulo waveform generated by the $\mathscr{M}$ –ADC for different types of input signals . . . 44
2.12 Quantization process in the $\mathscr{M}$ –ADC . . . 45
2.13 The modulo decomposition property . . . 47
2.14 Illustration of modulo folding by different folding architectures . . . 49
2.15 Time-domain partitioning of modulo samples . . . 52
2.16 Frequency-domain partitioning of modulo samples . . . 57

3.1 The spectrum of a bandpass signal . . . 60
3.2 The existing results in the context of the Unlimited Sensing Framework (USF) 62

3.3 The Fourier-domain representation of a modulo signal 62
3.4 An amplitude modulated signal, its associated modulo signal and undersampled modulo samples 63
3.5 Undersampling demodulates the bandpass spectrum into a lowpass region . 65
3.6 The partitioning of a bandpass signal in the discrete Fourier-domain 75
3.7 Modulo bandpass acquisition and reconstruction pipeline 79
3.8 Reconstruction of a bandpass signal 81
3.9 Reconstruction of a bandpass signal from experimental data ($\mathscr{M}$–ADC) . . 83
3.10 Reconstruction of a bandpass signal from experimental data (generalized $\mathscr{M}$–ADC) 83

4.1 The spectrum of a multiband signal 87
4.2 Downsampling vs. oversampling through the lens of redundancy 89
4.3 Achievable and unachievable sampling rates under the Unlimited Sensing Framework as a function of the maximum frequency f_{U}. 95
4.4 Reconstruction of a multiband signal 99
4.5 Reconstruction performance under additive noise 100
4.6 Multiband Signal Model and the Unlimited Sensing Framework-Multiband (USF-MB) Acquisition Pipeline 101
4.7 $\mathscr{M}$–ADC hardware prototype 115
4.8 Hardware experiment: weak-strong mixtures 116

5.1 An illustration of the probing and the back-scattered waveforms in a continuous wave time-of-flight sensor 122
5.2 The sampling pipeline of conventional and HDR continuous-wave time-of-flight sensor 123
5.3 3D imaging from simulated Time-of-Flight (ToF) measurements 128
5.4 The spectrum of a bandpass signal and valid sampling rates 130
5.5 The acquisition and reconstruction pipeline of the proposed dual-channel bandpass sampling architecture 131
5.6 Reconstruction of a bandpass signal 138

Abbreviations

HDR	High Dynamic Range
HDRes	High Digital Resolution
ADC	Analog-to-Digital Converter
USF	Unlimited Sensing Framework
$\mathscr{M}$**–ADC**	Modulo Analog-to-Digital Converter
US-Alg	The Unlimited Sensing Algorithm
SO-BPS	Second-order Bandpass Sampling
USF-MB	Unlimited Sensing Framework-Multiband
PNS	Periodic Nonuniform Sampling
FT	Fourier-transform
DTFT	Discrete-time Fourier-transform
DFT	Discrete Fourier-transform
FS	Fourier series
ToF	Time-of-Flight
FMCW	Frequency-Modulated Continuous-Wave
MRI	Magnetic resonance Imaging
FBM	Four-Bucket Method
RF	Radio Frequency
MSE	Mean Squared Error

Notations

$\mathbb{N}$	The set of natural numbers
$\mathbb{R}$	The set of real numbers
$\mathbb{Z}$	The set of integer numbers
$\mathbb{C}$	The set of complex numbers
$\mathbb{I}_K$	For $K \in \mathbb{Z}$, then $\mathbb{I}_K = \{0, 1, ..., K-1\}$
$\mathbb{1}_{(a,b)}$, $\mathbb{1}_{\mathcal{D}}$	The indicator function on the interval (a, b), and the indicator function on the set $\mathcal{D}$
$\mathcal{D}_{\Omega_{\mathsf{B}}}$	Symmetric baseband interval $[-\Omega_{\mathsf{B}}, ob)$ of width $2\Omega_{\mathsf{B}}$
$f(t)$	Continuous-time functions, $t \in \mathbb{R}$
$\widehat{f}(\omega)$	Continuous-time Fourier transform, $\omega \in \mathbb{R}$
$f[k]$	Discrete-time sequences, $k \in \mathbb{Z}$
$\mathrm{F}(\omega)$	Discrete-time Fourier transform, $k \in \mathbb{Z}$
$\mathrm{Re}(x), \mathrm{Im}(x)$	Real and imaginary part of a complex number x, respectively
$x, \mathbf{x}, \mathbf{X}$	Scalars, vectors (small boldface), and matrices (capital boldface), respectively
$[\mathbf{x}]_i$	The entry of the vector $\mathbf{x}$ at index i
$[\mathbf{X}]_i$, $[\mathbf{X}]_{i,j}$	The entries of the matrix $\mathbf{X}$ at column i and at index (i, j), respectively
$\mathcal{B}_{\Omega}, \mathcal{B}_{\mathsf{MB}}, \mathcal{B}_{\mathsf{BP}}$	The classes of bandlimited, multiband, and bandpass functions, respectively
PW_{Ω}	The space of Paley-Wiener functions
Δ^N	The finite-differences operator of order $N \in \mathbb{N}$
$\mathscr{M}_{\lambda}(\cdot)$	The modulo operator with threshold $\lambda \in \mathbb{R}^+$
$\|\cdot\|_p$	The p-norm for an integer $1 \leq p \leq \infty$. For continuous and discrete functions, it is defined by $\|f\|_p \stackrel{\text{def}}{=} \left(\int_{-\infty}^{\infty} \|f(t)\|^p dt\right)^{\frac{1}{p}}$ and $\|f\|_p \stackrel{\text{def}}{=} \left(\sum_{k\in\mathbb{Z}} \|f[k]\|^p\right)^{\frac{1}{p}}$, respectively
$\mathrm{supp}(f)$	The set of points in the domain of the function f, where f is nonzero Its size is denoted $\#f$
$T_{\mathsf{S}}, T_{\mathsf{NS}}$	Sampling period and the Nyquist period (for bandlimited signals), respectively
$\mathcal{E}(f, g)$	The mean-squared-error (MSE) between signals f and g

To Ronni, Yael, my parents, and my family.
In loving memory of Sibille Shtendel, my beloved grandmother,
who instilled in me self-belief, curiosity, and a lifelong love of learning.

Acknowledgments

My journey was both challenging and deeply rewarding, and, as always, the road turned out to be very different from what I had imagined. Along the way, I was fortunate to have the support of people who believed, guided, and helped me grow as a researcher and as a person.

First and foremost, I would like to thank my supervisor, Dr Ayush Bhandari. I had the unprecedented opportunity to write the first full PhD thesis centred around the Unlimited Sensing Framework, established by Dr Bhandari during his own doctoral work. Ayush is not only a professional and inspiring academic mentor but also a living example of the grit, passion, dedication, and creative boldness required to achieve true research excellence. His vision and encouragement were instrumental throughout this journey.

I would also like to express my gratitude to two postdoctoral researchers with whom I had the privilege to collaborate and co-author papers. From Dr Dorian Florescu, I learned the importance of paying attention to the smallest details and the value of striving for perfection. From Dr Ruiming Guo, I learned a scientific and algorithmic mindset that nothing is truly impossible—it is only that we have not yet found the solution.

Thanks to Peiyu Zhang, Václav Pavlíček, and Yuliang Zhu, whom I first met as undergraduate students. I am grateful for their help, and willingness to assist whenever needed.

I would also like to thank our visiting researchers, Dr Thomas Feuillen and Dr Matthias Beckmann, for their openness, thoughtful discussions, and valuable perspectives. Their insights have greatly helped shape many of the ideas presented in this thesis.

Special thanks to my personal friends and mathematical scholars, Idan Pazi and Jonathan Zin, whose long-standing support and insightful discussions helped shape many of my ideas.

My deepest gratitude goes to my parents and family, who instilled in me the roots of self-belief and the courage to pursue this path. They reminded me of what truly matters and encouraged me to stay grounded and persistent, giving me strength at every step.

Finally, and most importantly, I owe everything to my spouse, Yael, who embarked on this journey with me—and it was quite a journey for her, too. This PhD could not have happened without her unwavering support, patience, and love. I hope this achievement will, in some way, help shape the future of our family, just as her presence has shaped mine.

1

Introduction and Roadmap

1.1 Introduction

The theoretical foundation for the digital representation of analog signals was established by Claude E. Shannon in 1948 [1]. This *sampling theory*, together with transformative hardware innovations such as the transistor [2] and the integrated circuit [3], catalysed the *digital revolution* and the information era by allowing data to be recorded, duplicated, stored, transmitted and distributed without loss of information. More than 80 years later, Shannon's framework continues to underpin the digital infrastructure that shapes every aspect of modern life, from audio recorders to imaging sensors.

At the core of Shannon's theory lies the principle of time quantization: representing a continuous-time signal at discrete-time intervals. Remarkably, for bandlimited signals, this process is lossless when the sampling interval is sufficiently small relative to the signal frequencies. Over time, recovery guarantees from time-quantized samples have been extended to broader signal classes, including finite-rate-of-innovation signals [4], sparse signals [5], and signals with a Fourier structure [6, 7, 8, 9].

Analog-to-Digital Converters. A key strength of Shannon's framework lies in its direct, pointwise mapping from continuous-time signals to discrete samples, a process implemented by the physical device called the Analog-to-Digital Converter (ADC). However, unlike the theory, an ADC cannot represent amplitudes with infinite precision: each sampled value must be mapped onto a finite set of amplitude levels. This process, known as amplitude quantization, is inherently lossy and exposes a gap between Shannon's theoretical framework and its practical implementations [10]:

- Finite **dynamic range**: Input amplitudes that exceed the ADC's limits are clipped,

resulting in nonlinear distortions and permanent information loss.

- Finite **digital resolution**: The measurements are quantized during the analog-to-digital conversion process, introducing *quantization noise* and thereby limiting the precision of the recorded signal. The quantization noise is illustrated in Fig. 1.1(c).

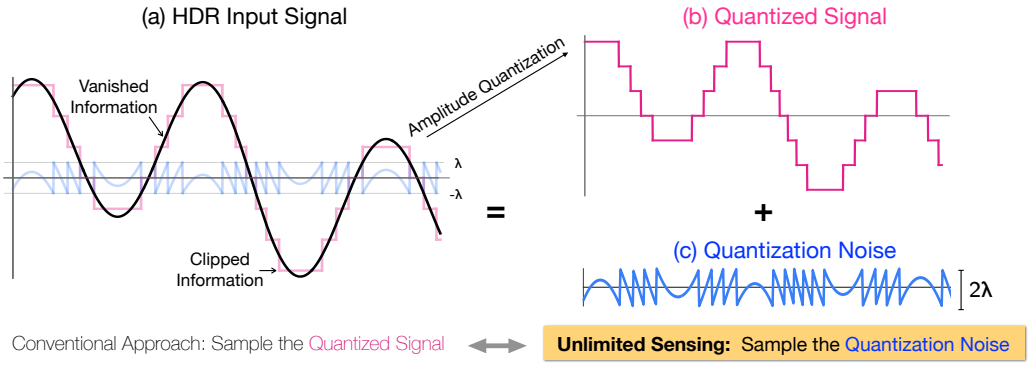


Figure 1.1: Decomposition of high-dynamic-range input signal into quantized signal and quantization noise. (a) A high dynamic range input signal undergoes amplitude quantization, which clips strong components and causes weak components to vanish. (b) The resulting quantized signal captures only the coarse amplitude levels. (c) The residual quantization noise contains the lost fine-scale information. Conventional approaches sample only the quantized signal, whereas the Unlimited Sensing Framework instead samples the quantization noise to recover the lost information.

Given a fixed bit budget, there is a fundamental trade-off between these two properties: expanding the dynamic range to avoid clipping necessarily reduces resolution, whereas increasing resolution reduces the range over which signals can be faithfully captured. This trade-off is illustrated in Fig. 1.2.

Overcoming dynamic range and resolution constraints has been an active research field for several decades. Seminal contributions include declipping and interpolation methods by Papoulis [11], Janssen [12], and Abel [13], as well as studies on quantization noise and dithering by Bennett [14], Schuchman [15], and Gray [16]. However, these foundational methods increasingly fall short in modern applications, where both high dynamic range and fine digital

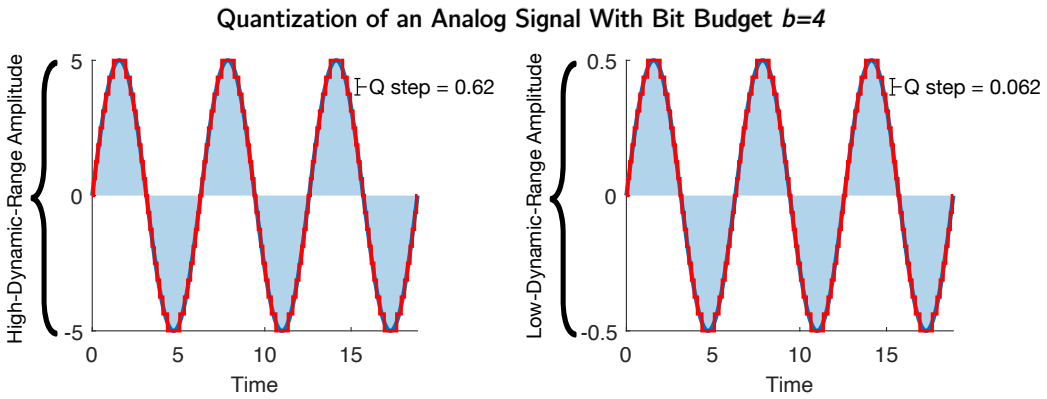


Figure 1.2: The trade-off between dynamic range and digital resolution. Given a fixed bit budget ($b = 4$), there are 2^b amplitude representation levels. The quantization step equals the full dynamic range divided by the number of levels; therefore, higher dynamic range results in a larger quantization step ($Q = 0.62$) compared to the lower dynamic range ($Q = 0.062$).

resolution are essential. Conventional hardware components such as variable gain amplifiers [17] also struggle—for example, when handling strong and weak signals simultaneously [18]. Addressing these challenges calls for a fundamental rethinking of the sampling process, with tighter hardware–software integration, improved handling of nonlinearity, and closer alignment with the characteristics of the data.

The Unlimited Sensing Framework. *The Unlimited Sensing Framework (USF)* [19, 20] is an alternative to Shannon's sampling paradigm, that enables the reconstruction of signals with both high dynamic range (HDR) and high digital resolution (HDRes) using only low-resolution ADCs. The USF achieves this by tightly integrating hardware design with algorithmic reconstruction, following the broader principles of Computational Sensing and Imaging[1].

[1]Computational Sensing and Imaging approaches aim to extract richer information than conventional systems by jointly designing the physical measurement process (encoding) and the computational recovery algorithm (decoding). A well-known example of CoSI is the HDR photography algorithm used in most modern smartphones [21, 22].

Contrary to the conventional wisdom that targets the *quantized signal*, the USF reinterprets the *quantization noise*—the fractional (modulo) part of the signal—as the primary signal to sample and process (see Fig. 1.1). This is based on the key insight that, for sufficiently smooth signals, the fractional part also encodes the missing integer "folds".

The first result to mathematically formalise this idea is the Unlimited Sensing Theorem [19, 20]. This result provides a sampling-rate condition for perfect recovery of bandlimited signals from their modulo samples. In direct analogy to Shannon's sampling theorem, the required rate depends only on signal bandwidth and is independent of the ADC threshold or dynamic range.

Realising USF in practice requires both hardware and algorithmic components. On the hardware side, a modulo nonlinearity is applied before sampling via injection of modulo nonlinearity on the analog signal, so that the modulo samples are captured[23, 24]. On the algorithmic side, one solves the inverse problem of reconstructing the original, "unfolded" signal from these modulo samples.

The first algorithm achieving reconstruction under the conditions of the Unlimited Sensing Theorem was introduced in [20]. Subsequent work incorporated hardware non-idealities and measurement noise, yielding practical reconstruction methods [23, 25, 26]. Hardware validations show up to $60\times$ dynamic-range extension in practice [24], along with 10dB reductions in quantization noise in tomography [27, 28], and radar systems [29]. The USF paradigm has also enabled advances in imaging [30], 1024-QAM transmission [31], and full-duplex communication [32].

Multiband Sampling. In many applications, including communications, radar, and cognitive radio, the signals of interest are *multiband* [33, 34, 35, 36, 37, 38, 39], meaning their

spectral energy is concentrated within several disjoint frequency bands, illustrated in Fig. 1.3. For such signals, directly applying the Shannon–Nyquist theorem leads to prohibitively high sampling rates, often beyond the capabilities of practical devices. This excessive rate can be viewed as the penalty for treating them as bandlimited to their total spectral span, while ignoring the spectral gaps inherent in multiband signals.

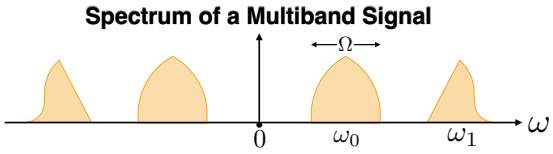


Figure 1.3: The spectrum of a multiband signal.

It is well established that, by exploiting prior knowledge of a signal's Fourier structure, perfect reconstruction can be achieved at sampling rates well below the Nyquist limit [10]. Early work by Kohlenberg [6] proposed dedicated sampling schemes for such signals, while Landau [7] established a fundamental lower bound on the sampling density required for their exact recovery. These seminal contributions laid the theoretical foundations for subsequent advances in the field of *multiband sampling* [40, 41, 42, 43].

Multiband Sampling in Practice. Practical implementations of multiband sampling techniques remain particularly challenging. First, the dynamic range versus resolution trade-off is especially restrictive for multiband signals, which often contain both strong and weak components. In such cases, conventional ADCs may either saturate on the strong components or fail to capture the weaker ones, leading to the well-known near–far problem, illustrated in Fig. 1.4 [44, 45, 18]. Second, operating at sub-Nyquist rates yields only sparse measurements, which heightens susceptibility to noise. Because oversampling, which is a common noise-reduction strategy[46], is inherently unavailable, achieving sufficient signal fidelity typically requires high-resolution ADCs. This, in turn, increases power consumption and hardware

cost, limiting the practical viability of such systems.

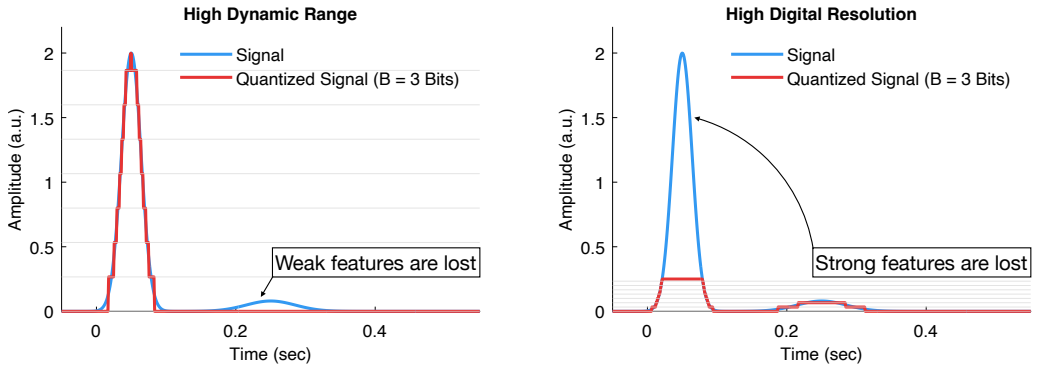


Figure 1.4: Illustration of the near-far problem. Sampling a signal containing both weak and strong components may suffer from analog-to-digital converter limitations. Choosing a quantization range large enough to capture strong components can cause weak features to be lost (left), whereas using a smaller range preserves weak features but saturates strong components (right).

1.2 Research Objectives

The ability of the USF to enhance the effective quantization resolution under a fixed bit budget [24] makes it particularly appealing for sub-Nyquist sampling regimes, where the need for high resolution often constrains practical systems.

However, existing studies of the USF have focused primarily on bandlimited signals. Prior work has examined its injectivity [47], recovery in the time domain [19, 48, 49] and Fourier domain [23], as well as practical implementation aspects [25, 50].

Specifically, we extend the study of the USF to the class of multiband signals, aiming to derive sampling conditions that exploit their Fourier structure to enable sub-Nyquist recovery. Addressing this problem has the potential to yield new theoretical insights, recovery algorithms, and practical architectures that define the main goal of this thesis:

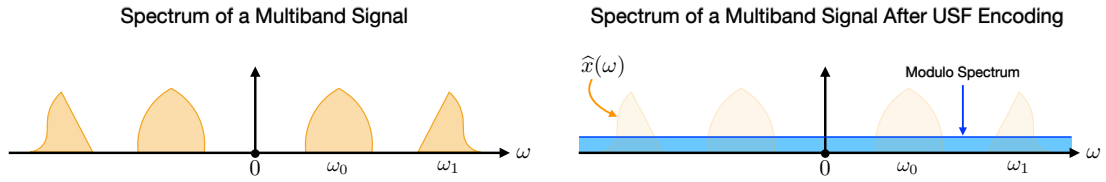


Figure 1.5: The spectrum of a multiband signal before (left) and after (right) encoding based on the Unlimited Sensing Framework (USF).

Develop sub-Nyquist sampling techniques for unlimited sensing of multiband signals

At first glance, this goal may appear contradictory. Sub-Nyquist techniques exploit spectral sparsity and therefore seek to minimise redundancy, whereas the non-linear folding mechanism in the USF produces a spectrum that is neither sparse nor bandlimited, making redundancy crucial for recovery (Fig. 1.5). Reconciling these seemingly conflicting requirements motivates the following research questions:

1. **Theory:** How can the Fourier structure of multiband signals be leveraged to achieve recovery from modulo samples at sub-Nyquist rates?

2. **Algorithms:** What are the corresponding recovery methods?

3. **Validation:** How do the methods translate to practical implementation?

1.3 Thesis Contributions

To address the research questions associated with multiband signals within the USF, the general class of multiband signals is further divided into two subclasses, bandpass signals and single-tone signals, which are studied individually. Their spectral characteristics, along with those of a standard bandlimited signal, are shown in Fig. 1.6.

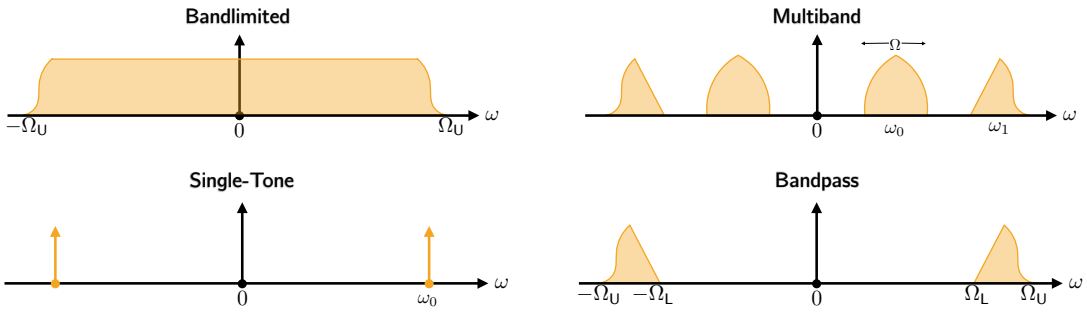


Figure 1.6: Four Fourier-structured signal classes that are relevant for this work. (a) Bandlimited spectrum. (b) Multiband spectrum. (c) Bandpass spectrum. (d) Single-tone spectrum.

This subclass-based approach serves two main purposes. First, it enables the development of tailored strategies for each signal type by accounting for their distinct structure and practical relevance: bandpass signals commonly arise in sonar, radar, ultrasound imaging, and optics, while single-tone signals are central to time-of-flight ranging and 3D imaging. Second, by progressing from simpler to more general cases, the analysis remains tractable while systematically building toward the broader class of multiband signals. An overview of the thesis structure and its main contributions is provided in Fig. 1.7.

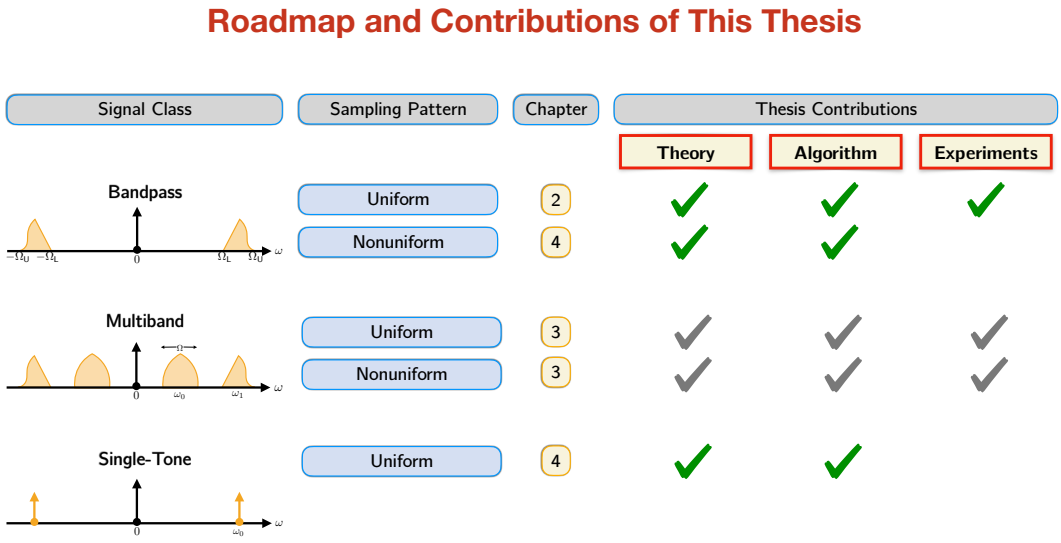


Figure 1.7: Overview of the thesis roadmap and main contributions across signal classes, sampling patterns, and corresponding chapters.

1.4 Thesis Outline and a List of Publications

- **Chapter 2: Background**

  In chapter 2, we introduce the necessary concepts to place this work in context. We begin from the hardware perspective of conversion speed and dynamic range in ADCs. Then, we discuss sub-Nyquist sampling, covering hardware-based demodulation, undersampling, bandpass sampling and periodic nonuniform sampling strategies. Next, the chapter delves into the Unlimited Sampling Framework, highlighting the signal encoding based on the modulo sampling pipeline, and the decoding methods for time- and Fourier- domain based recovery.

- **Chapter 3: Unlimited Sampling of Bandpass Signals**

[∗] G. Shtendel, D. Florescu, and A. Bhandari, "Unlimited sampling of bandpass signals: Computational demodulation via undersampling," *IEEE Trans. Signal Process.*, vol. 71, pp. 4134–4145, Nov. 2023.

In Chapter 3, we introduce the concept of unlimited sampling of bandpass signals and outline the motivation, key contributions, and practical applications. First, the idea of computational demodulation via modulo undersampling is discussed and formalised. Theoretical results are provided under various modulo folding architectures, including ideal, generalized, and non-ideal cases, with recovery guarantees theorems derived for each. Finally, the experimental section validates the theoretical findings through numerical simulations and hardware implementations, demonstrating the robustness and feasibility of the proposed methods.

- **Chapter 4: Unlimited Sampling of Multiband Signals**

[∗] G. Shtendel and A. Bhandari, "Unlimited Sampling of Multiband Signals: Single-Channel Acquisition and Recovery," in *IEEE Signal Processing Letters*, Sep. 2025.

[∗] R. Guo, G. Shtendel, Y. Zhu and A. Bhandari, "Unlimited Sensing for Multiband Signals: From Theory to Practice," in *IEEE Transactions on Signal Processing*, Oct. 2025, [under review].

[∗] R. Guo, G. Shtendel and A. Bhandari, "Multiband Unlimited Sampling: Super-Nyquist or Sub-Nyquist, That is the Question!," *2025 IEEE International Conference on Acoustics, Speech and Signal Processing (ICASSP)*, Hyderabad, India, Apr. 2025, pp. 1-5.

In Chapter 4, we extend the Unlimited Sensing Framework to multiband signals. We derive recovery guarantees that tie the sampling rate to the occupied bandwidth, rather than

the maximum carrier frequency. Building on this, we present a single-channel algorithm operating on frequency-aware differences for sub-Nyquist recovery from modulo samples, and then introduce a multi-channel design with carefully chosen inter-channel delays to resolve aliasing. Finally, we present a quantisation-aware reconstruction pipeline that can accommodate practical non-idealities, which was co-designed with *Dr.* Ruiming Guo. The algorithmic performance was validated in simulation and hardware, with the help of *Mr Yuliang Zhu*.

- **Chapter 5: Unlimited Sensing for Continuous-wave Time-of-Flight and Second Order Bandpass Sampling**

  [∗] G. Shtendel and A. Bhandari, "HDR-ToF: HDR time-of-flight imaging via modulo acquisition," in *Proc. IEEE Int. Conf. Image Process. (ICIP)*, Oct. 2022, pp. 3808–3812.

  [∗] G. Shtendel and A. Bhandari, "Dual-channel unlimited sampling for bandpass signals," in *2024 IEEE International Conference on Acoustics, Speech and Signal Processing (ICASSP)*, Apr. 2024, pp. 9711–9715.

  Chapter 5 contains two independent contributions. In the first part (Section 5.1), the single-tone signal class ($\mathcal{B}_{\mathsf{ST}}$) is considered in the context of high-dynamic-range Time-of-Flight (HDR-ToF) imaging. After formalising the forward model and the inverse problem, a new sampling density criterion is derived, along with a direct reconstruction algorithm that bypasses explicit signal unfolding. Accurate 3D image recovery at a moderate oversampling factor is demonstrated in numerical simulations.

  In the second part (Section 5.2), we extend the single-channel results for the bandpass class ($\mathcal{B}_{\mathsf{BP}}$) in Chapter 3 to second-order bandpass sampling. The design is based on a

dual-channel architecture with two sampling rates. As shown, it allows for accommodating scenarios of spectral overlap, leading to less restrictive sampling rate constraints compared to the bandpass results in Chapter 3. The mathematical guarantee, an efficient recovery algorithm and its numerical validation are presented.

- **Chapter 6: Conclusion**

  In Chapter 6, we conclude the thesis by revisiting its motivation and overarching research problem, summarising the main contributions presented throughout, and discussing the limitations and scope of the proposed approaches. The chapter closes with an outlook on open challenges and promising directions for future research.

2

Background

Shannon's sampling theorem provides the theoretical foundation for converting an analog signal into a sequence of discrete numbers:

Theorem 2.1 [Shannon's Sampling Theorem [51]]

If a function $f(t)$ contains no frequencies higher than Ω (in radians per second), it is completely determined by giving its ordinates at a series of points spaced $T_S = \frac{\pi}{\Omega}$ seconds apart.

Theorem 2.1 requires the knowledge of the discrete samples with 1) infinite precision, 2) infinite dynamic range, and 3) arbitrarily high density, depending on the input bandwidth. In practice, the interface between the analog and digital domains is typically implemented using an Analog-to-Digital Converter (ADC) [52], which cannot yield such ideal samples.

The digitization process as performed by an ADC is illustrated schematically in Fig. 2.1. For an analog input signal $f(t)$, the first stage applies low-pass filtering to ensure bandlimitedness that matches the ADC's bandwidth specifications. In the sampling stage, the signal amplitudes at discrete time instances $t = kT_S$, where $k \in \mathbb{Z}$ and $T_S \in \mathbb{R}^+$, are captured. This is performed by a circuit that maintains a constant output, such as a track-and-hold (T/H) or sample-and-hold (S/H) circuit. The sampled value is then passed to a quantizer, which converts it into a finite digital representation [9].

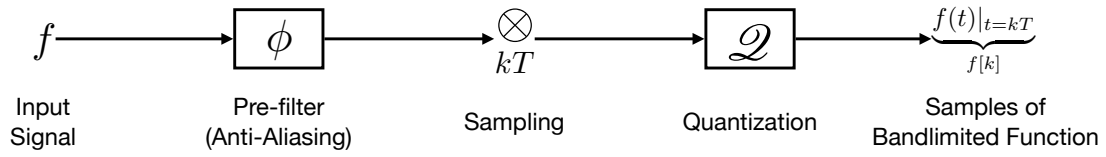


Figure 2.1: The conventional digitization pipeline.

The discrete samples produced by the ADC are influenced by several factors arising from the device's physical limitations. These include aliasing, quantization noise, and clipping, as illustrated in Fig. 2.2(b). A more detailed discussion is provided in Sections 2.1.1 and 2.1.2.

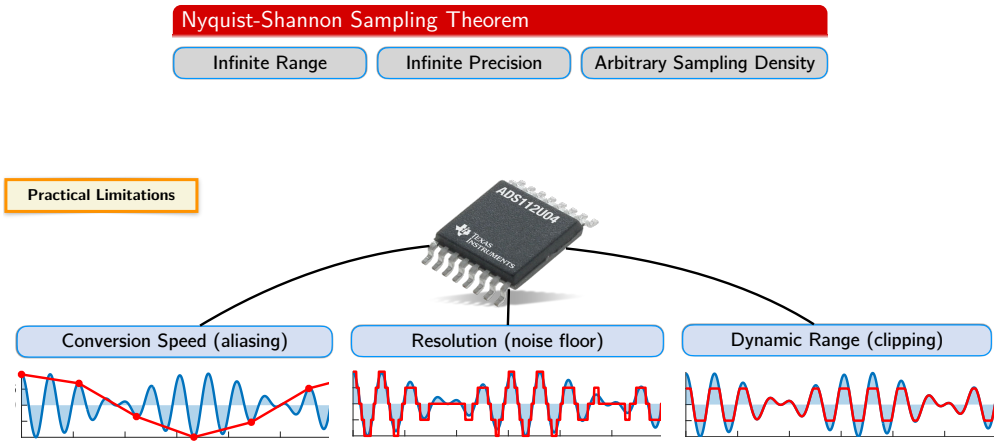


Figure 2.2: Analog-to-digital converters. (a) Ideal assumptions to satisfy Shannon's sampling theorem, (b) practical limitations.

2.1.1 Conversion Rate

The ability of an ADC to reliably digitize the signal amplitudes depends on two rates:

- **Analog Bandwidth:** The rate at which the T/H mechanism can track the analog input. For frequencies exceeding the T/H's analog bandwidth, the signal vanishes within the noise floor, as the frequency response of the T/H decreases with increasing frequency. The analog bandwidth is modelled by a low-pass filter with a cut-off frequency.

- **Sampling Rate:** The rate at which the quantizer operates, denoted by $f_S = 1/T_S$, defines how many samples can be quantized per second. When the sampling rate is

exactly half the bandwidth of the input analog signal, it corresponds to sampling at the Nyquist rate (f_{NS}). Otherwise, the setting is either *undersampling* ($f_{\mathsf{S}} < f_{\mathsf{NS}}$) or *oversampling* ($f_{\mathsf{S}} > f_{\mathsf{NS}}$).

The analog bandwidth is generally larger than the sampling rate [53] and therefore, for sampling at or above the Nyquist rate, where the maximal input frequency satisfies $f_{\mathsf{max}} \leq f_{\mathsf{S}}/2$, it is typically omitted from the model. However, the analog bandwidth does play a role in sub-Nyquist sampling.

The main limiting factor for the sampling rate is the random perturbations in the sampling interval T_{S} [54] between the recorded samples. These are known as the aperture jitter, or *timing jitter* [54]. Timing jitter distorts the obtained values, with a more pronounced effect at higher input frequencies as shown in Fig. 2.3, which consequently leads to a decrease in the signal-to-noise ratio (SNR) of the samples [55].

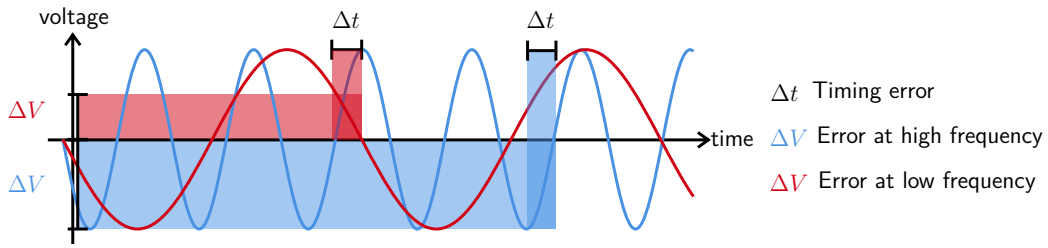


Figure 2.3: The effect of timing jitter at low (red) and high (blue) signal frequencies.

2.1.2 Dynamic Range and Digital Resolution

The *dynamic range* of an ADC refers to the ratio between the largest and the smallest signal intensities the device can resolve[56]. Amplitude values that exceed the ADC's dynamic range are *clipped*, meaning they are mapped to either the minimum or maximum quantiza-

tion values. This effect is illustrated in Fig. 2.4. The clipping effect poses a disruption in various signal acquisition systems, including photography [22], scientific imaging [57], communications [58], and audio [21, 59, 60].

The *digital resolution* of an ADC refers to the smallest detectable input voltage increment, corresponding to the voltage represented by the least significant bit (LSB) [56]. This resolution is given by dividing the ADC's dynamic range by 2^N, where N is the number of digital bits. To improve quantization resolution, system designers sometimes intentionally reduce the input dynamic range by applying a gain or adjusting the reference voltage—effectively using only part of the ADC's physical range to increase sensitivity to smaller signals. Lowering the full-scale voltage reduces the quantization step, enhancing digital resolution.

Limited digital resolution impacts many signal-acquisition systems, including medical imaging [61], remote sensing [62], and audio processing [63].

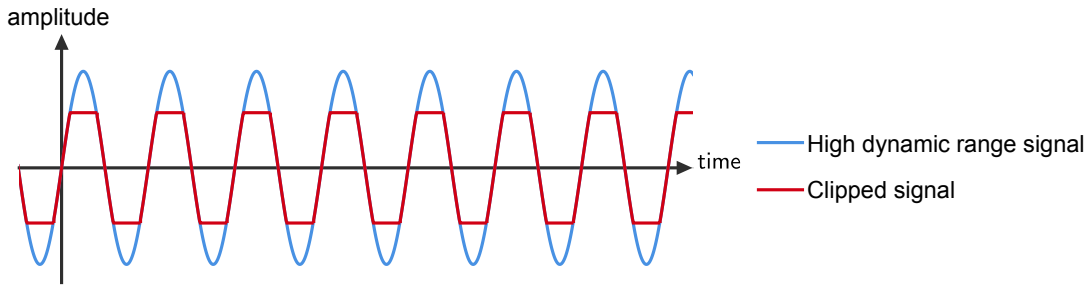


Figure 2.4: High dynamic range (blue) and clipped samples. This effect occurs when the amplitudes exceed the dynamic range of the Analog-to-Digital converter.

2.2 Sub-Nyquist Sampling

Modern applications make use of input signals that span a broad range of the electromagnetic spectrum, from radio frequencies [35, 36] and microwaves, through terahertz radiation, to

visible light [38, 39], as well as ultraviolet, X-rays, and gamma rays. In many cases, sampling at or above the Nyquist rate is impractical—even with state-of-the-art ADCs—or entails prohibitive cost and power consumption. These trade-offs are especially critical in the Internet-of-Things era, where efficiency and scalability are paramount.

The goal of the alternative approach of "sub-Nyquist sampling" is to recover the frequency content of a sampled signal beyond the nominal sampling rate without loss of information. To achieve this, it aims to exploit prior knowledge about the signal, and sample according to its structure, or information rate [64, 9].

A prominent use case for sub-Nyquist methods is acquisition of multiband signals, as illustrated in Fig. 1.5, by exploiting spectral sparsity. The idea is to intentionally translate/alias the occupied subbands into lower-frequency slices that low-rate ADCs can capture, while preserving enough information to reconstruct the original spectrum. Such schemes can rely on analog front-end preprocessing, algorithmic recovery [65, 66], or joint co-design of the sensing and reconstruction stages [67, 53].

2.2.1 The Multiband Signal Model

To discuss the relevant multiband sampling techniques, we first define the class of complex-valued **multiband signals** with *spectral support* $\mathcal{G}$ as[1],

$$\mathcal{B}_{\mathsf{MB}}\left(\mathcal{G}\right) = \left\{x \in L^2 \,:\, \widehat{x}(\omega) = 0,\, \forall \omega \notin \mathcal{G}\right\}, \quad \mathcal{G} \overset{\text{def}}{=} \bigcup\nolimits_{p=0}^{P-1} \left(\omega_p + \mathcal{D}_{\Omega_{\mathsf{B}}}\right), \tag{2.1}$$

[1]Throughout this work, the structure of $\mathcal{G}$ is fixed by context and determined by the parameters $P, \Omega_{\mathsf{B}}, \{\omega_p\}_{p=0}^{P-1}$. Therefore, we omit explicit dependence on $\mathcal{G}$ and write $\mathcal{B}_{\mathsf{MB}}$.

where $\widehat{x}$ denotes the Fourier transform (FT) of x, the set $\mathcal{D}_{\Omega_{\mathsf{B}}} \stackrel{\text{def}}{=} [-\Omega_{\mathsf{B}}, \Omega_{\mathsf{B}})$ is a symmetric baseband interval of width $2\Omega_{\mathsf{B}}$ and $\{\omega_p\}_{p=0}^{P-1}$ are distinct center frequencies (with $\omega_p \neq 0, \forall p$).

By specifying the parameters Ω_{B}, P (assume $\omega_p \neq 0, \forall p$), we derive sub-classes of $\mathcal{B}_{\mathsf{MB}}\,(\mathcal{G})$:

1. **Bandpass signals** ($\mathcal{B}_{\mathsf{BP}}$), defined as (2.1) with $P = 1$.

2. **Single-Tone signals** ($\mathcal{B}_{\mathsf{ST}}$), defined as (2.1) with $P = 1, \Omega_{\mathsf{B}} \to 0$.

Let $\omega_{\mathsf{U}} \stackrel{\text{def}}{=} \max_p \omega_p + \Omega_{\mathsf{B}}$, we denote by $\mathcal{B}_{\omega_{\mathsf{U}}}$ the class of signals bandlimited to ω_{U}. Then, the following inclusion hierarchy holds for any $\mathcal{G}$:

$$\mathcal{B}_{\mathsf{ST}} \subset \mathcal{B}_{\mathsf{BP}} \subset \mathcal{B}_{\mathsf{MB}} \subset \mathcal{B}_{\omega_{\mathsf{U}}}.$$

It is useful to represent signals in $\mathcal{B}_{\mathsf{MB}}(\mathcal{G})$ from (2.1) in the following closed form:

$$x\,(t) = \sum_{p=0}^{P-1} \varphi_p(t) e^{\jmath\omega_p t}, \quad \operatorname{supp}\left(\widehat{\varphi}_p\right) \in \mathcal{D}_{\Omega_{\mathsf{B}}}, \tag{2.2}$$

where each $\varphi_p(t) \in \mathbb{C}$ is a baseband signal modulated to its respective center frequency ω_p.

2.2.2 Hardware-Based Demodulation

A multiband signal written in the form (2.2) is composed as the sum of P baseband signals with maximal frequency Ω_{B}, which are modulated by the set of carrier signals $\{e^{\jmath\omega_p t}\}_{p=0}^{P-1}$ [68]. Sampling such signals below their Nyquist rate of $2\omega_{\mathsf{U}}$ using hardware-based demodulation is described below:

1. The p^{th} passband is de-modulated to be centered around the origin. Mathematically, this is equivalent to multiplying the input signal by the carrier signal's conjugate $e^{-\jmath\omega_p t}$.

2. A low-pass filter is applied to suppress any additional spectral information when extracting the interval $[-\Omega_{\mathsf{B}}, \Omega_{\mathsf{B}}]$. The output signal is the p^{th} baseband φ_p.

3. Sampling at the sub-Nyquist rate $2\Omega_{\mathsf{B}} \leq \Omega_{\mathsf{S}} \leq 2\omega_{\mathsf{U}}$ still yields the above-Nyquist samples of φ_p so no information is lost.

Practical realisation of the process involves frequency mixers [69] and a quadrature demodulation architecture [70], as shown in Fig. 2.5. This is because only $\mathfrak{Re}\left\{\varphi_p\left(t\right) e^{\jmath\omega_p t}\right\}$ can be accessed.

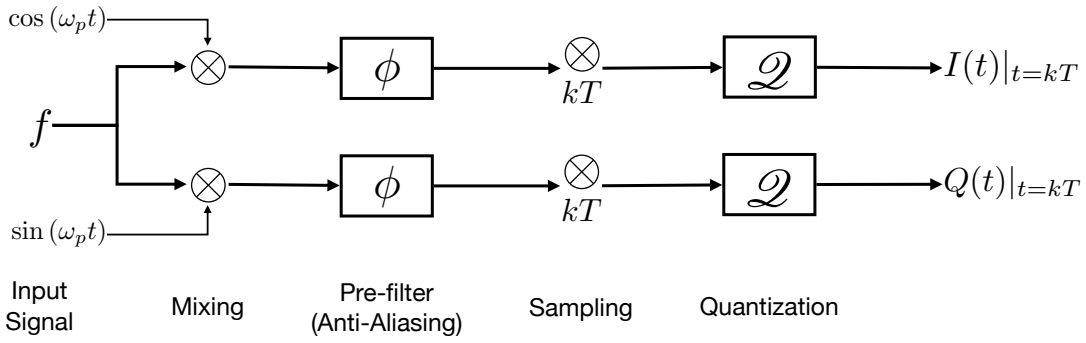


Figure 2.5: I /Q architecture for demodulation of the p^{th} spectral component of a signal, which is centred around frequency ω_p

2.2.3 Undersampling

Sub-Nyquist sampling can also be realised without adding hardware, by operating the uniform sampler in Fig. 2.1 below the Nyquist rate, i.e., with $T_{\mathsf{S}} > T_{\mathsf{NS}}$.

Sampling every T_{S} seconds replicates the continuous-time spectrum at integer multiples of the sampling radian frequency Ω_{S}[2]. This replication is sketched in Fig. 2.7 for a bandpass signal across four periods. Panels (b)–(d) illustrate *undersampling*, where $\Omega_{\mathsf{S}} < 2\omega_{\mathsf{U}} = \Omega_{\mathsf{NS}}$. Notice that in this case, the high-frequency band folds into the baseband interval $(\omega_{\mathsf{L}}, \omega_{\mathsf{L}})$, known as aliasing.

Although aliasing is often undesirable—and the Nyquist condition is derived as a sufficient way to prevent it—it is not always necessary to avoid aliasing. For a given spectrum, there may exist undersampling rates at which the shifted replicas do not overlap, referred to as *alias-free* rates. Formally, a signal x is *alias-free* with respect to the sampling rate T_{S} whenever for $\omega_0 \neq \omega_1$ [71],

$$x \text{ is aliasfree}(T_{\mathsf{S}}) \;\Leftrightarrow\; \omega_0 \bmod \Omega_{\mathsf{S}} \neq \omega_1 \bmod \Omega_{\mathsf{S}} \quad \forall \omega_0, \omega_1 \in \operatorname{supp}(\widehat{x}). \tag{2.3}$$

These rates enable deliberate "spectral compression" for Fourier-sparse signals (e.g., bandpass or multiband): the occupied subbands are translated into nonoverlapping slices of baseband that a low-rate ADC can capture; a subsequent low-pass selection (and, if desired, digital frequency modulation) recovers all relevant information, as illustrated in Fig. 2.7(b)–(d).

Uniform Bandpass Sampling

In the multiband case, the problem of finding alias-free rates is known to be difficult and has no closed-form solution [65, 66]. However, for bandpass signals, alias-free rates can be designed systematically, and this has been studied within the line of work on *bandpass sam-*

[2]Equivalently, the sequence's discrete-time Fourier transform is periodic; the samples act as Fourier-series coefficients over a fundamental band of width Ω_{S}.

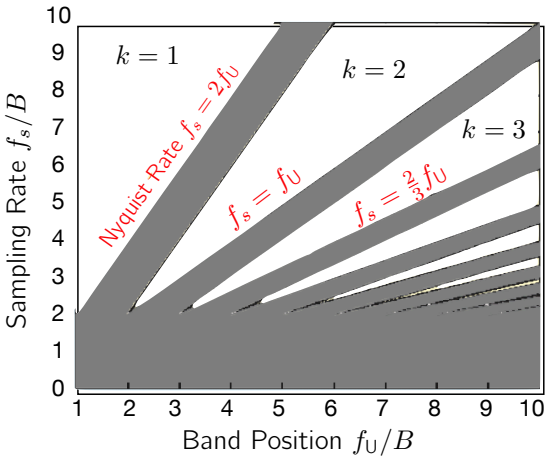


Figure 2.6: The allowed sampling rates based on the bandpass sampling theorem (from [9]).

pling [8, 72, 73]. For real-valued bandpass signals, alias-free sampling rates depend on the band position , and the valid rates are plotted in Fig. 2.6. The next theorem is known as the bandpass sampling theorem [72].

Theorem 2.2 [The Bandpass Sampling Theorem [72]]

Let $x \in \mathcal{B}_{\mathsf{BP}}$ *be a continuous-time bandpass signal where* $x(t) \in \mathbb{R}$. *Let* $\omega_{\mathsf{L}}, \omega_{\mathsf{U}}$ *denote the minimum and maximum frequencies, respectively, of the positive passband. Let* $x[k] = x(t)|_{k=kT_{\mathsf{S}}}$, *where* $T_{\mathsf{S}} \leq \pi/(\omega_{\mathsf{U}} - \omega_{\mathsf{L}})$. *Define* $\widehat{x}_\delta(\omega) = T_{\mathsf{S}} \sum_{k\in\mathbb{Z}} x[k]\, e^{-\jmath\omega kT_{\mathsf{S}}}$. *If there exists* $M \in \mathbb{N}$ *such that,*

$$\frac{\pi(M-1)}{\omega_{\mathsf{L}}} \leq T_{\mathsf{S}} \leq \frac{\pi M}{\omega_{\mathsf{U}}}, \tag{2.4}$$

then $\widehat{x}_\delta(\omega) = \widehat{x}(\omega), \omega \in (-\omega_{\mathsf{U}}, -\omega_{\mathsf{L}}) \cup (\omega_{\mathsf{L}}, \omega_{\mathsf{U}})$ *and* x *can be recovered.*

In Theorem 2.2, M is such that $\left\lfloor \frac{2\omega_{\mathsf{L}}}{\Omega_{\mathsf{S}}} \right\rfloor = M - 1 \in \mathbb{N}$ so there are $M-1$ periods within $(-\omega_{\mathsf{L}}, \omega_{\mathsf{L}})$.

Signal Recovery. Given the samples $x[k]$ of a bandpass signal at a rate that satisfies Theorem

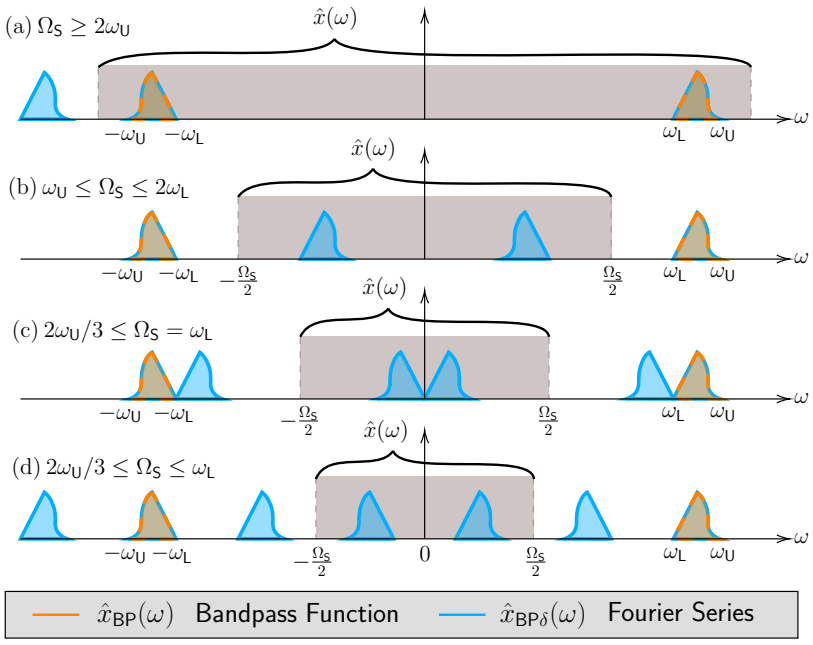


Figure 2.7: The computation of the baseband function $x(t)$. The Fourier transform of the bandpass function (red), and periodicity of the Fourier series of the bandpass samples (blue) at four sampling frequencies. (a) Sampling above the critical rate of the bandpass signal. (b) Sampling frequency within the wedge of $M = 2$. (c) Maximal valid sampling frequency for $M = 3$. (d) Sampling frequency within the wedge of $M = 3$.

2.2, recovery of $x\,(t)$ is obtained by computing the inverse Fourier transform of,

$$\widehat{x}\,(\omega) = \mathbb{1}_{\mathcal{G}(\Omega_S,M)}\,(\omega)\,\widehat{x}_\delta\,(\omega)\,, \quad \mathcal{G}\,(\Omega_S, M) = \tfrac{\Omega_S}{2}\,([-M, (1-M)] \cup [(M-1), M])\,. \tag{2.5}$$

Periodic Nonuniform Sampling

Alias-Free Multiband Sampling and Landau's Bound. Alias-free rates can also exist for multiband signals. However, unlike the bandpass case, there is no general closed-form characterisation. Intuitively, each occupied subband induces a set of admissible sampling rates

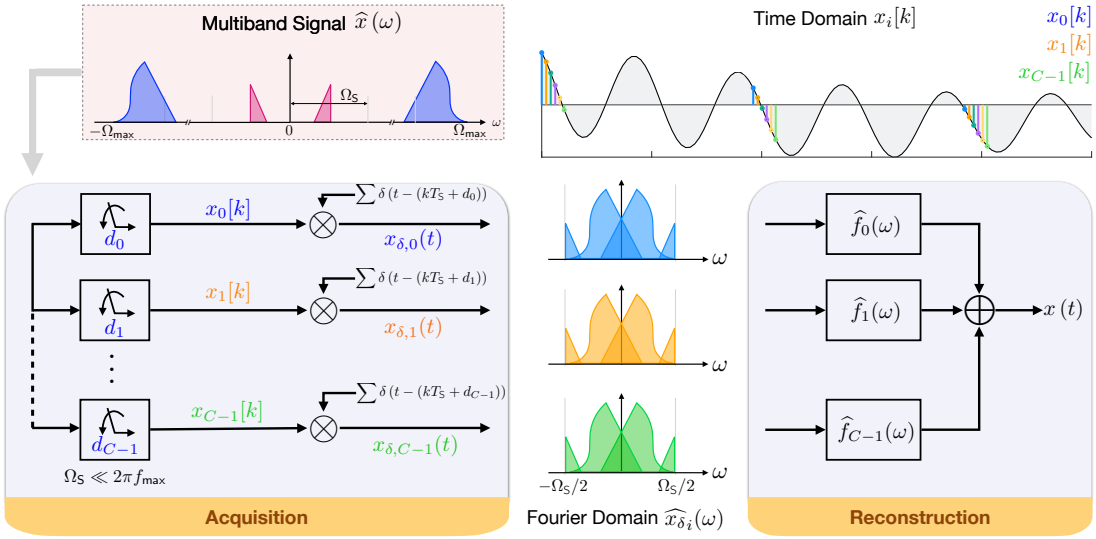


Figure 2.8: Multiband sampling using periodic nonuniform sampling pattern. In the acquisition stage, the input signal is sampled by C channels with respective time-delays d_i. Reconstruction involves filtering the sub-Nyquist sequences, combining them to recover each spectral band, and summing the bands to reconstruct the multiband signal.

(see Fig. 2.6), and an alias-free rate must lie in the intersection of these sets. For a given multiband spectrum, this intersection may be very restrictive or even empty [65].

Shifting subbands along the Fourier axis can be better controlled by using nonuniform sampling patterns. This was formalised by Landau, proving that multiband recovery is possible with samples taken on an arbitrary grid, while the average sampling rate can be reduced to the sum of the occupied bandwidths [74].

Periodic Nonuniform Sampling. Uniform and fully nonuniform sampling are two extremes: the former is easy to implement but is often inefficient, while the latter can approach Landau's limit, but its hardware realisation is challenging. A practical compromise is periodic nonuniform sampling (PNS): the sampling grid comprises C uniformly spaced subsequences

with period $T_{\mathsf{S}} > T_{\mathsf{NS}}$ and relative delays d_i. The samples are

$$x_i[k] = x(t)|_{kT_{\mathsf{S}}+d_i}, \quad 0 \le i \le C-1, \tag{2.6}$$

and the aggregate sampling frequency is $C\Omega_{\mathsf{S}}$, which can be lower than Ω_{NS} and approach Landau's minimal rate. PNS is implementable with C conventional uniform-sampling ADCs (see Fig. 2.8). Unlike uniform sampling, each channel need not operate at an alias-free rate. Controlled spectral overlap across channels is permissible, with recovery enabled by joint processing of the C sequences.

Signal Recovery. For band-pass signals, Kohlenberg [6] derived exact recovery conditions for periodic nonuniform sampling with two sequences ($C = 2$). Coulson [68] generalised these results to higher orders ($C > 2$). Lin and Vaidyanathan [71] further extended the framework to multiband signals. The recovery conditions and a constructive reconstruction procedure described in [71] are summarised below.

The PNS samples given in (2.6) correspond to the continuous-time representation $x_{\delta,i}(t) = x\sum_{k\in\mathbb{Z}}\delta(t-(kT_{\mathsf{S}}+d_i))$. The (normalized) Fourier transform of $x_{\delta,i}(t)$ is

$$\begin{aligned}
\widehat{x}_{\delta i}(\omega) &= T_{\mathsf{S}}\int_{-\infty}^{\infty} x\sum_{k\in\mathbb{Z}}\delta(t-(kT_{\mathsf{S}}+d_i))\,e^{-\jmath\omega t}dt \\
&= T_{\mathsf{S}}\widehat{x}(\omega) * \left(\sum_{l\in\mathbb{Z}}\delta(\omega-l\Omega_{\mathsf{S}})\,e^{-\jmath\omega d_i}\right) = T_{\mathsf{S}}\widehat{x}(\omega) * \sum_{l\in\mathbb{Z}} e^{-\jmath l\Omega_{\mathsf{S}} d_i}\delta(\omega-l\Omega_{\mathsf{S}}) \\
&= T_{\mathsf{S}}\sum_{l\in\mathbb{Z}}\widehat{x}(\omega-l\Omega_{\mathsf{S}})\,e^{-\jmath l\Omega_{\mathsf{S}} d_i}.
\end{aligned} \tag{2.7}$$

The spectrum of each subsequence of the PNS grid, as given in (2.7), is a periodic sum of the multiband spectrum $\widehat{x}(\omega)$. Due to that, $\widehat{x}_{\delta i}(\omega)$ is the sum of $\widehat{x}(\omega-l\Omega_{\mathsf{S}})$ over all integers

$l \in \mathbb{Z}$, for which $\widehat{x}\left(\omega - l\Omega_{\mathsf{S}}\right) \neq 0$. Focusing only on the interval $[-\frac{\Omega_{\mathsf{S}}}{2}, \frac{\Omega_{\mathsf{S}}}{2})$, we can write

$$\widehat{x_{\delta i}}\left(\omega\right) = T_{\mathsf{S}} \sum_{p=0}^{P-1} \widehat{x}\left(\omega - \beta_p\left(\omega\right)\Omega_{\mathsf{S}}\right) e^{-\jmath\beta_p(\omega)\Omega_{\mathsf{S}} d_i},$$

where,

$$\beta_p\left(\omega\right) = \begin{cases} p_0 + 1, & \omega \in [-\frac{\Omega_{\mathsf{S}}}{2}, 0) \\ p_0, & \omega \in [0, \frac{\Omega_{\mathsf{S}}}{2}) \\ 0, & \text{elsewhere} \end{cases}, \quad p_0 = \left\lfloor \frac{\omega_p}{\Omega_{\mathsf{S}}} \right\rfloor.$$

Let,

$$\mathbf{A}\left(\omega\right) = \begin{pmatrix} e^{-\jmath\beta_0(\omega)\Omega_{\mathsf{S}} d_0} & e^{-\jmath\beta_0(\omega)\Omega_{\mathsf{S}} d_1} & \dots & e^{-\jmath\beta_0(\omega)\Omega_{\mathsf{S}} d_{C-1}} \\ \vdots & \vdots & \ddots & \vdots \\ e^{-\jmath\beta_p(\omega)\Omega_{\mathsf{S}} d_0} & e^{-\jmath\beta_p(\omega)\Omega_{\mathsf{S}} d_1} & \dots & e^{-\jmath\beta_{p(\omega)\Omega_{\mathsf{S}} d_{C-1}}} \end{pmatrix},$$

we use a vector-matrix notation to write the sequences $\{\widehat{x_{\delta i}}\left(\omega\right)\}_{i=0}^{C-1}$

$$\begin{pmatrix} \widehat{x_{\delta 0}}\left(\omega\right) \\ \widehat{x_{\delta 1}}\left(\omega\right) \\ \vdots \\ \widehat{x_{\delta C-1}}\left(\omega\right) \end{pmatrix} = \mathbf{A}^{\top}\left(\omega\right) \begin{pmatrix} \widehat{x}\left(\omega - \beta_0\left(\omega\right)\Omega_{\mathsf{S}}\right) \\ \vdots \\ \widehat{x}\left(\omega - \beta_{p-1}\left(\omega\right)\Omega_{\mathsf{S}}\right) \end{pmatrix}, \tag{2.8}$$

Given $\{\widehat{x_{\delta i}}\left(\omega\right)\}_{i=0}^{C-1}$, the recovery is performed in the Fourier domain using a filter bank

$\{f_i\}_{i=0}^{C-1}$ for each passband. For the i^{th} passband, it is computed by solving

$$\mathbf{A}\begin{pmatrix} \widehat{f}_0(\omega) \\ \vdots \\ \widehat{f}_{C-1}(\omega) \end{pmatrix} = \begin{pmatrix} 0 & \cdots & 0 & \underbrace{1}_{i^{\text{th}}\text{ index}} & 0 & \cdots & 0 \end{pmatrix}^{\top} \tag{2.9}$$

for every $\omega \in \left[-\frac{\Omega_{\mathsf{S}}}{2}, \frac{\Omega_{\mathsf{S}}}{2}\right]$ on which the replica of the passband is nonzero. Then, applying the filter bank $\left\{\widehat{f}_i(\omega)\right\}_{i=0}^{C-1}$ on both sides of (2.8) extracts the passband. To recover the multiband signal, the procedure has to be performed for all the passbands. This requires $\mathbf{A}$ in (2.9) to be nonsingular for $\omega \in \operatorname{supp}(\widehat{x}(\omega))$. As shown in [71], a convenient choice for the delays is $d_i = id_0$ because it renders $\mathbf{A}(\omega)$ a Vandermonde matrix, and the conditions for nonsingularity become:

$$\text{a) } C = L, \quad \text{b) } e^{\jmath\beta_p(\omega)\Omega_{\mathsf{S}}d_i} \neq 1, \quad \text{and c) } e^{\jmath\beta_p(\omega)\Omega_{\mathsf{S}}d_i} \neq e^{\jmath\beta_m(\omega)\Omega_{\mathsf{S}}d_i} \text{ for } i \neq m.$$

Based on that, finding delay d_0 for which $\mathbf{A}^{-1}(\omega)$ exists is a tractable problem.

The formulation in (2.8) suggests that a PNS grid composed of C sequences can resolve up to C spectral passbands that overlap at the same frequency. These ideas can be related to those considered by Papoulis in the *generalised sampling* [75] theory to overcome aliasing.

2.3 The Unlimited Sensing Framework

Computational Sensing and Imaging. Existing technology is shaped by two opposing trends: on one hand, modern smartphones are more powerful than the computers used dur-

ing NASA's Apollo missions[3]; on the other hand, hardware capabilities are already being pushed to their limits[4]. These trends motivate a signal processing approach that harnesses modern fabrication techniques together with strong computational capabilities, called *computational sensing and imaging* (CoSI) [76]. Underpinning CoSI is a paradigm shift from the conventional "capture first – process later" approach, towards a co-design of hardware and complementary algorithms. A renowned example of CoSI is the commercialised high dynamic range (HDR) photography algorithm [21] that is prevalent in most modern smartphones [22]. In crux, CoSI frameworks are composed of:

- **Encoding.** The hardware is designed to produce the indirect measurements of a desired quantity. Ultimately, by encoding the measurements, more information can be captured than would be possible directly using the same resources.
- **Decoding.** The information is recovered from the encoded measurements using algorithms and computational routines.

Mathematically, the encoding stage corresponds to a *forward model*, while the decoding stage involves solving the associated *inverse problem*.

The Unlimited Sensing Framework (USF). The USF is a computational sensing protocol that employs a unique encoding–decoding process to acquire signals with arbitrary dynamic range at high resolution. Since its introduction in [19], the framework has been significantly extended in terms of theory, hardware implementation, and applications. This section provides a brief overview of its main aspects, which are most relevant to the scope of this work.

[3] https://www.popularmechanics.com/space/moon-mars/a25655/nasa-computer-iphone-comparison/
[4] https://spectrum.ieee.org/power-problems-might-drive-chip-specialization

2.3.1 Encoding — The Modulo Sampling Pipeline



Figure 2.9: The modulo acquisition pipeline.

The USF is based on the non-linear digitization pipeline shown in Fig. 2.9. The non-linear mapping is performed by the centred modulo operator with threshold λ

$$\mathscr{M}_\lambda : x \mapsto 2\lambda \left(\left[\!\!\left[\frac{x}{2\lambda} + \frac{1}{2} \right]\!\!\right] - \frac{1}{2} \right), \quad [\![x]\!] \stackrel{\text{def}}{=} x - \lfloor x \rfloor, \tag{2.10}$$

where $[\![x]\!]$ and $\lfloor x \rfloor$ define the fractional part and floor function, respectively. Compared to the conventional signal acquisition model from Fig. 2.1, the USF pipeline incorporates an encoding process realised by the modulo mapping, which compresses the amplitude information into a fixed dynamic range. Given a signal $f \in L^2$, the full pipeline is described as follows:

1. Pre-filtering with a non-aliasing filter $\phi(t)$. The low-pass approximation of $f(t)$ is

$$x(t) = f(t) * \phi(t) = \int f(\tau)\, \phi(t-\tau)\, d\tau. \tag{2.11}$$

2. Non-linear mapping with the operator $\mathscr{M}_\lambda(\cdot)$. The output is $y(t) \stackrel{\text{def}}{=} \mathscr{M}_\lambda(x(t))$.

3. Uniform sampling using an impulse train $\otimes_{kT_\mathsf{S}} \stackrel{\text{def}}{=} \sum_{k=\in\mathbb{Z}} \delta(t - kT_\mathsf{S})$ with parameter

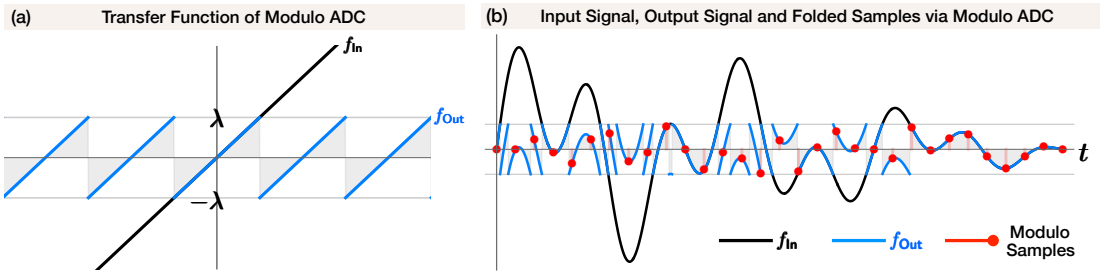


Figure 2.10: The modulo ADC ($\mathscr{M}$–ADC). (a) Transfer function. (b) Input signal, output signal and modulo point-wise samples [48].

$T_s > 0$. This results in

$$y\left[k\right] \overset{\text{def}}{=} y\left(t\right)|_{t=kT_{\text{S}}}, \quad k \in \mathbb{Z}.$$

4. B-bits quantization of $y\left[k\right]$. The values of $y\left[k\right]$ are rounded to the closest set element in

$$\mathcal{C}_{B,\lambda} = \left\{ \pm \frac{(2n+1)}{2^B}\lambda \quad \middle| \quad n \in \left\{0, \ldots, 2^B - 1\right\} \right\}, \tag{2.12}$$

where $[-\lambda, \lambda)$ are the dynamic range extremums.

Notice that the mapping (2.10) is injected before the uniform sampling stage, so the low-pass signal to be sampled x is encoded into a bounded signal $y\left(t\right) = \mathscr{M}_\lambda(x\left(t\right)) \in [-\lambda, \lambda)$, and clipping cannot occur. This effect is visualised for some common input signals in Fig. 2.11.

The first hardware demonstration of the above encoding procedure was demonstrated in [23] using the $\mathscr{M}$–ADC, whose transfer function is shown in Fig. 2.10. In all the following analyses, we discuss the forward model

$$y\left[k\right] = \mathscr{M}_\lambda(x\left(kT_{\text{S}}\right)), \quad k \in \mathbb{Z}, \tag{2.13}$$

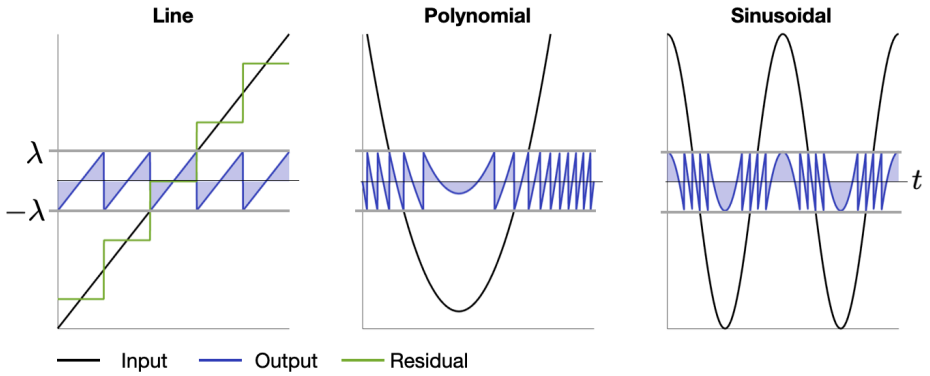


Figure 2.11: The modulo waveform (blue) generated by the $\mathscr{M}$–ADC for different types of input signals (black). The residual between the input and the modulo waveforms is shown in green. Notice that this is in fact the quantized signal that is sampled in a conventional analog-to-digital pipeline.

and the non-linear inverse problem

$$\text{given } y\left[k\right], \text{ find } x\left(t\right) \quad \text{s. t.} \quad y = \mathscr{M}_{\lambda}(x\left(kT_{\mathsf{S}}\right)). \tag{2.14}$$

Sampling Resolution

The conventional trade-off between dynamic range and noise floor, discussed in Section 2.1.2, states that for a fixed bit budget, increasing the dynamic range necessarily increases the quantization step size, and vice versa. This trade-off is reflected by the signal-to-quantization noise ratio, defined as $\mathrm{SQNR} \stackrel{\mathrm{def}}{=} 10\log_{10}\left(\frac{\sigma_q^2}{\sigma_x^2}\right)$, where σ_x^2 and σ_q^2 denote the power of the signal (assuming zero mean) and the quantization noise, respectively. Remarkably, the USF challenges this limitation. Modulo signals not only encode large input amplitudes effectively, but they also enable smaller quantization steps, thereby achieving both a higher dynamic range and improved resolution simultaneously. Quantitatively, the quantization error of the $\mathscr{M}$–ADC is reduced by a factor of $\zeta = \frac{\lambda}{||x||_{\infty}}$. compared to the case of a conventional ADC.

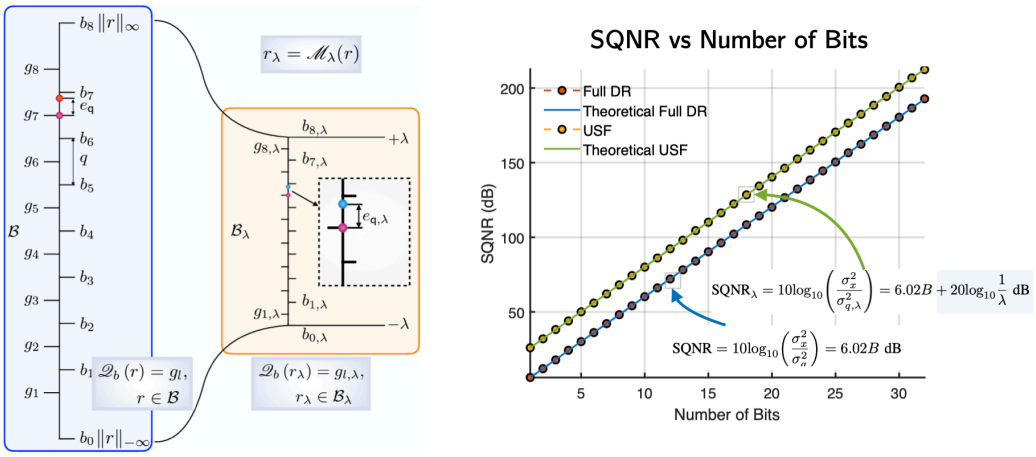


Figure 2.12: Left: Illustration of the quantization process for bit resolution b = 3 (from [31]). Right: Comparison between the signal-to-quantization noise ratio (SQNR) of a conventional ADC and the modulo ADCs.

Identifiability in Unlimited Sampling

The forward model in (3) results in a non-linear, many-to-one mapping (2.10) that makes the inverse problem (2.14) inherently ill-posed. However, as proved both in [47] and [77], the problem is well-posed for any sampling rate $0 < T_S < \pi/\Omega$, such that the modulo samples $y[k]$ uniquely characterise the bandlimited function x. Normalizing the bandwidth of $x(t)$ to $\Omega = \pi$ so the critical sampling rate is $T_{NS} = 1$, an oversampling rate is denoted by $T_\epsilon = \frac{\pi}{\pi+\epsilon}, \epsilon > 0$, where $0 < T_\epsilon < 1$. Then, this injectivity property is formalised as follows.

Theorem 2.3 [Injectivity for Modulo Sampling [47]]

Any $f \in \mathsf{PW}_\pi$ *is uniquely determined by its modulo samples that are recorded on the grid* $\{t_n = nT_\epsilon\}_{n\in\mathbb{Z}}$ *with* $\epsilon > 0$.

2.3.2 Decoding — Algorithmic Signal Recovery

The $\mathscr{M}$–ADC's encoding operation must be followed by a decoding procedure for solving the inverse problem in (2.14). Depending on the signal class of interest, algorithms have been proposed for different acquisition models and processing techniques [48, 23, 78, 79, 30]. The main focus in this study is the class of bandlimited signals. In the following, we first set up the different models for the acquired modulo signal that are used in various works. Then, a survey of the key recovery methods is given.

Folding Architectures

The USF-based signal recovery is based on exploiting the structure of the sampled modulo signal. In particular, the modulo decomposition property.

Theorem 2.4 [Modulo Decomposition Property [48]]

The bandlimited function $x \in \mathcal{B}_\Omega$ admits a decomposition,

$$x(t) = y(t) + r(t), \tag{2.15}$$

where $y(t) = \mathscr{M}_\lambda(x(t))$, $\lambda > 0$ and $r(t)$ is a step-wise function.

We will refer to $r(t)$ also as a simple function, or a residual function. This function holds the discontinuities that are introduced by the modulo folding step. Theorem 2.4 is visualised in Fig. 2.13.

Having the samples $y[k]$, knowing $r[k] = r(t)|_{t=kT_\mathrm{S}}$ is equivalent to knowing $x[k]$ since they can be computed one from the other using (2.15). Therefore, the inverse problem (2.14)

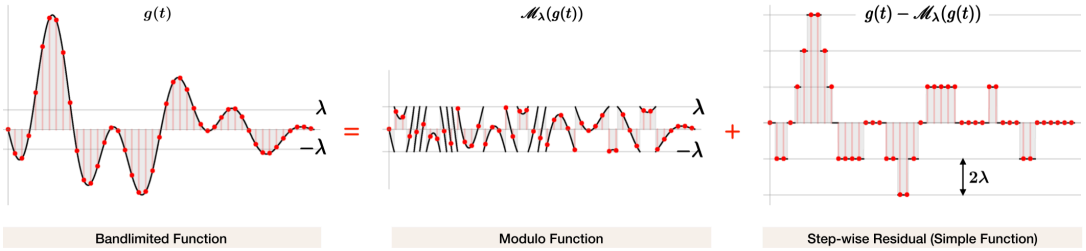


Figure 2.13: The modulo decomposition property.

boils down to finding $r\,[k]$. The advantage of recovering the residual part is that its structure can be leveraged for the task. In the USF line-of-work, 3 main models for $r\,(t)$ that are used:

1. *Ideal Modulo Folding ($\mathscr{M}_\lambda$).* Assuming that all the folds have an exact amplitude equal to 2λ, the residual function model was given by,

$$r\,(t) = 2\lambda \sum_{m\in\mathbb{Z}} e[m]\mathbb{1}_{\mathcal{D}_m}\,(t),\;\; e[m] \in \mathbb{Z}, \tag{2.16}$$

   where the real line is partitioned into intervals $\mathcal{D}_m$ such that $\bigcup_{m\in\mathbb{Z}} \mathcal{D}_m = \mathbb{R}$. Recovery algorithms based on this model were proposed for different input signal classes and sampling architectures [48, 80, 81, 79, 82, 27].

2. *Non-Ideal Modulo Folding ($\widetilde{\mathscr{M}_\lambda}$).* The advent of the $\mathscr{M}$–ADC enabled the investigation of practical realisations of the modulo-based encoding [23, 83, 50]. It was observed that the amplitudes of the residual part do not necessarily belong to the set $2\lambda\mathbb{Z}$. A model that incorporates this empirical observation was proposed in [23],

$$r\,(t) = \sum_{m\in\mathcal{M}} c_m \mathbb{1}_{\mathcal{D}_m}\,(t),\;\; \cup_m \mathbb{1}_{\mathcal{D}_m} = \mathbb{R},\;\; c_m \in \mathbb{R}, \tag{2.17}$$

where $\mathcal{M}$ is the number of folding instances. The model can describe the effect of disruptions in the sampled signal, like reset- or shot- noise [50], as well as imperfections in the acquisition device [83] and deviations in the modulo threshold.

3. *Generalized Folding* ($\mathscr{M}_{\mathsf{H}}$). To compensate for further model deviations that were revealed in hardware experiments with the $\mathscr{M}$–ADC [84, 25, 83, 85], a generalised residual model was proposed in [25]. This model adds two degrees of freedom to the residual function, incorporating two effects: *hysteresis*, where increasing or decreasing signals exhibit a different threshold, and the folding *transient* effect, where the folding does not happen instantaneously, but rather it has a non-negligible time duration. The generalized residual model with parameters $\lambda, h \in [0, 2\lambda), \alpha \in \mathbb{R}^+$ is [25],

$$r(t) = \sum\nolimits_{p\in\mathbb{Z}} s_p \varepsilon_0 (t - \tau_p), \text{ where } \quad \varepsilon_0(t) = 2\lambda_h \left[\tfrac{1}{\alpha} t \cdot \mathbb{1}_{[0,\alpha)}(t) + \mathbb{1}_{[\alpha,\infty)}(t)\right], \tag{2.18}$$

and $\lambda_h = \lambda - \frac{h}{2}$, $s_p = \operatorname{sign}(x(\tau_p) - x(\tau_{p-1}))$. Moreover, $p \geq 1$, $\{\tau_p\}$ is an asynchronous sequence satisfying $\tau_0 = 0$ and,

$$\begin{aligned}
\tau_1 &= \min\{t > \tau_0 | \mathscr{M}_\lambda(x(t) + \lambda) = 0\} \\
\tau_{p+1} &= \min\{t > \tau_p | \mathscr{M}_\lambda(x(t) - x(\tau_p) + h s_p) = 0\}.
\end{aligned}$$

The value of h controls the minimal time between folding adjacent instances τ_p and τ_{p+1}, where for $h = 0$ folds can be arbitrarily close, like in the ideal model.

Illustration of a bandlimited signal and the folded outputs of the three architectures is shown in Fig. 2.14

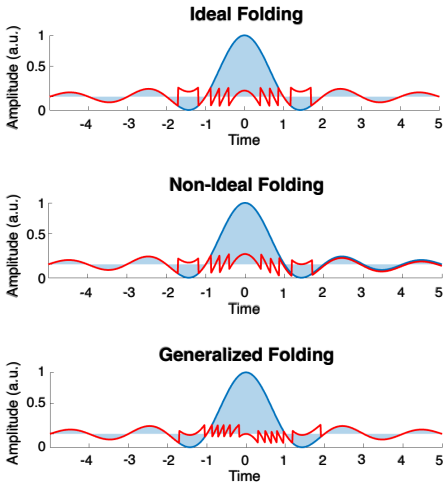


Figure 2.14: Illustration of modulo folding by different folding architectures. Upper: Ideal folding. Middle: Non-ideal folding, where the discontinuities are not confined to the grid $2\lambda\mathbb{Z}$. Lower: Hysteresis effect, where discontinuities do not reset to the threshold value.

Time-Domain Based Recovery

The injectivity theorem 2.3 indicates that, under certain conditions, the recovery of a bandlimited signal from its modulo samples becomes a well-posed problem. To extract this unique solution, the following algorithms utilise prior knowledge on the structure of the residual signal (2.16), and recover $x\left(t\right)$ using time-domain processing.

The Unlimited Sampling Theorem and Algorithm. A sufficient condition for guaranteed recovery of a bandlimited signal x from its modulo samples is in the next theorem [48].

Theorem 2.5 [The Unlimited Sampling Theorem [19, 48]]

Let x be a continuous-time function with maximum frequency Ω $\frac{\text{rad}}{\text{sec}}$. Then, a sufficient condition for the recovery of $x\left(t\right)$ from its modulo samples (up to an additive constant) taken every T_{S} seconds apart is $T_{\mathsf{S}} \leqslant 1/\left(2\Omega e\right)$ where e is Euler's number.

The sampling density criterion in Theorem 2.5 exploits the property that bandlimited samples $x[k] \stackrel{\text{def}}{=} x\left(kT_{\mathsf{S}}\right)$ can be upper bounded in the higher-order differences domain. Mathematically, $\|\Delta^N x\|_\infty \leq \left(T_{\mathsf{S}}\Omega e\right)^N \|x\|_\infty$, where $\Delta^N x$ denotes N-th order difference operator on x. Based on the previous relation, if

$$T_{\mathsf{S}} \leq T_{\mathsf{US}} = \tfrac{1}{2\Omega e}, \tag{2.19}$$

then for

$$N^\star \geq \left\lceil \frac{\log \lambda - \log \beta_x}{\log\left(T_{\mathsf{S}}\Omega e\right)} \right\rceil, \quad \beta_x \in 2\lambda\mathbb{Z}, \quad \text{and} \quad \beta_x \geq ||x||_\infty, \tag{2.20}$$

it is guaranteed that $||\Delta^{N^\star} x||_\infty < \lambda$ [48]. From modular arithmetic, we have the property that $\mathscr{M}_\lambda(\Delta^N \mathscr{M}_\lambda(x\,[k])) = \mathscr{M}_\lambda(\Delta^N x\,[k])$. Then, under the assumption of ideal modulo sampling, that is the residual function follows (2.16), this property can be leveraged to separate $x\,[k]$ and $r\,[k]$ in the higher differences space,

$$\mathscr{M}_\lambda(\left(\Delta^N y\right)[k]) = \mathscr{M}_\lambda(\left(\Delta^N x\right)[k]) = \left(\Delta^N x\right)[k]\,. \tag{2.21}$$

Given $\left(\Delta^N x\right)[k]$, by inversion of the finite differences operation, the inverse problem (2.14) can be solved. Let S define the anti-differences operator

$$\mathsf{S} : \{s[k]\}_{k\in\mathbb{Z}^+} \rightarrow \sum_{m=1}^{k} s[m], \tag{2.22}$$

that inverts the operator Δ up to an unknown constant. The recovery is based on applying

Algorithm 1: The Unlimited Sensing Algorithm (US-Alg)

Data: $y[k] = \mathscr{M}_\lambda(x(kT_\mathsf{S}))$.
Result: $\widetilde{x}(t) \approx x(t)$.

1) Compute N from (2.20).
2) Compute $(\Delta^N y)[k]$.
3) Compute $s_{(0)}[k] = \left(\mathscr{M}_\lambda(\Delta^N y) - \Delta^N y\right)[k]$.
4) Define $\mathsf{S} : \{s[k]\}_{k\in\mathbb{Z}^+} \to \sum_{m=1}^{k} s[m]$.
   For $n = 0 : N-2$:
   $4(a)$ $s_{(n+1)}[k] = \left(\mathsf{S}\left(s_{(n)}\right)\right)[k]$.
   $4(b)$ $s_{(n+1)} = 2\lambda \left\lceil \frac{\lfloor s_{(n+1)}/\lambda \rfloor}{2} \right\rceil$.
   $4(c)$ $\kappa_n = \left\lfloor \frac{\mathsf{S}\left(s_{(n+1)}\right)[1] - \mathsf{S}\left(s_{(n+1)}\right)[J+1]}{12\beta_X} + \frac{1}{2} \right\rfloor$.
   $4(d)$ $s_{(n+1)}[k] = s_{(n+1)}[k] + 2\lambda\kappa_{(n)}$.
   end
5) $\widetilde{x}[k] = \left(\mathsf{S}\left(s_{(N-1)}\right)\right)[k] + y[k]$.
6) $\widetilde{x}(t) = \sum_{k\in\mathbb{Z}} \widetilde{x}[k] \operatorname{sinc}\left(\frac{t}{T_\mathsf{S}} - k\right)$.

S sequentially N times on the finite differences of the residual. The restriction on its amplitudes is used to find the unknown constant. The full recovery algorithm, called US-Alg [48], is summarised in Algorithm 1. The recovery using US-Alg is not restricted by the number of folds in the signal, leading to theoretically infinite dynamic range. It is also suitable for measurements with additive bounded noise, where $y_\eta[k] = y[k] + \eta[k]$, $|\eta[k]| \leq \beta_0$, for some $\beta_0 > 0$ and $\forall k \in \mathbb{Z}$. Romanov et al. [77] proposed a recovery algorithm for any $T_\mathsf{S} > T_\mathsf{NQ}$, given that there is $T_0 \in \mathbb{R}$ for which $\|x(t)\| < |t|^{-\rho}$, $\rho > 0$ for $|t| > T_0$. The recovery is based on a prediction filter.

Results Demonstrating Applicative Utility. In US-Alg, the bandlimited and the residual samples that compose y based on (2.15) are separated in the higher-order difference space. This same principle was later adapted to a series of algorithms that enable efficient HDR signal acquisition for different sensing and imaging systems. In [86], such a framework for computational array processing was presented. The advantage of the proposed algorithms is

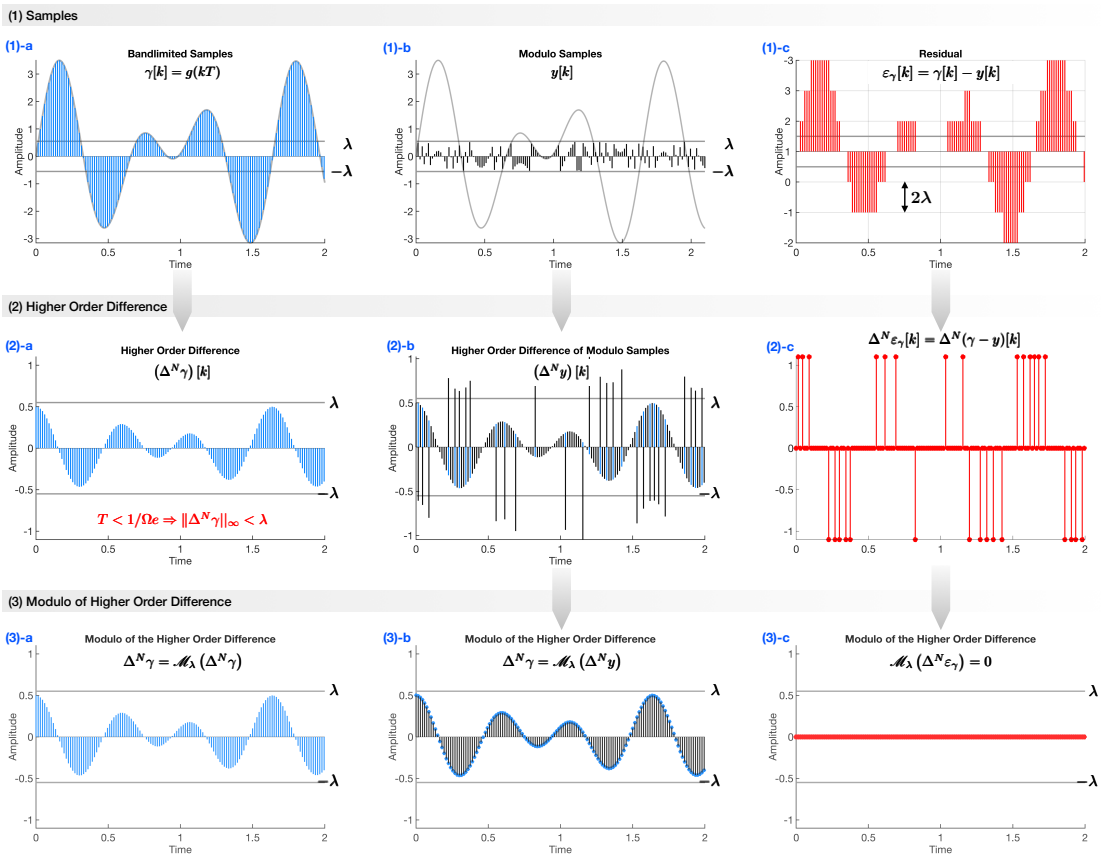


Figure 2.15: Time-domain partitioning of modulo samples into their bandlimited and residual components $x[k]$ and $r[k]$ respectively, based on higher order finite differences operator (from [48]).

the capability to estimate the direction of arrival directly from the eigenvalues of the higher-order differences samples and to retrieve a beamformed signal directly from the folded samples. Beckmann et al. defined the Modulo Radon transform (MRT) in [27] as a composition of the Radon and Modulo operators. The authors prove the injectivity of the MRT, and demonstrate its utilisation for computerised tomography systems via a recovery algorithm named US-FBP. A proof of concept for FMCW radars was presented in [87]. An HDR Time-of-Flight imaging framework is part of this thesis, and covered in Section 5.1).

Sampling Architectures for Bandlimited Signals. The ideal modulo non-linear mapping was integrated into common sampling architectures such as 1-bit $\Sigma\delta$ and multi-channel sampling. Graff et al. [80] observed that the fact that both the modulo and 1-bit $\Sigma\delta$ sampling architectures trade the bit budget with oversampling makes their integration desirable. The authors formulated recovery guarantees and algorithms that are not based on finite difference operations, as these are not beneficial in the 1-bit $\Sigma\delta$ case. Multi-channel sampling architecture was examined by Lu et al. in [82]. In the proposed framework, the bandlimited signal is sampled simultaneously with multiple channels at the critical rate. The threshold on each channel varies such that the values are coprime numbers. Then, the Chinese Remainder Theorem enables the unfolding of the modulo samples.

Time-Domain Based Recovery for Modulo Hysteresis Folding. The generalized model of the residual function (2.18) allows tackling some non-standard sampling scenarios such as incomplete folds [25], non-pointwise average sampling [83], or event-driven sampling [84, 85]. As in the ideal folding case, the recovery is again based on estimation of the residual samples $r\left[k\right]$, which is equivalent to finding the folding instances and amplitudes, (s_p, τ_p), in the case of the parametric model (2.18). Here, the recovery is based on first filtering the data by a generic filter ψ_N that produces, $\psi_N * y\left[k\right] = \psi_N * x\left[k\right] - \psi_N * r\left[k\right]$. Then, for cases when the transient duration α is negligible, a variation of the US-Alg based on λ_h can be used. Otherwise, a *thresholding* based algorithm was presented in [25].

Fourier-Domain Based Recovery

A Fourier-domain approach for solving the problem (2.14) was suggested in [23]. The method leverages the fact that for $x \in \mathcal{B}_\Omega$, then $\widehat{x}\left(\omega\right) = 0, \forall|\omega| > \Omega$ while $\mathscr{M}_\lambda(x\left(t\right)) \notin \mathcal{B}_\Omega$. To

formulate this, the input signal is assumed to be τ-periodic such that $x(t) = x(t+\tau)$. Sampling with period T_S yields $K = \tau/T_\mathsf{S}$ samples over one period. Denote by $\widehat{x}$, $\widehat{y}$, $\widehat{r}$ the DFT of the K-length sequences x, y, and r, respectively. The Fourier-domain partition of the finite difference sequence Δy satisfies

$$\widehat{\Delta y}[n] = \begin{cases} \widehat{\Delta x}[n] - \widehat{\Delta r}[n] & n \in (\mathbb{E}_{P,K-1}) \qquad \text{(in-band interval)}, \\ -\widehat{\Delta r}[n] & n \in (\mathbb{I}_{K-1} \setminus \mathbb{E}_{P,K-1}) + (K-1)\,\mathbb{Z} \quad \text{(out-of-band interval)}, \end{cases} \tag{2.23}$$

where $P = \lceil \frac{\Omega\tau}{2\pi} \rceil$ and we assume $K \geq 2P+1$, which is an oversampling setting. The Fourier-domain separation (2.23) is not based on the higher-order differences like the time-domain separation (Section 2.3.2). Also, there is no need for the assumption of $r(t) \in 2\lambda\mathbb{Z}$. This allows using the non-ideal model for the residual function (2.17). Mathematically, the finite differences sequence of the residual samples has a DFT that can be written as,

$$\widehat{\bar{r}}[n] = \sum_{m=0}^{M-1} w[m]\, e^{-\jmath \frac{2\pi}{K-1}\kappa[m]n}, \quad \bar{r} \stackrel{\text{def}}{=} \Delta r, \tag{2.24}$$

which is a function of $2M$ parameters, where M is the number of folds. The sequences κ, w of length M denote the instances and amplitudes of the discontinuities, respectively. From (2.23), there are $K-1-P$ accessible samples of $\widehat{\Delta r}[n]$ so possible recovery requires $K-1-(2P+1) \geq 2M$. This condition is formalised in the next theorem.

Theorem 2.6 [Fourier Domain Reconstruction, [23]]

Let $x \in \mathcal{B}_\Omega$ be a τ-periodic function. Suppose that we are given K modulo samples of $y[k] = \mathscr{M}_\lambda(x(kT))$ with at most M non-ideal folds. Then a sufficient condition for recovery of $x(t)$ from $y[k]$ (up to a constant) is that,

$$T_{\mathsf{S}} \leq \frac{\tau}{K}, \quad \textit{and} \quad K \geq 2\left(\left\lceil \frac{\Omega\tau}{2\pi} \right\rceil + (M+1)\right).$$

Compared with (2.19), the sampling rate in Theorem 2.6 is favourable. A suitable recovery algorithm called the US-FP was also presented in [23], and it is summarised in Algorithm 2. The idea is illustrated in Fig. 2.16. To estimate the folding times, spectral estimation techniques like Prony's method [88] and the Matrix Pencil [89] can be used. Successful recovery by using the Fourier-domain approach was demonstrated in hardware experiments with the $\mathscr{M}$–ADC, where the signal was contaminated with system noise [50] and non-ideal folds [23]. A recent work utilised the US-FP method for direct estimation of a sparse signal from its modulo measurements, without unfolding [90].

2.3.3 Advantages of USF over Alternative High-Resolution and High-Dynamic-Range Methods

Several existing approaches address high-dynamic-range (HDR) acquisition either algorithmically, by attempting to recover saturated samples after clipping, or at the hardware level, by modifying the signal before quantization. Algorithmic de-clipping methods exploit signal structure, such as bandlimitedness[11] or sparsity, as well as measurement redundancy from oversampling or multiple data streams[13]. However, they operate after saturation has

Algorithm 2: Unlimited Sensing Fourier-Prony (US-FP)

Input: $\{y[k]\}_{k=0}^{K-1}$, τ, P and $M = |\mathcal{M}|$ in (2.17).
Result: $\widetilde{x}(t)$.

1) Compute The DFT $\widehat{\Delta y}[n]$.
2) Define $z[n] = \widehat{\Delta y}[n]\,,\ n \in \mathbb{I}_{K-1} \setminus \mathbb{E}_{P,K-1}$.
3) Fold Estimation in the Fourier Domain
   - $3a$) Define $\boldsymbol{\mathfrak{T}}_M(\mathbf{z})$ using (2.25).
   - $3b$) Find $\mathbf{p}$ such that $\boldsymbol{\mathfrak{T}}_M(\mathbf{z})\,\mathbf{p} = \mathbf{0}$.
   - $3c$) Using $\mathbf{p}$ above, compute the roots $\widetilde{\xi}_m$ of the polynomial $\mathsf{P}_M(z)$ constructed via,
   $$\mathsf{P}_M(z) = \prod_{m=0}^{M-1}\left(1 - \frac{\xi_m}{z}\right) = \sum_{n=0}^{M} p[n] z^{-k}.$$
   - $3d$) Estimate $\widetilde{t}_m = -T_{\mathsf{S}} \angle\widetilde{\xi}_m / \bar{\omega}_0$.
   - $3e$) Estimate $\widetilde{c}[m]$ using least-squares minimization.
4) Estimate $\widetilde{\Delta r}[k]$. This is done by plugging $\{\widetilde{c}[m]\,, \widetilde{t}_m\}_{m\in\mathcal{M}}$ in the first order differences of (2.17), yielding $\widehat{\widetilde{\Delta r}}[n]$ and then performing inverse DFT.
5) Estimate $\widetilde{r}[k]$ by zero padding and anti-difference.
6) Estimate $\widetilde{x}[k] = \widetilde{r}[k] + y[k]$ (up to an unknown constant).
7) Estimate $\widetilde{x}(t)$ by applying sinc-interpolation to $\widetilde{x}[k]$.

$$\boldsymbol{\mathfrak{T}}_M(\mathbf{z}) \overset{\text{def}}{=} \begin{bmatrix} z[0] & z[-1] & \cdots & z[-M] \\ z[1] & z[0] & \cdots & z[1-M] \\ \vdots & \vdots & \ddots & \vdots \\ z[M-1] & z[M-2] & \cdots & z[-1] \end{bmatrix}. \tag{2.25}$$

already caused information loss, so their guarantees depend on restrictive assumptions, including the number of clipped samples, the oversampling factor, or a known sparse model. Moreover, many such methods provide only discrete-to-discrete recovery and lack a general sampling-density criterion for arbitrary HDR signals.

Hardware-based alternatives, such as automatic gain control, companding, and adaptive gain[17], address the dynamic-range limitation by changing the acquisition mechanism itself. Automatic gain control and companding attempt to fit the signal into the ADC range before

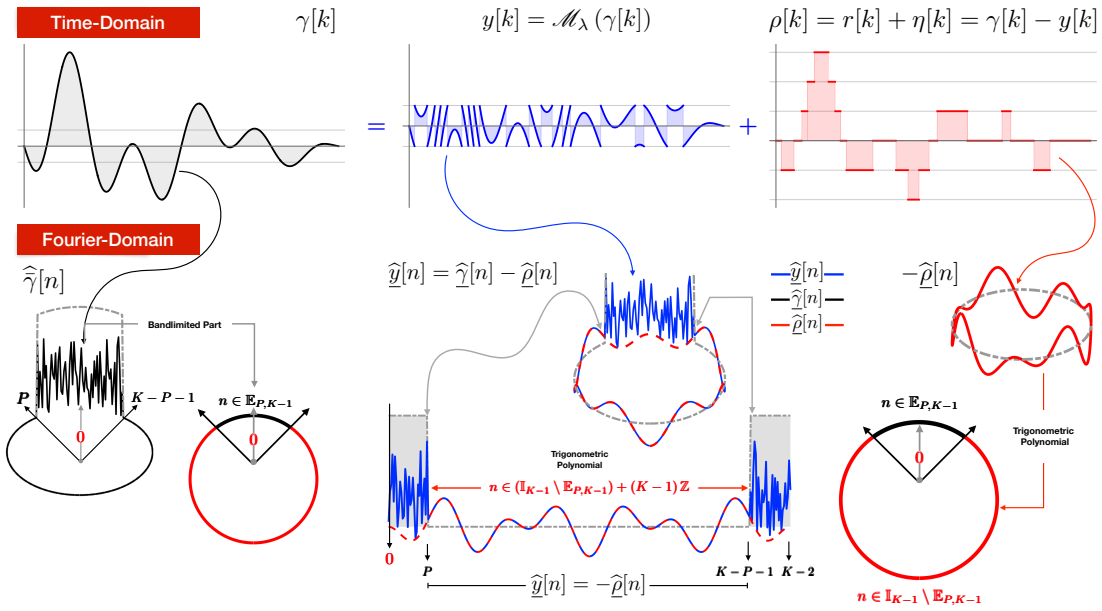


Figure 2.16: Frequency domain partitioning of modulo samples into their bandlimited and residual components $x[k]$ and $r[k]$, respectively (based on [23]).

sampling, but this introduces analog complexity, stability concerns, and sensitivity to non-ideal implementations. Time-varying gain architectures similarly use additional hardware structure and often rely on oversampling or calibration.

For improving digital resolution, Sigma-delta ADCs are particularly relevant in this comparison because, like USF, they trade sampling rate for amplitude resolution: instead of using many bits per sample, they oversample and shape the quantization error[91]. In this sense, sigma-delta conversion can resemble USF at a high level, since both methods exploit oversampling to relax the requirements on the instantaneous quantizer resolution.

The distinction, however, is that sigma-delta and modulo sampling address the dynamic-range problem in different ways. Practical sigma-delta systems have a finite stable input range: if the internal prediction error or loop states become too large, the modulator can overload,

become unstable, or produce large reconstruction errors. Thus, sigma-delta achieves high resolution by using significant oversampling and feedback-based noise shaping, but its performance depends on loop stability, filter design, and the admissible signal range. By contrast, modulo sampling deliberately folds the signal amplitude through a controlled nonlinearity. Values outside the ADC range are not clipped or treated as overload events. Instead, they are mapped back into the measurable range in a structured way that preserves information modulo the folding threshold.

3

Unlimited Sensing of Bandpass Signals

Motivation.

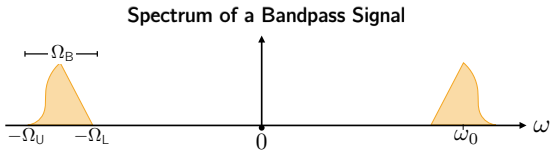


Figure 3.1: The spectrum of a bandpass signal.

Bandpass signals are prevalent in sonar [33, 34], radar [35, 36], ultrasound imaging [37], and optics [38, 39], and often occupy spectral bands that make sampling above their Nyquist rate challenging. Two main approaches to address this issue, which are hardware demodulation and undersampling, reviewed in Chapter 2, do not account for the limitations imposed by the ADC's finite dynamic range and resolution. Here, we aim to develop a USF-based method that enables efficient acquisition of bandpass signals with HDR and high HDRes.

Unlimited Sensing of Bandpass Signals. HDR sampling of bandpass signals has been addressed mostly through ADC implementations [69, 92, 93]. Computational techniques addressing this challenge are less explored, and in particular, bandpass signals have not been explicitly considered within the USF. However, emerging applications such as USF-based radar and computational tomography [87, 29] systems, emphasise the need for such solutions.

A key challenge in achieving HDR bandpass sampling based on the USF is the opposing sampling paradigms. Bandpass sampling operates within the sub-Nyquist region, whereas all of the existing USF techniques reside in the oversampling region[1]. To develop techniques for USF-based acquisition in the undersampling domain, we address the three questions of:

1) Theory: How does aliasing affect the amplitude-folded signal?

[1] At the time this work was published.

2) Algorithm: What are the frameworks to unfold such functions, that are folded in both their range and domain?

3) Practice: Are the proposed frameworks practical, and can they be implemented?

Contributions. This chapter formulates and addresses the problem of HDR sampling and recovery of bandpass signals with modulo non-linearities at sub-Nyquist sampling rates. The main contributions are:

1) Recovery guarantees. Given folded samples of a bandpass signal, the conditions for guaranteed recovery are derived, enabling sub-Nyquist sampling.

2) Algorithmic flexibility for practical solutions. Solutions are derived for different modulo folding architectures, which explain different hardware observations.

3) Numerical simulations and hardware experiments. Validation of the results and algorithms is provided, establishing the practical feasibility and the empirical performance of the recovery methods.

The recovery guarantees are summarised in Fig. 3.2.

Signal Model. Bandpass signals comprise a spectral band of width Ω_{B}, centred around a modulation frequency $\omega_0 > \Omega_{\mathsf{B}}/2$. The signal model is written according to (2.2) with $P = 1$ as

$$x_{\mathsf{BP}}(t) = \varphi_0(t)e^{\jmath\omega_0 t}, \quad \varphi(t) \in \mathbb{R}, \quad \operatorname{supp}(\widehat{\varphi}_0) \in \mathcal{D}_{\frac{\Omega_{\mathsf{B}}}{2}}. \tag{3.1}$$

In the following, we consider real-valued bandpass signals having two symmetric spectral bands w.r.t. the DC frequency $\omega = 0$, as illustrated in Fig. 3.1. This is the model from

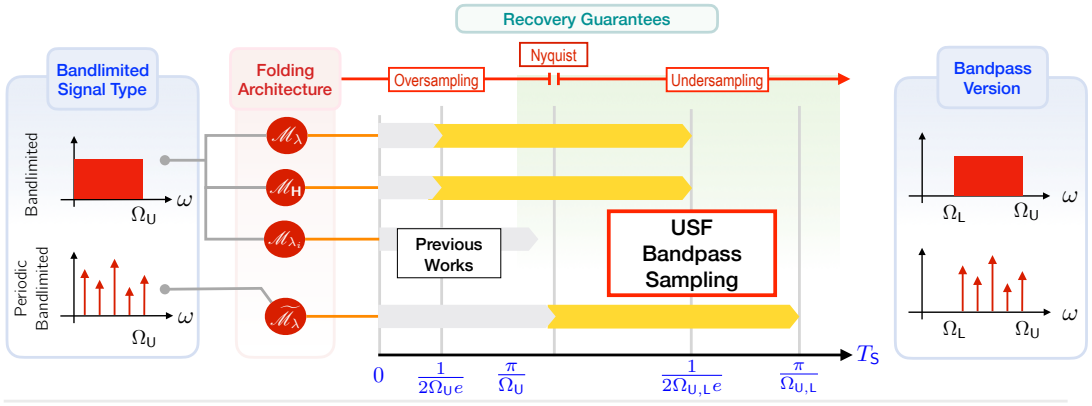


Figure 3.2: The existing results for commonly occurring types of bandlimited signals in the context of the Unlimited Sensing Framework (USF) for different folding architectures denoted by $\mathscr{M}_\lambda, \tilde{\mathscr{M}}_\lambda, \mathscr{M}_\mathsf{H}$, require oversampling. The contribution of this work is the extension of the results for the bandlimited signal type to their corresponding bandpass case, especially in the undersampled regime.

[68], which can be obtained by replacing the modulation $e^{\jmath\omega_0 t}$ in (3.1) with $e^{\jmath\pm\omega_0 t}$, which corresponds to the model (2.2) with $P = 2$ and $\omega_1 = -\omega_0$.

3.2 Towards Computational Demodulation via Modulo Undersampling

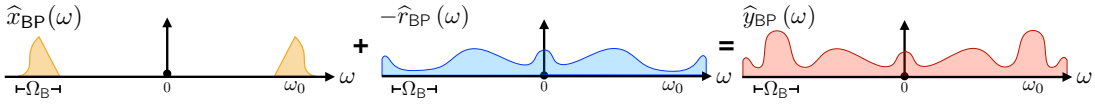


Figure 3.3: The Fourier-domain representation of a modulo signal. The sum of a bandpass component $\widehat{x}_{\mathsf{BP}}(\omega)$ (upper) and a residual component $-\widehat{r}_{\mathsf{BP}}(\omega)$ (middle) composes the modulo signal $\widehat{y}_{\mathsf{BP}}(\omega) = \widehat{x}_{\mathsf{BP}}(\omega) - \widehat{r}_{\mathsf{BP}}(\omega)$ (lower).

Sub-Nyquist sampling of modulo signals may seem unreasonable because modulo folding renders a bandlimited signal, non-bandlimited, as visualised in Fig. 3.3. However, the motivation to investigate modulo undersampling emerged during hardware experiments with amplitude-modulated (AM) bandpass signals; for some choices of sampling rates, undersampling with the $\mathscr{M}$–ADC yielded the baseband signal (φ_0 in (3.1)) without any recovery pro-

cedure. An example is shown in Fig. 3.4. This phenomenon indicates that, despite the non-bandlimitedness of the modulo signal, the underlying bandlimited component preserves its structure under aliasing.

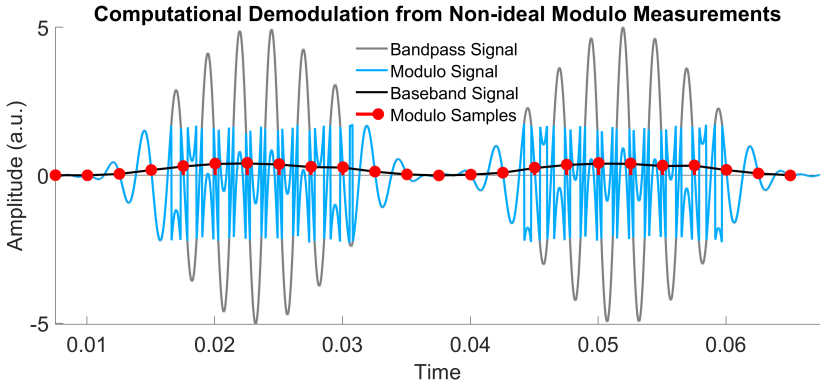


Figure 3.4: An amplitude modulated signal, its associated modulo signal and undersampled modulo samples. The frequencies of the message and carrier signals are $f_{\mathsf{M}} = 35\,\mathrm{Hz}$ and $f_{\mathsf{C}} = 400\,\mathrm{Hz}$, respectively. For a sampling period $T_{\mathsf{S}} = 2.5\,\mathrm{ms}$, modulo samples coincide with underlying baseband signal samples, which directly results in demodulation.

Modulo Undersampling. Consider the bandpass signal $x_{\mathsf{BP}} \in \mathcal{B}_{\mathsf{BP}}$ defined in (3.1), and $x_{\mathsf{BP}}(t) \in \mathbb{R}$. Let $x_{\mathsf{BP}}[k] = x_{\mathsf{BP}}(t)|_{t=kT_{\mathsf{S}}}$, $k \in \mathbb{Z}$ be its uniform samples with $T_{\mathsf{S}} \leq \pi/\Omega_{\mathsf{B}}$, and define the normalized Fourier series $\widehat{x}_{\mathsf{BP}\delta}(\omega) = T_{\mathsf{S}} \sum_{k\in\mathbb{Z}} x_{\mathsf{BP}}[k]\, e^{-\jmath\omega kT_{\mathsf{S}}}$. We can always extract the lowpass filtered signal x via its spectrum,

$$\widehat{x}(\omega) = \mathbb{1}_{\left[-\frac{\Omega_{\mathsf{S}}}{2},\frac{\Omega_{\mathsf{S}}}{2}\right]}(\omega)\, \widehat{x}_{\mathsf{BP}\delta}(\omega)\,, \tag{3.2}$$

Using that $T_{\mathsf{S}} \cdot x_{\mathsf{BP}}[k]$ are the FS coefficients of $\widehat{x}_{\mathsf{BP}\delta}(\omega)$ together with (3.2) we write,

$$\begin{aligned} x_{\mathsf{BP}}[k] &= \frac{1}{2\pi}\int_{-\Omega_{\mathsf{S}}/2}^{\Omega_{\mathsf{S}}/2} \widehat{x}_{\mathsf{BP}\delta}(\omega)\, e^{\jmath\omega kT_{\mathsf{S}}} d\omega \\ &= \frac{1}{2\pi}\int_{-\infty}^{\infty} \mathbb{1}_{\left[-\frac{\Omega_{\mathsf{S}}}{2},\frac{\Omega_{\mathsf{S}}}{2}\right]}(\omega)\, \widehat{x}_{\mathsf{BP}\delta}(\omega)\, e^{\jmath\omega kT_{\mathsf{S}}} d\omega \\ &\overset{(3.2)}{=} \frac{1}{2\pi}\int_{-\infty}^{\infty} \widehat{x}(\omega)\, e^{\jmath\omega kT_{\mathsf{S}}} d\omega = g(t)_{|t=kT_{\mathsf{S}}} \overset{\text{def}}{=} x[k]. \end{aligned} \tag{3.3}$$

The last equation shows that in the sub-Nyquist regime $T_{\mathsf{S}} > T_{\mathsf{NS}}$, the samples $x_{\mathsf{BP}}[k]$ are not unique and represent the lowpass signal $x(t) \neq x_{\mathsf{BP}}(t)$, as illustrated in Fig. 3.5. Using the modulo decomposition property (Theorem 2.4), we decompose both sequences into their modulo and residual components

$$x_{\mathsf{BP}}[k] = y_{\mathsf{BP}}[k] + r_{\mathsf{BP}}[k], \quad x[k] = y[k] + r[k], \quad k \in \mathbb{Z}. \tag{3.4}$$

Subtracting the modulo sequences, we get

$$(y_{\mathsf{BP}} - y)[k] = \underbrace{(x_{\mathsf{BP}} - x)[k]}_{=0 \text{ from (3.3)}} - (r_{\mathsf{BP}} - r)[k]. \tag{3.5}$$

For the LHS of (3.5), since $y_{\mathsf{BP}}[k] \in [-\lambda, \lambda)$ we get that $(y_{\mathsf{BP}} - y)[k] \in (-2\lambda, 2\lambda)$. For the RHS, $(r_{\mathsf{BP}} - r)[k] \in 2\lambda\mathbb{Z}$ so the intersection set between the two sides of (3.5) must be zero. Then,

$$(y_{\mathsf{BP}} - y)[k] = (r - r_{\mathsf{BP}})[k] = 0 \Rightarrow y_{\mathsf{BP}}[k] = y[k], \quad \forall k \in \mathbb{Z}. \tag{3.6}$$

The result in (3.6) shows that by undersampling the modulo bandpass signal, we get the samples of the modulo lowpass signal. The fact that y_{BP} to y is like x_{BP} to x, will play a key role in the derivation of the USF bandpass sampling methods. It reveals that for suitable sampling rates, after unfolding y_{BP} to x. we can recover the bandpass signal x_{BP}.

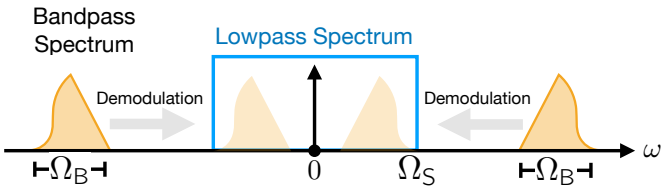


Figure 3.5: Undersampling demodulates the bandpass spectrum into a lowpass region, and the lowpass signal x can be extracted.

3.3 Theory and Algorithms

Problem Formulation. The acquisition pipeline for HDR bandpass sampling is detailed in Chapter 2.3.1 and Fig. 2.9. The input signal x_{BP} is fed into the $\mathscr{M}$–ADC, which performs the modulo folding operation and yields the samples $y_{\mathsf{BP}}[k]$ at rate T_{S}. Signal reconstruction is achieved by solving the inverse problem:

$$\text{given } y_{\mathsf{BP}}[k] = \mathscr{M}_\lambda(x_{\mathsf{BP}}(kT_{\mathsf{S}})), \text{ where } T_{\mathsf{S}} > T_{\mathsf{NS}}, \text{ recover } x_{\mathsf{BP}}(t)\,. \tag{3.7}$$

Based on the modulo undersampling result described above, it is evident that given T_{S}, if:

1. The spectrum of x_{BP} has no spectral overlaps, and
2. The residual samples $r[k]$ can be recovered from $y_{\mathsf{BP}}[k]$,

then we can find $x[k]$ from $y_{\mathsf{BP}}[k]$ and $x_{\mathsf{BP}}(t)$ from $x[k]$. Therefore, the solution strategy is to determine the intersection between the sampling periods where both conditions are satisfied.

3.3.1 Ideal Folding Architecture

For the ideal folding architecture described in Chapter 2.3.2, we derive the following sampling theorem.

Theorem 3.1 [The Unlimited Bandpass Sampling Theorem [94]]

Let $x_{\mathsf{BP}} \in \mathcal{B}_{\mathsf{BP}}$ *with* $\Omega_{\mathsf{B}} = \omega_{\mathsf{U}} - \omega_{\mathsf{L}}$ *and* $y_{\mathsf{BP}}(t) = \mathscr{M}_{\lambda}(x_{\mathsf{BP}}(t))$. *Let* $y_{\mathsf{BP}}[k] = y(kT_{\mathsf{S}})$, $k \in \mathbb{Z}$ *be the modulo samples of* $x_{\mathsf{BP}}(t)$ *at period* $T_{\mathsf{S}} > 0$. *If there exists* $M \in \mathbb{N}$ *such that* T_{S} *satisfies,*

$$\begin{cases} \frac{\pi(M-1)}{\omega_{\mathsf{L}}} \leq T_{\mathsf{S}} \leq \frac{2\pi e(M-1)+1}{2e\omega_{\mathsf{U}}} & M \in 2\mathbb{N}+1 \\ \frac{2\pi eM-1}{2e\omega_{\mathsf{L}}} \leq T_{\mathsf{S}} \leq \frac{\pi M}{\omega_{\mathsf{U}}} & M \in 2\mathbb{N} \end{cases} \tag{3.8}$$

where e *denotes Euler's number, then* $x_{\mathsf{BP}}(t)$ *can be recovered from* $y_{\mathsf{BP}}[k]$ *up to an integer multiple of* 2λ.

Proof. We define the normalized FS with coefficients $y_{\mathsf{BP}}[k]$,

$$\begin{aligned} \widehat{y}_{\mathsf{BP}\delta}(\omega) &\overset{\text{def}}{=} T_{\mathsf{S}} \sum_{k\in\mathbb{Z}} y_{\mathsf{BP}}[k]\, e^{-\jmath\omega kT_{\mathsf{S}}} \\ &\overset{(2.15)}{=} T_{\mathsf{S}} \sum_{k\in\mathbb{Z}} [x_{\mathsf{BP}} - r_{\mathsf{BP}}][k]\, e^{-\jmath\omega kT_{\mathsf{S}}} = [\widehat{x}_{\mathsf{BP}\delta} - \widehat{r}_{\mathsf{BP}\delta}](\omega), \end{aligned} \tag{3.9}$$

Substituting (3.3) and (3.6) into (3.9)

$$\widehat{y}_{\mathsf{BP}\delta}\left(\omega\right)=\widehat{y}_{\delta}\left(\omega\right)=\widehat{x}_{\delta}\left(\omega\right)-\widehat{r}_{\delta}\left(\omega\right), \tag{3.10}$$

where $\widehat{x}_{\delta}\left(\omega\right)$ and $\widehat{r}_{\delta}\left(\omega\right)$ are the FS of $x\left[k\right]$ and $r\left[k\right]$, respectively. From (3.10), we get that $\widehat{y}_{\delta}\left(\omega\right)=\widehat{x}_{\delta}\left(\omega\right)-\widehat{r}_{\delta}\left(\omega\right)$ which means that under the conditions of Theorem 2.5 [48], we can get $x\left[k\right]$ (and hence, $x\left(t\right)$) from $y_{\mathsf{BP}}\left[k\right]$. Moreover, if (2.4) is satisfied then from Lemma 2.2, $x_{\mathsf{BP}}\left(t\right)$ can be obtained and

$$\Omega_{\mathsf{U}}^{x}=\begin{cases}\omega_{\mathsf{U}}-\frac{M-1}{2}\Omega_{\mathsf{S}} & M\in2\mathbb{N}+1\\ \frac{M}{2}\Omega_{\mathsf{S}}-\omega_{\mathsf{L}} & M\in2\mathbb{N}\end{cases}, \tag{3.11}$$

where Ω_{U}^{x} denotes the bandwidth of x. The USF recovery condition for x requires that $\Omega_{\mathsf{S}}\geq4\pi\omega_{\mathsf{U}}^{x}e$. For $M\in2\mathbb{N}+1$, plugging (3.11) allows to re-write the USF recovery condition as

$$\begin{aligned}\Omega_{\mathsf{S}}\geq4\pi\omega_{\mathsf{U}}^{x}e=4\pi e\left(\omega_{\mathsf{U}}-\tfrac{P-1}{2}\Omega_{\mathsf{S}}\right)\\ \Leftrightarrow\Omega_{\mathsf{S}}\geq\tfrac{4\pi e}{1+2\pi e(M-1)}\omega_{\mathsf{U}}.\end{aligned} \tag{3.12}$$

It can be directly shown that $\frac{4\pi e}{1+2\pi e(P-1)}\omega_{\mathsf{U}}\geq\frac{2\omega_{\mathsf{U}}}{P}$, which yields the final condition on Ω_{S},

$$\frac{4\pi e}{1+2\pi e\left(M-1\right)}\omega_{\mathsf{U}}\leq\Omega_{\mathsf{S}}\leq\frac{2\omega_{\mathsf{L}}}{M-1}. \tag{3.13}$$

For $M\in2\mathbb{N}$, using the same derivation as in (3.12), we get $\Omega_{\mathsf{S}}\geq4\pi e\left(\frac{M}{2}\Omega_{\mathsf{S}}-\omega_{\mathsf{L}}\right)$, which yields

$$\frac{2\omega_{\mathsf{U}}}{M}\leq\Omega_{\mathsf{S}}\leq\frac{4\pi e}{2\pi eM-1}\omega_{\mathsf{L}}. \tag{3.14}$$

Using $T_S = \frac{2\pi}{\Omega_\mathsf{S}}$ in 3.13 and 3.14 yields the desired result; then $x_{\mathsf{BP}}(t)$ can be recovered from its modulo samples. ■

As a sanity check, the consistency of Theorem 3.1 with Theorem 2.5 can be verified for $M = 1$. Nevertheless, for $M > 1$, lower sampling periods are allowed by exploiting the bandpass prior. Another property to look at is the upper bound on M. In the conventional bandpass result (see Theorem 2.2), this is given by $M \leq \left\lfloor \frac{\omega_\mathsf{U}}{\Omega_\mathsf{B}} \right\rfloor$. Using (3.13) and (3.14), an equivalent bound for the modulo bandpass case is,

$$\begin{cases} (M-1)2\pi e\Omega_\mathsf{B} \leq \omega_\mathsf{L} & M \in 2\mathbb{N}+1 \\ 2\pi eM\Omega_\mathsf{B} \leq \omega_\mathsf{U} & M \in 2\mathbb{N} \end{cases} \Rightarrow \begin{cases} M \leq \left\lfloor \frac{\omega_\mathsf{L}}{2\pi e\Omega_\mathsf{B}} + 1 \right\rfloor & M \in 2\mathbb{N}+1 \\ M \leq \left\lfloor \frac{\omega_\mathsf{U}}{2\pi e\Omega_\mathsf{B}} \right\rfloor & M \in 2\mathbb{N} \end{cases} \tag{3.15}$$

Since the bound in (3.15) is tighter for the even case, we get that $M \leq \left\lfloor \frac{\omega_\mathsf{U}}{2\pi e\Omega_\mathsf{B}} \right\rfloor$, which is stricter than $M \leq \left\lfloor \frac{\omega_\mathsf{U}}{\Omega_\mathsf{B}} \right\rfloor$. Lastly, we notice that based on Theorem 3.1, whenever

$$\begin{cases} \Omega_\mathsf{S} = \frac{2}{M-1}\omega_\mathsf{L} & M \in 2\mathbb{N}+1 \\ \Omega_\mathsf{S} = \frac{2}{M}\omega_\mathsf{U} & M \in 2\mathbb{N} \end{cases}, \tag{3.16}$$

we get the *baseband relocation* case, where x have minimal bandwidth $\Omega_\mathsf{U}^x = \Omega_\mathsf{B}$. This case is demonstrated in Fig. 2.7(c) for $M = 3$.

Sampling-Based Demodulation of Modulo AM Signals. Among the most common bandpass waveforms that appear in practical applications are double-sideband AM signals [95], characterised by a spectrum comprising two adjacent sidebands mirrored around a carrier frequency. Because of their spectral structure, AM signals can be recovered even when $\Omega_\mathsf{S} = \Omega_\mathsf{B}$

[8]. In this particular case, the result of Theorem 3.1 can be improved based on an even stronger prior, formalised in the next corollary.

Corollary 1 (Unlimited Sampling of AM Signals)**.** *If the side lobes of the bandpass spectrum* $\widehat{x}$ *are symmetric, i.e.,* $\widehat{x}\left(\omega_{\mathsf{L}}+\omega\right)=\widehat{x}\left(\omega_{\mathsf{U}}-\omega\right), \forall \omega \in [0, \Omega_{\mathsf{B}}/2]$*, then* $x_{\mathsf{BP}}(t)$ *can be recovered via Algorithm 3 if there exists* $M_{\mathsf{AM}} \in \mathbb{N}$ *such that*

$$\Omega_{\mathsf{S}}=\frac{\omega_{\mathsf{U}}+\omega_{\mathsf{L}}}{2M_{\mathsf{AM}}} \quad \textit{and} \quad \frac{\omega_{\mathsf{U}}+\omega_{\mathsf{L}}}{\omega_{\mathsf{U}}-\omega_{\mathsf{L}}} \geq 4\pi e M_{\mathsf{AM}}. \tag{3.17}$$

Proof. We require that the sideband copies lead to pairs of lobes that perfectly overlap, such that a pair is centred around the origin. This is true if the LHS equation in (3.17) is satisfied. Furthermore, to ensure that adjacent pairs of lobes do not lead to additional overlaps, which ensures that the information can be recovered, we further assume $\Omega_{\mathsf{S}} \geq \Omega_{\mathsf{B}}$. This leads to the following condition on $\omega_{\mathsf{U}}, \omega_{\mathsf{L}}$:

$$\frac{\omega_{\mathsf{U}}+\omega_{\mathsf{L}}}{\omega_{\mathsf{U}}-\omega_{\mathsf{L}}} \geq 2M_{\mathsf{AM}}. \tag{3.18}$$

Lastly, we compute ω_{U}^{x}, in order to derive a bound for USF. The pair of lobes centred in the origin has width $\omega_{\mathsf{U}}-\omega_{\mathsf{L}}$, therefore its bandwidth is $\omega_{\mathsf{U}}^{x}=\frac{\Omega_{\mathsf{B}}}{2}$. This yields the USF condition $\Omega_{\mathsf{S}} \geq 4\pi e\frac{\Omega_{\mathsf{B}}}{2} = 2\pi e\Omega_{\mathsf{B}}$. By using the LHS equation in (3.17) it is translated in terms of $\omega_{\mathsf{U}}, \omega_{\mathsf{L}}$ that leads to the RHS equation in (3.17). ■

The RHS equation in (3.17) is a tighter condition than (3.18), and thus is enough for input recovery in the case of AM signals. As a particular case, Corollary 2 has implications for sinusoids, which can be viewed as AM signals with $\Omega_{\mathsf{B}} \to 0$. While [96] demonstrated

Algorithm 3: Unlimited Sampling of Bandpass Signals

Input: $y_{\mathsf{BP}}[k]$, λ,$\beta_{x_{\mathsf{BP}}} = ||x_{\mathsf{BP}}||_{\infty}$, ω_{L}, and ω_{U}.
Result: Bandpass function, $\widetilde{x}_{\mathsf{BP}}(t)$.

1) Compute Ω_{U}^{x} using (3.11).

2) Compute $N = \left\lceil \frac{\log\lambda - \log\beta_{x_{\mathsf{BP}}}}{\log\left(T_{\mathsf{S}}\Omega_{\mathsf{U}}^{x}e\right)} \right\rceil$.

3) Compute $\left(\Delta^{N}y\right)[k] \overset{(3.6)}{=} \left(\Delta^{N}y_{\mathsf{BP}}\right)[k]$.

4) Compute $\left(\Delta^{N}r\right)[k] = \left(\mathscr{M}_{\lambda}(\Delta^{N}y) - \left(\Delta^{N}y\right)\right)[k]$.
Set $s_{(0)}[k] = \left(\Delta^{N}r\right)[k]$.

5) For $n = 0 : N-2$

(i) $s_{(n+1)}[k] = \mathsf{S}\left(s_{(n)}\right)[k]$, $\quad \mathsf{S} : \{s[k]\}_{k\in\mathbb{Z}^{+}} \to \sum_{m=1}^{k} s[m]$.

(ii) $s_{(n+1)}[k] = 2\lambda \left\lceil \frac{\lfloor s_{(n+1)}/\lambda \rfloor}{2} \right\rceil$ (rounding to $2\lambda\mathbb{Z}$).

(iii) Compute $\kappa_{(n)} = \left\lfloor \frac{\mathsf{S}^{2}(\Delta^{n}r)[1] - \mathsf{S}^{2}(\Delta^{n}r)[\frac{6\beta_{x_{\mathsf{BP}}}}{\lambda}+1]}{12\beta_{x_{\mathsf{BP}}}} + \frac{1}{2} \right\rfloor$.

(iv) $s_{(n+1)}[k] = s_{(n+1)}[k] + 2\kappa_{(n)}$.

end

6) $\widetilde{x}[k] = \mathsf{S}\left(s_{(N-1)}\right)[k] + y_{\mathsf{BP}}[k] + 2m\lambda$, $m \in \mathbb{Z}$.

7) Compute $\widehat{x}_{\delta}(\omega) = T_{\mathsf{S}} \sum_{k\in\mathbb{Z}} \widetilde{x}[k]\, e^{-\jmath\omega k T_{\mathsf{S}}}$.

8) Estimate $\widetilde{x}_{\mathsf{BP}}(t)$ from $\widehat{x}_{\delta}(\omega)$ using (2.5) and M from (3.8).

that these signals allow lower sampling rates than in the general bandlimited case, under the conditions of Corollary 1, this improvement can be further enhanced.

3.3.2 Generalized Folding Architecture

To be able to accommodate nonlinear effects occurring during modulo acquisition, such as hysteresis, the generalized modulo architecture $\mathscr{M}_{\mathsf{H}}$ described in Chapter 2.3.2 is considered for the forward model with $T_{\mathsf{S}} > 0$. The output samples are modelled as,

$$y_{\mathsf{BP}}[k] = \mathscr{M}_{\mathsf{H}}\left(x_{\mathsf{BP}}\left(kT_{\mathsf{S}}\right)\right) = \left(x_{\mathsf{BP}} + r_{\mathsf{BP}}\right)[k] \overset{(3.3)}{=} \left(x + r_{\mathsf{BP}}\right)[k], \tag{3.19}$$

where the residual sequence is modeled as $r_{\mathsf{BP}}[k] = \sum_{p\in\mathbb{Z}} s_p \varepsilon_0\left(kT_{\mathsf{S}} - \tau_p\right)$ based on (2.18). By replacing the ideal modulo with $\mathscr{M}_{\mathsf{H}}(\cdot)$, the inverse problem (3.7) is changed accordingly.

Assuming negligible transient ($\alpha = 0$), it gives $\varepsilon_0\left(t - \tau_p\right) = 2\lambda_h \mathbb{1}_{[\tau_p,\infty)}(t)\big|_{t=kT_{\mathsf{S}}} \in \{0, 2\lambda_h\}$. Therefore, samples $x[k]$ (3.19) can be recovered up to $2\lambda_h\mathbb{Z}$ using a variation of US-Alg detailed in Algorithm 1, as explained next. Using the same reasoning as in US-Alg, $\forall k \in \mathbb{Z}$ we require that $\left|\Delta^N\left(x+\eta\right)[k]\right| < \lambda_h$, which is true if $\left(T_{\mathsf{S}}\Omega e\right)^N \|g\|_\infty < \lambda_h$. Subsequently, $\widetilde{x}[k] = x[k] + 2M\lambda_h$, $M \in \mathbb{Z}$, is computed using $\Delta^N x[k] = \mathscr{M}_{\lambda_h}\left(\Delta^N y[k]\right)$. In the following, we give a theorem guaranteeing recovery from generalized modulo data.

Theorem 3.2 [Generalized Modulo Recovery]

Let $x_{\mathsf{BP}} \in \mathsf{PW}_{[\omega_{\mathsf{L}},\omega_{\mathsf{U}}]}$ *and* $y_{\mathsf{BP}}[k] = \mathscr{M}_{\mathsf{H}}(x_{\mathsf{BP}}(t))|_{t=kT_{\mathsf{S}}}$ *be the generalized modulo samples of* x_{BP} *with sampling period* $T_{\mathsf{S}} > 0$. *We assume that there exists* $M \in \mathbb{N}$ *such that* T_{S} *satisfies* (3.8). *Then* x_{BP} *can be recovered from* $\left(\Delta^N y_{\mathsf{BP}}\right)[k]$ *up to an integer multiple of* $2\lambda_h$, *where* N *is defined as*

$$N = \left\lceil \frac{\log \lambda_h - \log \beta_g}{\log\left(T_{\mathsf{S}}\Omega_{\mathsf{U}}^x e\right)} \right\rceil, \tag{3.20}$$

and Ω_{U}^x *is defined in* (3.11).

Proof. From (3.19) we get that $\Delta^N y_{\mathsf{BP}} = \Delta^N (x + r_{\mathsf{BP}})$, where $x[k] = x(t)|_{t=kT_{\mathsf{S}}}$ and x is defined in (3.2). It can be directly verified that the value of N in (3.20) guarantees $(T_{\mathsf{S}}\Omega e)^N \|x\|_\infty < \lambda_h$, which was also shown in [48] for the case $h = 0$. Similarly, given that $r_{\mathsf{BP}}[k] \in \{2m\lambda_h \mid m \in \mathbb{Z}\}$, it can be directly shown that $\Delta^N r_{\mathsf{BP}}[k] \in \{2m\lambda_h \mid m \in \mathbb{Z}\}$. Then, using a similar reasoning as for US-Alg, we get that $\mathscr{M}_{\lambda_h}\left(\Delta^N r_{\mathsf{BP}}[k]\right) = 0$ and thus $\left(\Delta^N x\right)[k] = \mathscr{M}_{\lambda_h}\left(\Delta^N y_{\mathsf{BP}}[k]\right)$. Further on, the US-Alg can be used to recover $x(t)$. Even though the recovery of $x(t)$ has no direct link to the bandpass property of $x_{\mathsf{BP}}(t)$, this is required to get back $x_{\mathsf{BP}}(t)$ from $g(t)$. As shown in Theorem 3.1, this is possible if (3.8) is satisfied. ■

3.3.3 Non-Ideal Folding Architecture

The Fourier-domain-based recovery procedure in Chapter 2.3.2, which is designed for the non-ideal folding architecture, exploits both the parametric structure of the residual signal model (2.17), and the partitioning of the modulo signal in the frequency domain. Since for

bandpass signals $\widehat{x}_{\mathsf{BP}}(\omega) = 0, \forall \omega \in \mathbb{R}, |\omega| \notin (\omega_{\mathsf{L}}, \omega_{\mathsf{U}})$, two partitioning intervals can be leveraged in that case. In fact, the bandpass prior interval of $\omega \in (-\omega_{\mathsf{L}}, \omega_{\mathsf{L}})$ can be used to recover the residual signal's parameters without the need for demodulation, for any $\Omega_{\mathsf{S}} > 2\omega_{\mathsf{U}}$. Qualitatively, this can be observed in Fig. 3.3. However, for further reduction of the sampling frequency, demodulation will be necessary.

Fourier-Domain Partitioning of Modulo Bandpass Signals. To derive the modulo bandpass sampling conditions in the discrete frequency domain, we use the discrete Fourier transform (DFT). The function $x_{\mathsf{BP}}(t)$ is considered to be τ-periodic . We also assume that $T_{\mathsf{S}} = \frac{\tau}{K}$, where $K \in \mathbb{Z}$ denotes the number of samples, and without reducing the generality, we assume that $\omega_{\mathsf{L}}, \omega_{\mathsf{U}}$ are integer multiples of $\frac{2\pi}{\tau}$. In terms of the K–length DFT of y_{BP}, (3.10) becomes,

$$\begin{aligned}\widehat{y}_{\mathsf{BP}}[n] &= T_{\mathsf{S}} \sum_{k=0}^{K-1} y_{\mathsf{BP}}[k]\, e^{-\jmath \frac{2\pi}{K} kn} = \widehat{y}_{\mathsf{BP}\delta}(\omega)\big|_{\omega=\frac{2\pi}{\tau}n} \\ &= \left(\widehat{x}_{\delta} - \widehat{r}_{\mathsf{BP}\delta}\right)(\omega)\big|_{\omega=\frac{2\pi}{\tau}n} = \widehat{x}[n] - \widehat{r}_{\mathsf{BP}}[n].\end{aligned}$$

Moreover, $x(t)$ defined in (3.2) is τ-periodic as well, given that its frequencies are obtained by shifting $\widehat{x}_{\mathsf{BP}}(\omega)$ by integer multiples of $\Omega_{\mathsf{S}} = \frac{2\pi}{T_{\mathsf{S}}}$.

We assume $\omega_{\mathsf{L}} > 0$, therefore $\omega_{\mathsf{L}} \geq 2\pi/\tau$. Define $Q_{\mathsf{L}}, Q_{\mathsf{U}} \in \mathbb{Z}$ as

$$Q_{\mathsf{L}} \stackrel{\text{def}}{=} \frac{K\omega_{\mathsf{L}}}{\Omega_{\mathsf{S}}}, \quad Q_{\mathsf{U}} \stackrel{\text{def}}{=} \frac{K\omega_{\mathsf{U}}}{\Omega_{\mathsf{S}}}, \tag{3.21}$$

we get $Q_{\mathsf{L}} \geq 1$. We know that the DFT coefficients computed from the samples $x[k] = x(t)|_{t=kT_{\mathsf{S}}}$ map to the magnitudes of $\widehat{x}(\omega)\big|_{\omega=n\frac{2\pi}{\tau}=n\frac{\Omega_{\mathsf{S}}}{K}}$. It then follows from (3.11) and

(3.21) that the indices of the passband frequencies in $\widehat{x}\,[n]$, the DFT of $x(t)$, are contained in

$$\{-Q^x_{\mathsf{U}}, Q^x_{\mathsf{U}}+1, \ldots, -Q^x_{\mathsf{L}}\} \cup \{Q^x_{\mathsf{L}}, Q^x_{\mathsf{L}}+1, \ldots, Q^x_{\mathsf{U}}\}\,, \text{ where}$$

$$Q^x_{\mathsf{U}} = \begin{cases} Q_{\mathsf{U}} - \frac{M-1}{2}K & M \in 2\mathbb{N}+1 \\ \frac{M}{2}K - Q_{\mathsf{L}} & M \in 2\mathbb{N} \end{cases} \text{ and, } \quad Q^x_{\mathsf{L}} = Q^x_{\mathsf{U}} - Q_{\mathsf{B}}, \tag{3.22}$$

and $Q_{\mathsf{B}} \stackrel{\text{def}}{=} Q_{\mathsf{U}} - Q_{\mathsf{L}}$. The number of periods Ω_{S} within $(-\omega_{\mathsf{L}}, \omega_{\mathsf{L}})$ is $M-1 = \frac{2\omega_{\mathsf{L}}}{\Omega_{\mathsf{S}}} \in \mathbb{N}$. We have that $x\,[k] = x_{\mathsf{BP}}\,[k]$ via (3.3). Then, using the periodicity of the DFT, that is $\widehat{y}_{\mathsf{BP}}\,[K-q] = \widehat{y}_{\mathsf{BP}}\,[q]\,, \forall q \in \{0,1,\ldots,K\}$, the following holds

$$\widehat{y}_{\mathsf{BP}}\,[n] = \begin{cases} \widehat{x}\,[n] - \widehat{r}_{\mathsf{BP}}\,[n]\,, & n \in \mathbb{E}_{[Q^x_{\mathsf{L}}, Q^x_{\mathsf{U}}],K} \\ -\widehat{r}_{\mathsf{BP}}\,[n]\,, & n \in \mathbb{I}_K \setminus \mathbb{E}_{[Q^x_{\mathsf{L}}, Q^x_{\mathsf{U}}],K} \end{cases}$$

where the set $\mathbb{E}_{[Q^x_{\mathsf{L}}, Q^x_{\mathsf{U}}],K}$ is given by, $\mathbb{E}_{[Q^x_{\mathsf{L}}, Q^x_{\mathsf{U}}],K} = [Q^x_{\mathsf{L}}, Q^x_{\mathsf{U}}] \cup [K - Q^x_{\mathsf{U}}, K - Q^x_{\mathsf{L}}]$. The partition is schematically illustrated in Fig. 3.6. As can be seen, the two sets on which the residual and the lowpass signals can be separated are,

$$\mathbb{F}_{\mathsf{BP}} = \begin{cases} [Q^x_{\mathsf{U}}+1, K - Q^x_{\mathsf{U}} - 1] & \text{(Outer Set)} \\ [0, Q^x_{\mathsf{L}} - 1] \cup [K - Q^x_{\mathsf{L}} - 1, K-1] & \text{(Inner Set)} \end{cases}. \tag{3.23}$$

A sampling density criterion that enables recovery based on the two sets is given in the next theorem.

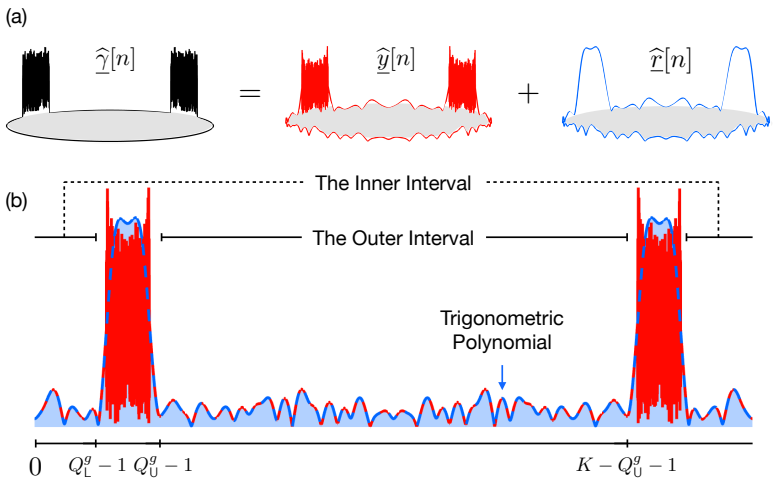


Figure 3.6: The partitioning of a bandpass signal into its modulo (red) and residual (blue) components in the discrete Fourier-domain. (a) Decomposition of the bandpass spectra into the modulo and residual components. (b) The inner and outer intervals as defined in (3.23) on a single DFT period.

Theorem 3.3 [Bandpass Fourier-Domain Recovery]

Let $x_{\mathsf{BP}} \in \mathcal{B}_{\mathsf{BP}}$ *be a* τ*-periodic function. Suppose that we are given* K *modulo samples of* $y_{\mathsf{BP}}[k] = \widetilde{\mathscr{M}_{\lambda}}(x_{\mathsf{BP}}(kT_{\mathsf{S}}))$*, at sampling period* $T_{\mathsf{S}} = \frac{\tau}{K} > 0$*, folded at most* M *times. If there exists* $M \in \mathbb{N}$ *such that* T_{S} *satisfies,*

$$\begin{cases} \frac{(M-1)\tau}{2Q_{\mathsf{L}}} \leq T_{\mathsf{S}} \leq \frac{M\tau}{2(Q_{\mathsf{U}}+M+1)}, & M \in 2\mathbb{N}+1 \\ \frac{(M-1)\tau}{2(Q_{\mathsf{L}}-M-1)} \leq T_{\mathsf{S}} \leq \frac{M\tau}{2Q_{\mathsf{U}}}, & M \in 2\mathbb{N} \end{cases}$$

or,

$$\begin{cases} \frac{(M-1)\tau}{2(Q_{\mathsf{L}}-M-1)} \leq T_{\mathsf{S}} \leq \frac{M\tau}{2Q_{\mathsf{U}}}, & M \in 2\mathbb{N}+1 \\ \frac{(M-1)\tau}{2Q_{\mathsf{L}}} \leq T_{\mathsf{S}} \leq \frac{M\tau}{2(Q_{\mathsf{U}}+M+1)}, & M \in 2\mathbb{N} \end{cases}, \tag{3.24}$$

and $Q_{\mathsf{L}} > M+1$ *for* $M \in 2\mathbb{N}$ *or* $M \in (2\mathbb{N}+1) \setminus \{1\}$ *in* (3.24)*. Then,* $x_{\mathsf{BP}}(t)$ *can be*

recovered from $y_{\mathsf{BP}}[k]$ *up to* $2\lambda\mathbb{Z}$.

Proof. We start from (2.4) and multiply by K to get,

$$\left(\frac{M-1}{2}\right)K \leq \frac{K\omega_{\mathsf{L}}}{\Omega_{\mathsf{S}}} \leq \frac{K\omega_{\mathsf{U}}}{\Omega_{\mathsf{S}}} \leq \left(\frac{M}{2}\right)K. \tag{3.25}$$

Re-arranging (3.25) with respect to the number of samples K,

$$\frac{2}{M}\frac{K\omega_{\mathsf{U}}}{\Omega_{\mathsf{S}}} \leq K \leq \frac{2}{M-1}\frac{K\omega_{\mathsf{L}}}{\Omega_{\mathsf{S}}}. \tag{3.26}$$

Then, using (3.21), we get an equivalent of the bandpass sampling condition (2.4) in the discrete frequency domain

$$\frac{2Q_{\mathsf{U}}}{M} \leq K \leq \frac{2Q_{\mathsf{L}}}{M-1}. \tag{3.27}$$

Next, to recover the bandpass samples, we note that for a modulo sequence with M folds, the first order difference of the residual, Δr, is a $2M$-parametric signal. Its recovery requires $2M+1$ samples in the outer set (3.23), for which $\widehat{y}_{\mathsf{BP}}[n] = -\widehat{r}_{\mathsf{BP}}[n]$. This is guaranteed by $K - 2Q^x_{\mathsf{U}} - 1 \geq 2M+1$. By substituting with Q^x_{U} from (3.3.3) and isolating K we get,

$$\begin{cases} K \geq \frac{2(Q_{\mathsf{U}}+M+1)}{M} & M \in 2\mathbb{N}+1 \\ K \leq \frac{2(Q_{\mathsf{L}}-M-1)}{M-1} & M \in 2\mathbb{N} \end{cases}.$$

For every $M \geq 0, M > 0$, we get that $\frac{2(Q_{\mathsf{U}}+M+1)}{M} \geq \frac{2Q_{\mathsf{U}}}{M}$ and $\frac{2(Q_{\mathsf{L}}-M-1)}{M-1} \leq \frac{2Q_{\mathsf{L}}}{M-1}$. Integration with the bound in (3.27) and substitution $K = \tau/T_{\mathsf{S}}$ yields the first condition in (3.24). For the set $[0, Q^x_{\mathsf{L}}-1] \cup [K - Q^x_{\mathsf{L}} - 2, K-2]$ we require that $2\left(Q^x_{\mathsf{L}}-1\right) \geq 2M$.

We use Q_{L}^{x} from (3.3.3) and isolate K to get,

$$\begin{cases} K \leq \frac{2(Q_{\mathsf{L}}-M-1)}{M-1} & M \in 2\mathbb{N}+1 \\ K \geq \frac{2(Q_{\mathsf{U}}+M+1)}{M} & M \in 2\mathbb{N} \end{cases}. \tag{3.28}$$

As in the outer set case, we integrate (3.28) with the bound in (3.27), and replace $K = \tau/T_{\mathsf{S}}$ to get the sampling condition in (3.24). For T_{S} that satisfies (3.24) for some $M \in \mathbb{N}$, $x_{\mathsf{BP}}(t)$ can be recovered from its modulo samples by Algorithm 4. ■

- As a sanity check, it is verified that in the case of a bandlimited signal ($Q_{\mathsf{U}} = Q_{\mathsf{B}}$), the result is that $2(M+1)$ modulo samples beyond the maximal non-zero frequency of the signal are needed, as expected from Theorem 2.6.

- For $M = 1$, the possibility of reconstruction based on the inner set samples is independent of the sampling period and requires $Q_{\mathsf{L}} \geq M+1$.

- The number of folds that can be recovered decreases when M gets larger, as more replicas of the bandwidth occupy the outer set (even M case) or the inner set (odd M case).

- For a given M, the outer set (even M case) or the inner set (odd M case) shrinks as K increases. Consequently, a larger M would require lowering the sampling period for recovery based on a specific interval. This implies that in modulo undersampling, the sampling period must be carefully optimised based on the recovery strategy, taking into account the exploited interval and the parity of M.

Similar to Corollary 1, the prevalence of AM signals and their spectral structure motivates the proof of the next corollary for non-ideal modulo bandpass sampling.

Algorithm 4: Bandpass Recovery in the Fourier-Domain

Input: $\{y_{\mathsf{BP}}[k]\}_{k=0}^{K-1}, \tau, \omega_{\mathsf{L}}, \omega_{\mathsf{U}}$, and $M = |\mathcal{M}|$ (2.17)
Result: Bandpass function, $\widetilde{x}_{\mathsf{BP}}(t)$.

1) Compute $\widehat{\Delta y}_{\mathsf{BP}}[n]$, the DFT of Δy_{BP}.
2) Compute Q_{L}^x or Q_{U}^x using (3.3.3).
3) Define $\widehat{\Delta r}[n] \overset{\text{def}}{=} -\widehat{\Delta y}_{\mathsf{BP}}[n] \overset{(3.6)}{=} -\widehat{\Delta y}[n]$, where $n \in \mathbb{F}_{\mathsf{BP}}$ (3.23).
4) Use spectral estimation to estimate $\widetilde{\Delta r}[k]$ [23].
5) Estimate $\widetilde{r}[k] = \sum_{m=1}^{k} \widetilde{\Delta r}[m]$ (up to an unknown constant), and compute $\widetilde{x}[k] = \widetilde{r}[k] + y_{\mathsf{BP}}[k]$.
6) Compute $\widehat{x}_\delta(\omega) = T_{\mathsf{S}} \sum_{k\in\mathbb{Z}} x[k] e^{-\jmath\omega k T_{\mathsf{S}}}$.
7) Estimate $\widetilde{x}_{\mathsf{BP}}(t)$ from $\widehat{x}_\delta(\omega)$ using (2.5) and M from (3.24).

Corollary 2 (Fourier-Domain Recovery for AM Signals)**.** *If $x_{\mathsf{BP}} \in \mathcal{B}_{\mathsf{BP}}$ is a τ-periodic function such that the side lobes of $\widehat{x}$ are symmetric, i.e., $\widehat{x}(\omega_{\mathsf{L}} + \omega) = \widehat{x}(\omega_{\mathsf{U}} - \omega), \forall \omega \in [0, \Omega_{\mathsf{B}}/2]$, then $x_{\mathsf{BP}}(t)$ can be recovered from K modulo samples folded at most M times via Algorithm 4 if there exists $M_{\mathsf{AM}} \in \mathbb{N}$ such that $\Omega_{\mathsf{S}} = \frac{2\pi}{KT_{\mathsf{S}}} = \frac{\omega_{\mathsf{U}}+\omega_{\mathsf{L}}}{2M_{\mathsf{AM}}}$ and*

$$\Omega_{\mathsf{B}} \leq \Omega_{\mathsf{S}} \leq \frac{4\pi(Q_{\mathsf{L}} - M - 1)}{\tau(2M_{\mathsf{AM}} - 1)}. \tag{3.29}$$

Proof. Just as in Corollary 1, $\Omega_{\mathsf{S}} = (\omega_{\mathsf{U}} + \omega_{\mathsf{L}}) / (2M_{\mathsf{AM}})$ guarantees perfect overlapping of the spectral lobes. For recovery to work, we further require that $\Omega_{\mathsf{B}} \leq \Omega_{\mathsf{S}}$. Here, only the outer set $[Q_{\mathsf{U}}^x + 1, K - Q_{\mathsf{U}}^x - 2]$ can be used and hence, we require that $(K - 2Q_{\mathsf{U}}^x - 2) \geq 2M$. Then, the RHS of (3.29) follows by substituting Q_{U}^x (3.3.3) (with $M = 2M_{\mathsf{AM}}$) and $K = (\Omega_{\mathsf{S}}\tau)/(2\pi)$. ∎

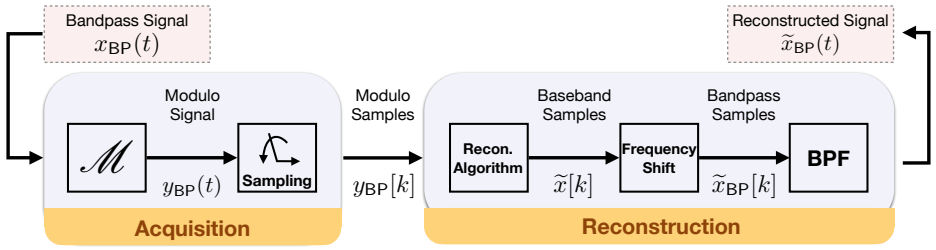


Figure 3.7: Modulo bandpass acquisition and reconstruction pipeline.

3.4 Experiments

The theoretical results presented in Section 3.3 are validated in numerical experiments, and the potential of the modulo undersampling technique is demonstrated via hardware experiments, including the computational demodulation and the recovery of a bandpass signal from its modulo samples.

3.4.1 Numerical Experiments

As the most practical use case, we consider the case of baseband relocation. In the experiments, the bandwidth of the positive Fourier-domain coefficients is $\Omega_{\mathsf{B}} = \pi$, and their complex values are generated randomly so $\widehat{x}_{\mathsf{BP}}(\omega) = 100\mathsf{U}_0 + \jmath 120\mathsf{U}_1, \forall \omega \in [\omega_{\mathsf{L}}, \omega_{\mathsf{U}}]$, where $(\mathsf{U}_0, \mathsf{U}_1) \in (0,1) \times (0,1)$ are sampled from a uniform distribution. The negative Fourier-domain coefficients are the complex conjugate of the positive Fourier-domain coefficients. The bandpass signal is normalized so $||x_{\mathsf{BP}}||_\infty = 1$. The experimental pipeline follows the block diagram in Fig. 3.7. The modulo of the bandpass signal, $y_{\mathsf{BP}}(t)$ is sampled at period T_{S} for a time interval τ to produce a sequence of $K = \tau/T$ modulo samples $y_{\mathsf{BP}}[k]$, and the samples that are recovered by Algorithm 3 and Algorithm 4 are denoted by $\widetilde{x}_{\mathsf{BP}}^{\mathsf{US}}[k]$ and $\widetilde{x}_{\mathsf{BP}}^{\mathsf{FP}}[k]$, respectively. Both algorithms recover the signal up to an additive constant of $2\lambda\mathbb{Z}$.

Table 3.1: Hardware Experiments–Summary of Parameters and Performance

Exp.	Fig. No.	T_{S} (ms)	K	τ (ms)	ω_{L}(rad/s)	ω_{U}(rad/s)	ρ	A_{M}	Ω_{M}(rad/s)	θ_{M}(rad)	ω_0(rad/s)	θ_{C}(rad)	$\mathcal{E}\left(x,\widetilde{x}\right)$
0	Fig. 3.4	2.5	24	59.8	2.29×10^3	2.73×10^3	2.49	-2.502	219.91	1.147	2.51×10^3	-0.17	1.7×10^{-3}
1	Fig. 3.9	10	30	299	584.33	672.30	3.77	3.72	43.98	2.644	628.31	-0.93	7.1×10^{-3}
2	Fig. 3.10	2.5	24	59.8	2.29×10^3	2.73×10^3	2.6	2.47	216	-1.57×10^{-2}	2.5×10^3	-1.57×10^{-2}	4.26×10^{-4}

This factor is estimated from the ground-truth samples $x_{\mathsf{BP}}[k]$, and the MSE between the signals is measured and denoted by $\mathcal{E}\left(x_{\mathsf{BP}},\widetilde{x}_{\mathsf{BP}}^{\mathsf{US}}\right)$ and $\mathcal{E}\left(x_{\mathsf{BP}},\widetilde{x}_{\mathsf{BP}}^{\mathsf{FP}}\right)$.

—• **Time-Domain Recovery.** The evaluation on this experiment is based on 1000 random realizations of a bandpass signal $x_{\mathsf{BP}} \in \mathcal{B}_{(50\pi,51\pi)}$ with $\lambda \sim \mathsf{U}(0.05, 0.1)$. According to (2.19), the sampling period should satisfy $T_{\mathsf{S}} \leq T_{\mathsf{US}}^{\mathsf{BP}} = 1/(102\pi e) \approx 1.1\times10^{-3}$. However, according to Theorem 3.1 with $M = 5$, recovery is still possible for $0.080 \leq T_{\mathsf{S}} \leq 0.085$. We set $T_{\mathsf{S}} = 0.080$ to achieve baseband relocation in (3.16). The maximal reconstruction error achieved by Algorithm 3 is $\mathcal{E}\left(x_{\mathsf{BP}},\widetilde{x}_{\mathsf{BP}}^{\mathsf{US}}\right) = 8.54\times10^{-32}$. This verifies the validity of Theorem 3.1, and shows a factor of $8\pi e$ reduction in the required sampling period for bandpass signals recovery. The modulo samples of $x_{\mathsf{BP}}(t)$ with $\lambda = 0.07$ and the reconstruction using Algorithm 3 with $N = 3$ are shown in Fig. 3.8.

—• **Fourier-Domain Recovery.** To test the utility of our numerical algorithm, 1000 random realizations of the signal $x_{\mathsf{BP}} \in \mathcal{B}_{(199\pi,200\pi)}$ and $\lambda \sim \mathsf{U}(0.02, 0.1)$ were generated. The maximum number of detected folds was $M = 259$. Without undersampling, recovery of x_{BP} using the US-FP algorithm requires a sampling period smaller than 4.4×10^{-3}. Based on (3.24), we observe that with $M = 2$ the sampling period can be eased to $5.8\times10^{-3} \leq T_{\mathsf{S}} \leq 10\times10^{-3}$. We set $T_{\mathsf{S}} = 10\times10^{-3}$, which relocates the bandpass signal to a baseband position (3.16). The maximal reconstruction error using Algorithm 4 is $\mathcal{E}\left(x_{\mathsf{BP}},\widetilde{x}_{\mathsf{BP}}^{\mathsf{FP}}\right) = 6.39\times10^{-32}$.

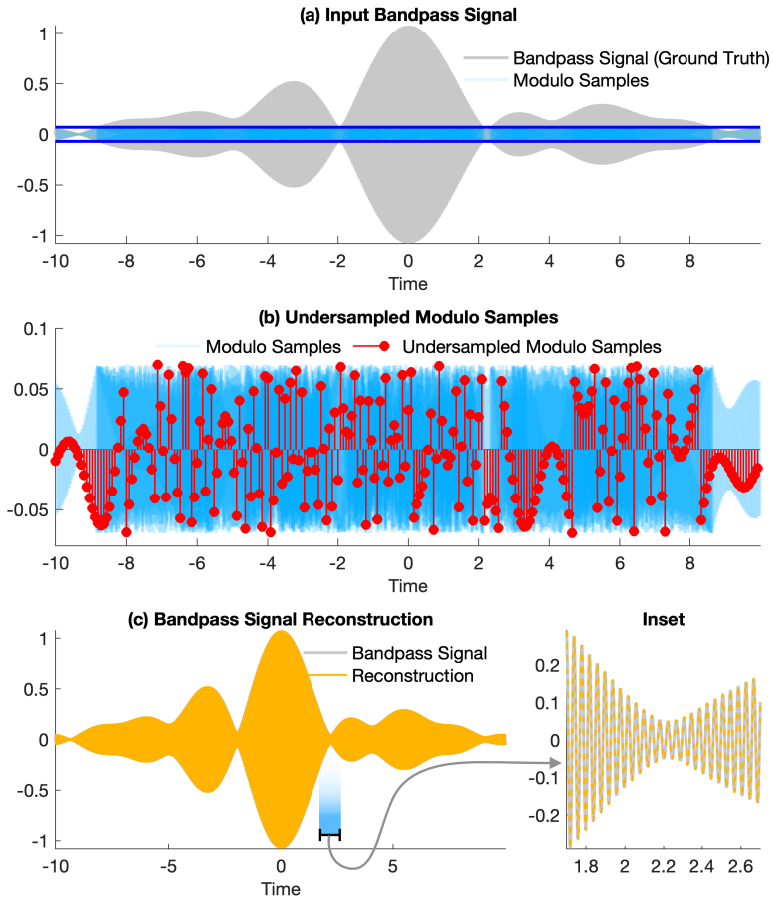


Figure 3.8: Reconstruction of a bandpass signal with $\omega_{\mathsf{L}} = 50\pi, \omega_{\mathsf{U}} = 51\pi$ from its modulo samples at $T_{\mathsf{S}} = 8 \times 10^{-2}$, where $\lambda = 0.07, M = 5$. Reconstruction with Algorithm 3 achieves $\mathcal{E}\left(x_{\mathsf{BP}}, \widetilde{x}_{\mathsf{BP}}^{\mathsf{US}}\right) = 2.06 \times 10^{-34}$.

3.4.2 Hardware Experiments

Experimental Protocol. The results for non-ideal modulo architectures can be validated via hardware experiments, by achieving computational demodulation and recovery of a bandpass signal from its modulo samples. The input signal follows,

$$x_{\mathsf{BP}}(t) = A_{\mathsf{M}}\left(1 + \cos\left(\Omega_{\mathsf{M}} t + \theta_{\mathsf{M}}\right)\right) \sin\left(\omega_0 t + \theta_{\mathsf{C}}\right) \tag{3.30}$$

where $\{A_{\mathsf{M}}, \Omega_{\mathsf{M}}, \theta_{\mathsf{M}}\}$ are the amplitude, frequency and phase of a message wave, and $\{\omega_0, \theta_{\mathsf{C}}\}$ are the frequency and phase of a carrier wave. The minimal and maximal frequencies of the bandpass signal in (3.30) are $\omega_{\mathsf{L}} = \omega_0 - \Omega_{\mathsf{M}}$ and $\omega_{\mathsf{U}} = \omega_0 + \Omega_{\mathsf{M}}$, respectively. In the experimental prototype, the signal (3.30) is generated by a `TTI-TG5011` function generator, and then fed into the $\mathscr{M}$–ADC and a 4-channel `DSO-X 3024A` oscilloscope that simultaneously samples the input and the output of the $\mathscr{M}$–ADC to produce the ground-truth and the modulo samples. The sampling and reconstruction pipeline follows Fig. 3.7. For validation purposes, standard curve fitting techniques are used to estimate the parameters of (3.30).

Exp. 1: Reconstruction from Non-ideal Modulo Samples

To show demodulation and reconstruction using Algorithm 4, a signal with a period of $\tau = 299\ \mathrm{ms}$ that obeys (3.30) with the parameters $A_{\mathsf{M}} = 3.72, \Omega_{\mathsf{M}} = 43.98\ \mathrm{rad/s}, \theta_{\mathsf{M}} = 2.64, \omega_0 = 628.31 \times 10^3\ \mathrm{rad/s}$, and $\theta_{\mathsf{C}} = -0.93 \times 10^{-2}\ \mathrm{rad}$ is generated. The signal was fed into the $\mathscr{M}$–ADC with a threshold $\lambda \approx 2.01 \pm 3/20$, where $\pm 3/20$ is a manually adjustable design parameter, and then sampled at period $T_{\mathsf{S}} = 10\ \mathrm{ms}$. The produced modulo samples $y[k]$ have $Q_{\mathsf{U}}^x = 3$ and $M = 4$. As (3.30) is an AM signal, we validate that $\Omega_{\mathsf{S}} = 2\pi/T_{\mathsf{S}} = 200\pi\ \mathrm{rad/s}$ satisfies (3.17) with $M_{\mathsf{AM}} = 1$ and also satisfies (3.29) since $\Omega_{\mathsf{B}} = 28\pi \leq 200\pi \leq 293\pi$. The conditions of Corollary 2 are satisfied so we can use Algorithm 4 with input $y[k]$, to produce the recovered samples $\widetilde{x}^{\mathsf{FP}}[k]$. The error compared to the sequence $x[k] = x(kT_{\mathsf{S}})$ is $\mathcal{E}\left(x, \widetilde{x}^{\mathsf{FP}}\right) = 7.1 \times 10^{-3}$, which verifies that $y_{\mathsf{BP}}[k] \approx y[k]$ when undersampled. We then use interpolation with $\mathrm{sinc}(\Omega_{\mathsf{S}} t)$ to get $\widetilde{x}^{\mathsf{FP}}(t)$, and recover $\widetilde{x}_{\mathsf{BP}}(t) = \widetilde{x}^{\mathsf{FP}}(t) \frac{\sin(\omega_0 t + \theta_{\mathsf{C}})}{\sin \theta_{\mathsf{C}}}$. The corresponding signals are shown in Fig. 3.9.

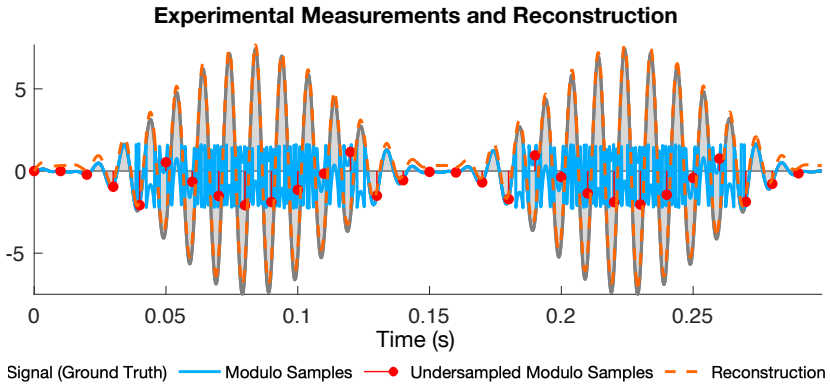


Figure 3.9: Reconstruction from experimental data using $\mathscr{M}$-ADC. The experimental parameters are in Table 3.1 (Exp. 1).

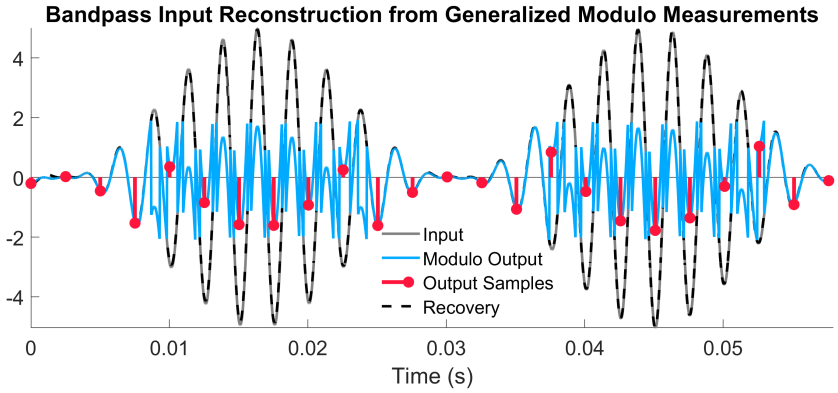


Figure 3.10: Reconstruction from experimental data using the generalized $\mathscr{M}$-ADC. The experimental parameters are in Table 3.1 (Exp. 2).

Exp. 2: Reconstruction From Generalized Modulo Nonlinearity

The input is generated using (3.30) with $\Omega_{\mathsf{M}} = 216\ \mathrm{rad/s}, \omega_0 = 2.5 \times 10^3\ \mathrm{rad/s}, \theta_{\mathsf{M}} = \theta_{\mathsf{C}} = -1.57 \times 10^{-2}\ \mathrm{rad}$, and $A_{\mathsf{M}} = 2.47$. The generalized modulo nonlinearity parameters are $\lambda = 1.93, h = 0.88$, leading to a ratio $\rho = 2.6$ between the input amplitude and modulo threshold. The input is bandpass, satisfying $\{\omega_{\mathsf{L}}, \omega_{\mathsf{U}}\} = \{2.29, 2.73\} \times 10^3$. The input and output of the modulo were sampled with period $T_{\mathsf{S}} = 2.5 \times 10^{-3}$, which is

more than double the Nyquist sampling period of $T_{\mathsf{NS}} = 1.2\,\mathrm{ms}$. This resulted in $K = 24$ samples. The input $x_{\mathsf{BP}}(t)$, modulo output $y(t)$ and output samples $y[k] = y(t)|_{t=kT_{\mathsf{S}}}$ are depicted in Fig. 3.10. The samples of the baseband signal $x(t)|_{t=kT_{\mathsf{S}}}$ were subsequently recovered using Algorithm 3 with threshold λ_h. The signal $x(t)$ is reconstructed via interpolation with $\mathrm{sinc}(\Omega t)$, where $\Omega = \frac{\pi}{T_{\mathsf{S}}}$. The input $x_{\mathsf{BP}}(t)$, recovered as $\widetilde{x}_{\mathsf{BP}}(t) = \widetilde{x}(t)\frac{\sin(\omega_0 t+\theta_{\mathsf{C}})}{\sin\theta_{\mathsf{C}}}$, is depicted in Fig. 3.10. The error between the recovered input and ground truth is $\mathcal{E}(x_{\mathsf{BP}}, \widetilde{x}_{\mathsf{BP}}) = 4.26 \times 10^{-4}$.

3.5 Conclusion

In this chapter, the Unlimited Sensing Framework was leveraged for high dynamic range bandpass sampling. The proposed computational sensing-based solution demonstrates how the distinct advantages of modulo folding architectures can be exploited in this context.

The first insight is that the structure of bandpass input signals can be exploited to establish a unique mapping between bandpass signals and their modulo samples, even at sub-Nyquist rates. Building on that, sampling conditions that guarantee signal recovery are derived. The three folding architectures: ideal modulo, non-ideal modulo, and generalised modulo are examined to address practical considerations of modulo ADCs. Practical recovery algorithms that achieve successful reconstruction at the specified rates, in both the time and frequency domains, were derived as well. The numerical experiments validated the underlying theoretical findings. Taking a step closer to practice, hardware experiments further demonstrated the advantages of the proposed approach.

Overall, this chapter highlights the potential of modulo folding architectures for undersampling-based acquisition. While directly relevant to bandpass signals, the results also lay the ground-

work for broader sampling architectures, such as multi-channel systems [73] and Sigma–Delta ADCs [92], as well as more general signal models, in particular multiband signals.

4

Unlimited Sensing of Multiband Signals

Motivation

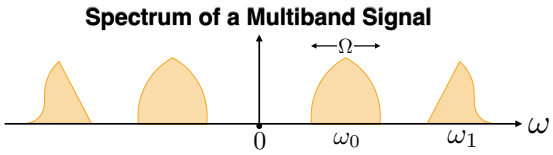


Figure 4.1: The spectrum of a multiband signal.

Multiband signals are characterised by spectra consisting of multiple disjoint frequency bands, as illustrated in Fig. 4.1. They arise across a wide range of technologies, including 5G, Wi-Fi, cognitive radio, radar, sonar, and hyperspectral imaging, where information from several spectral bands is exploited [33, 34, 35, 36, 37, 38, 39].

When sampling multiband signals, a direct application of the Shannon sampling theorem treats the signal as bandlimited to its total spectral span. This is often impractical: the required sampling rate is set by the overall bandwidth rather than the actually occupied subbands, yielding prohibitively high demands on analog-to-digital converters (ADCs). Mathematically, this excess reflects the penalty for ignoring the spectral gaps inherent in the Fourier structure of multiband signals. Over the past decades, *sub-Nyquist sampling* strategies that exploit these gaps have been developed in both classical and modern works [71, 97, 43, 41, 42] and are summarised in Chapter 2.

Looking ahead, multiband signals are expected to play a central role in emerging applications:

- **6G communication**, spanning RF, mmWave, visible-light, and terahertz bands, with dense spectrum occupancy and heightened interference—particularly in MIMO ultra-wideband systems [98].

- **LiDAR- and radar-based autonomous systems**, where robust operation under adverse

conditions is critical for safety.

- **Extended Reality (XR)**, where multiband protocols are essential to meeting stringent latency, throughput, and reliability requirements [99].

Common to the above is the demand for both high dynamic range (HDR) and high digital resolution (HDRes), which adds a further layer of complexity to sampling. ADC quantization introduces a fundamental bottleneck: under a fixed bit budget [46], there is an inherent trade-off between HDR and HDRes. Expanding the dynamic range prevents clipping of strong signals but reduces resolution for weak ones, whereas increasing resolution improves sensitivity to weak components at the risk of saturating strong ones. This trade-off, discussed in Sections 2.1.1 and 2.1.2, is particularly acute in multiband scenarios for two reasons:

1. Coexistence of strong and weak components leads to the near–far problem [44, 45]. Conventional solutions such as variable-gain amplifiers [17] struggle to accommodate both simultaneously [18].

2. Sub-Nyquist methods typically demand high digital resolution. Low sampling rates introduce noise folding, while insufficient bit depth severely compromises algorithmic recovery.

These considerations underscore the need for architectures that mitigate quantization limitations. In this regard, the Unlimited Sensing Framework (USF) offers a distinct advantage: for a fixed bit budget, it increases the effective quantization resolution [24], thereby reducing reliance on excessive bit depth. This property makes USF-enabled sub-Nyquist schemes especially promising for practical acquisition of multiband signals [78].

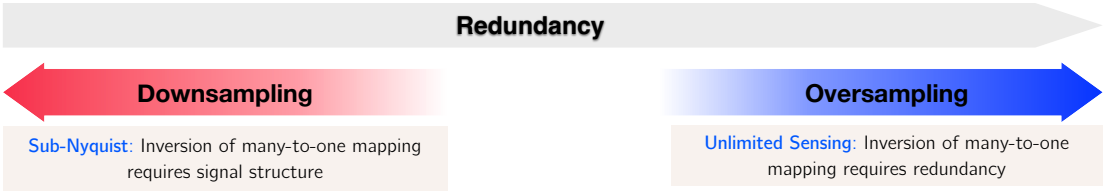


Figure 4.2: Downsampling vs. oversampling through the lens of redundancy. Sub-Nyquist recovery inverts a many-to-one mapping of frequencies by exploiting signal structure. In contrast, the Unlimited Sensing Framework inverts a many-to-one mapping of amplitudes by exploiting measurement redundancy (typically via oversampling).

Unlimited Sensing of Multiband Signals. The challenge in sub-Nyquist USF for multiband signals arises from the conflicting requirements visualised in Fig. 4.2: while undersampling is key to leveraging the multiband structure, redundancy, and in particular, oversampling, is crucial for the inversion of the many-to-one modulo mapping in the USF.

In Chapter 3, we showed that despite their non-bandlimited nature, bandpass signals can be effectively demodulated and acquired both theoretically and in practice using the $\mathscr{M}$–ADC. This, together with insights regarding complex exponentials [78], serves as a first step towards USF-based multiband sampling. Yet, the extension from bandpass signals is not immediate.

Here, we derive a new multiband acquisition strategy within the USF that enables stable recovery under HDR, HDRes and sub-Nyquist constraints. By exploiting structural properties of multiband signals and tailoring the acquisition and recovery processes, we overcome the limitations imposed by aliasing and modulo non-linearities.

Contributions. This chapter formulates and addresses the problem of HDR sampling and recovery of multiband signals with modulo non-linearities at sub-Nyquist sampling rates. The main contributions are:

1) Recovery guarantees. We derive conditions for exact recovery of multiband signals from folded (modulo) samples by leveraging effective bandwidth, tightening the existing USF bandpass sampling result. We further establish below-Nyquist recovery guarantees for a multiphase periodic-nonuniform USF pipeline with known band locations

2) Algorithms. We present a compact single-channel modulo-unfolding architecture that is backwards-compatible with prior multiband frameworks and an integrated USF-based recovery workflow across single- and multi-channel settings.

3) Numerical simulations and hardware experiments. We validate the theory and methods in a single-channel setting, achieving up to $13\times$ dynamic-range improvement with 7-bit measurements. Grounded in the multiphase theoretical framework, collaborators' experiments validate robustness under low-bit quantization and reliability in challenging real-world scenarios.

Signal Model. The multiband signal model is (2.2),

$$x(t) = \sum_{p=0}^{P-1} \varphi_p(t) e^{\jmath \omega_p t}, \quad \operatorname{supp}(\widehat{\varphi}_p) \in \mathcal{D}_{2\Omega_{\mathsf{B}}},$$

where x is the sum of P baseband signals $\{\varphi_p\}_{p=0}^{P-1}$ of bandwidth $2\Omega_{\mathsf{B}}$, with respective modulation frequencies $\Omega_{\mathsf{C}} = \{\omega_p\}_{p=0}^{P-1}$.

To reduce hardware complexity and mitigate challenges related to calibration and synchronisation in multi-channel systems, we first adopt a single-channel design well-suited for compact, resource-constrained systems. The proposed architecture is backwards compatible with previous frameworks, such as hardware-demodulated radar systems, single-channel multiband sampling [65, 66], and multi-channel periodic nonuniform sampling methods [41, 97].

Problem Formulation. Given a multiband input signal x, the acquisition pipeline is described in Chapter 2.3.1 and Fig. 2.9, where the $\mathscr{M}$–ADC hardware yields samples $y[k] = \mathscr{M}_\lambda(x(t))|_{t=kT_S}$, $k \in \mathbb{Z}$. The corresponding inverse problem amounts to:

$$\text{given } y[k] = \mathscr{M}_\lambda(x(kT_S)), \text{ recover the discrete samples } x[k]. \tag{4.1}$$

Solution Approach. Our recovery leverages the separation of modulo samples into their *smooth* and *non-smooth* components based on the modulo decomposition property in [48] (see also Theorem 2.4 in Chapter 2 of this work) , which gives

$$y[k] = x[k] - r[k], \quad r[k] \in 2\lambda\mathbb{Z}, \tag{4.2}$$

where x and r denote the multiband and residual parts, respectively.

Though smoothness can be measured via a digital derivative filter[1] $\Delta = \begin{bmatrix} -1 & 1 \end{bmatrix}$, this would be non-ideal for modulated signals. Therefore, we redefine the filter to accommodate

[1] The filter Δ is used in the US-Alg unfolding method presented in [48] and in (Algorithm 1), to shrink the amplitudes of Ω-bandlimited signals for sufficiently small T_S.

local carrier frequencies $\{\omega_0\}_{p=0}^{P-1}$, which achieves more precise shrinkage. To exemplify this, consider $P = 1$ in (2.2) which results in bandpass signal, $x(t) = \varphi_0(t)e^{-\jmath\omega_0 t}$. Using $\psi = \begin{bmatrix} -1 & e^{\jmath\omega_0 T_\mathsf{S}} \end{bmatrix}$ as an adaptation of Δ, The N-th order filter $\psi^N \stackrel{\text{def}}{=} \psi * \psi^{N-1}$ is related to $\Delta^N \stackrel{\text{def}}{=} \Delta * \Delta^{N-1}$ via,

$$\psi^N[k] = \Delta^N[k]\, e^{-\jmath\omega_0 k T_\mathsf{S}}, \quad k = [0, 1, \cdots, N+1]. \tag{4.3}$$

Then,

$$(\psi^N * x)[k] = e^{-\jmath\omega_0 k T_\mathsf{S}} (\Delta^N * \varphi_0)[k]. \tag{4.4}$$

The advantage of defining the filter ψ is that the upper bound $||\psi^N * x||_\infty$ is independent of ω_0. According to [48], $||\Delta^N \varphi_0||_\infty \leq (T_\mathsf{S}\Omega_\mathsf{B} e)^N ||\varphi_0||_\infty$ for $T_\mathsf{S} \leq 1/(2\Omega_\mathsf{B} e)$. Hence, we can find N such that $||\psi^N * x||_\infty$ is arbitrarily small. The shrinkage of $||\psi^N * x||_\infty$ for increasing N is exploited to isolate the samples $r[k]$ in (4.2). Despite the conceptual similarity to US-Alg in [48], the same technique cannot be applied because $\psi^N[k] \notin \mathbb{Z}$; a new recovery strategy is needed to handle the non-integer nature of ψ. In Section 4.2.1, we formalise the filter ψ for $P > 1$. Then, in Section 4.2.2, we introduce a recovery algorithm in the domain defined by ψ^N.

4.2.1 The Proposed Filter

Before generalising the solution approach and presenting the recovery algorithm, we formulate the properties of the filter Ψ, defined for a set of modulation frequencies Ω_C. We also formalise its property to arbitrarily shrink the amplitudes of a multiband signal x for a choice of T_S.

Lemma 1. *Let x be defined in* (2.2) *with frequencies $\Omega_{\mathsf{C}} \stackrel{\text{def}}{=} \{\omega_p\}_{p=0}^{P-1}$, $\#\Omega_{\mathsf{C}} = P$. Let $x[k] = x(t)\big|_{t=kT_{\mathsf{S}}}$. Define*

$$\Psi_{\Omega_{\mathsf{C}}} \stackrel{\text{def}}{=} \psi_0 * \psi_1 * \cdots \psi_{P-1}, \quad \psi_p \stackrel{\text{def}}{=} \begin{bmatrix} -1 & e^{\jmath\omega_p T_{\mathsf{S}}} \end{bmatrix}, \tag{4.5}$$

and $\Psi_{\Omega_{\mathsf{C}}}^N \stackrel{\text{def}}{=} \Psi_{\Omega_{\mathsf{C}}} * \Psi_{\Omega_{\mathsf{C}}}^{N-1}$. Let $||\varphi||_\infty \stackrel{\text{def}}{=} \max_p ||\varphi_p||_\infty$. Then,

$$||\Psi_{\Omega_{\mathsf{C}}}^N * x||_\infty \leq P(T_{\mathsf{S}} 2^{P-1} \Omega_{\mathsf{B}} e)^N ||\varphi||_\infty. \tag{4.6}$$

Proof. Let $\widetilde{\varphi}_p[k] \stackrel{\text{def}}{=} \varphi_p[k]\, e^{-\jmath\omega_p k T_{\mathsf{S}}}$ and $\Omega_{\mathsf{C}}^{[p]} \stackrel{\text{def}}{=} \Omega_{\mathsf{C}} \setminus \{\omega_p\}$. We will use the identity

$$\left(\Psi_{\Omega_{\mathsf{C}}}^N * \widetilde{\varphi}_p\right)[k] = \left(\Psi_{\Omega_{\mathsf{C}}^{[p]}}^N * \left[\left(\Delta^N * \varphi_p\right)[m]\, e^{\jmath\omega_p(m) T_{\mathsf{S}}}\right]\right)[k], \tag{4.7}$$

which is proved by induction in Appendix A. Taking magnitudes in (4.7), we obtain:

$$\left\|\left(\Psi_{\Omega_{\mathsf{C}}}^N * \widetilde{\varphi}_p\right)\right\|_\infty \leq \left\|\Psi_{\Omega_{\mathsf{C}}^{[p]}}^N\right\|_1 ||\Delta^N * \varphi_p||_\infty. \tag{4.8}$$

The filter coefficients are $\Psi_{\Omega_{\mathsf{C}}}[k] = (-1)^k a_{\Omega_{\mathsf{C}}}^k$, where we define $a_{\Omega_{\mathsf{C}}}^k$ as the degree k elementary symmetric polynomial[2] in P variables $\{e^{\jmath\omega_p t}\}_{\omega_p \in \Omega_{\mathsf{C}}}$. For the N^{th} order filter,

$$\Psi_{\Omega_{\mathsf{C}}}^N[k] = (-1)^k \sum\nolimits_{\mathbf{v} \in \mathcal{V}(N,k)} \prod\nolimits_{i=0}^{N-1} a_{\Omega_{\mathsf{C}}}^{[\mathbf{v}]_i}, \tag{4.9}$$

where the set $\mathcal{V}(N,k) = \left\{\mathbf{v} \in \mathbb{N}^N \mid \sum_{i=1}^N [\mathbf{v}]_i = k\right\}$ consists of all length-N vectors of

[2] For a set of variables $\zeta = \{z_n\}_{n=0}^{N-1}$, the elementary symmetric polynomial of degree k is $a_\zeta^k = \sum_{S \subseteq \mathbb{I}_N, \#S=k} z_{i_1} z_{i_2} \cdots z_{i_k}$.

non-negative integers whose elements sum to k. Therefore, we have

$$\left\|\Psi^N_{\Omega_{\mathsf{C}}^{[p]}}\right\|_1 \leq \sum_{n=0}^{N(P-1)} \sum_{\mathbf{v}\in\mathcal{V}(N,k)} \prod_{i=0}^{N-1} \left|a^{[\mathbf{v}]_i}_{\Omega_{\mathsf{C}}^{[p]}}\right|.$$

Using Vandermonde's identity $\sum_{k=0}^{r}\binom{m}{k}\binom{n}{r-k} = \binom{m+n}{r}$ and $\left|a^{[\mathbf{v}]_i}_{\Omega_{\mathsf{C}}^{[p]}}\right| = \binom{\Omega_{\mathsf{C}}^{[p]}}{[\mathbf{v}]_i}$, where $\binom{m}{k}$ denotes the binomial coefficient,

$$\left\|\Psi^N_{\Omega_{\mathsf{C}}^{[p]}}\right\|_1 \leq \sum_{n=0}^{N(P-1)} \binom{N\#\Omega_{\mathsf{C}}^{[p]}}{n} = 2^{N(P-1)}. \tag{4.10}$$

Plugging (4.10) and the bound $||\Delta^N * \varphi_p||_\infty$ from [48] in (4.8),

$$\left\|\left(\Psi^N_{\Omega_{\mathsf{C}}} * \widetilde{\varphi}_p\right)\right\|_\infty \leq 2^{N(P-1)}(T_{\mathsf{S}}\Omega_{\mathsf{B}}e)^N ||\varphi_p||_\infty.$$

Finally, from the linearity of convolution and summation over P terms, we obtain the final bound $||\Psi^N_{\Omega_{\mathsf{C}}} * x||_\infty \leq P\left\|\Psi^N_{\Omega_{\mathsf{C}}} * \widetilde{\varphi}_p\right\|_\infty$. ■

From Lemma 3, choosing $T_{\mathsf{S}} \leq \frac{1}{2^P\Omega_{\mathsf{B}}e}$ ensures that the amplitudes of x shrink as N increases. It is valuable to investigate the result of Lemma 1 for particular signal classes.

Bandlimited case ($P = 1$). The condition $T_{\mathsf{S}} < 1/(2\Omega_{\mathsf{B}}e)$ matches [48], while the applicability is extended to one-sided bandpass signals, as ω_0 does not affect the sampling rate.

Bandpass Case ($P = 2$). For real-valued bandpass signals, we have $T_{\mathsf{S}} \leq 1/(4\Omega_{\mathsf{B}}e)$. As T_{S} is independent of ω_0, a new USF bandpass sampling condition can be deduced. We add the

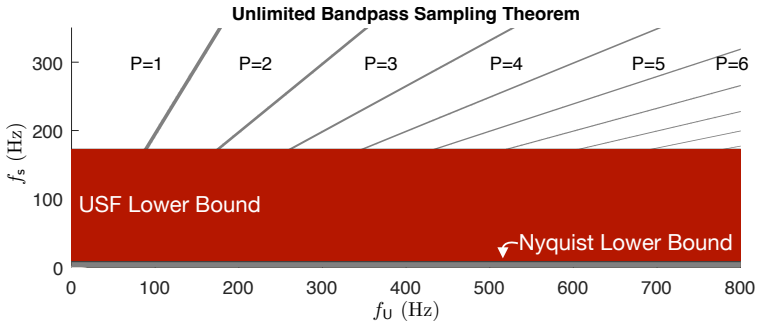


Figure 4.3: Achievable (white) and unachievable (red) sampling rates under the Unlimited Sensing Framework as a function of the maximum frequency f_{U}. They differ from the conventional result [72] only by a lower bound, while allowing high dynamic range recovery.

USF condition to the bandpass sampling formula in [72]:

$$\frac{\pi(P-1)}{\omega_0 - \Omega_{\mathsf{B}}} \leq T_{\mathsf{S}} \leq \min\left\{\frac{\pi P}{\omega_0 + \Omega_{\mathsf{B}}}, \frac{1}{4\Omega_{\mathsf{B}} e}\right\}, \quad P \in \mathbb{Z}. \tag{4.11}$$

Shown in Fig. 4.3, the result is less restrictive compared to [94].

Multiband Case ($P > 2$). The condition $T_{\mathsf{S}} < 1/(2^P \Omega_{\mathsf{B}} e)$ implies an exponential decrease in T_{S} with P, but this is still often lower than T_{NS} in practical cases, as it depends on the total bandwidth $\{\Omega_{\mathsf{B}}, P\}$, rather than modulation frequencies. Notably, it does not impose constraints on inter-band spacing; therefore, it can be treated as an added constraint in algorithmic approaches such as [65, 66] used in uniform multiband sampling, without requiring reformulation or guard bands.

4.2.2 Recovery Algorithm

Convolving both sides of (4.18) with the complex-valued filter[3] $\Psi^N \in \mathbb{C}^{P(N+1)}$ defined in (4.5) gives

$$\left(\Psi^N * y\right)[k] = \left(\Psi^N * x\right)[k] - \left(\Psi^N * r\right)[k]. \tag{4.12}$$

Lemma 1 provides an upper bound on $||\Psi^N * x||_\infty$ under the specified conditions. Then, the following unfolding algorithm can recover $x[k]$ from modulo samples $y[k]$.

Theorem 4.1 [Multiband Recovery from Uniform Samples]

Let x be defined in (2.2) *with frequencies $\Omega_{\mathsf{C}} \overset{\text{def}}{=} \{\omega_p\}_{p=0}^{P-1}$, $\#\Omega_{\mathsf{C}} = P$. Moreover, let $y[k]$, $k \in \mathbb{Z}$ denote its modulo samples at period T_{S} and $k_0 \in \mathbb{Z}$ denote the index of the first modulo fold. Let $\beta \in \{z \in 2\lambda\mathbb{Z} : z \geq ||\varphi||_\infty\}$. If $k_0 > NP + 1$, and*

$$T_{\mathsf{S}} < 1/\left(2^{P-1}\Omega_{\mathsf{B}} e\right), \quad N \geq \left\lceil \frac{\log(\lambda) - \log(P\beta)}{\log\left(T_{\mathsf{S}} P 2^{P-1}\Omega_{\mathsf{B}} e\right)} \right\rceil, \tag{4.13}$$

then the samples $x[k] = x|_{t=kT_{\mathsf{S}}}$ can be recovered from $y[k]$.

Proof. We show a constructive proof for reconstructing $x[k], \forall k \in \mathbb{Z}$, considering: 1. $k < k_0$ 2. $k = k_0$ 3. $k > k_0$.

1) $\mathbf{k < k_0}$**:** The modulo signal has no folds so $x[k] = y[k]$.

2) $\mathbf{k = k_0}$**:** Compute the filter Ψ using (4.5) with Ω_{C}[4]. Apply it to get (4.12) and then apply

[3] To relax the notation, the subscript Ω_{C} is omitted.

[4] For $T_{\mathsf{S}} > T_{\mathsf{NS}}$ (undersampling), then $\Omega_{\mathsf{C}} = \{\omega \bmod \Omega_{\mathsf{S}} \ : \ \omega \in \Omega_{\mathsf{C}}\}$.

$\mathscr{M}_\lambda(\cdot)$ on both sides to get

$$\mathscr{M}_\lambda(\Psi^N * y) = \mathscr{M}_\lambda(\mathscr{M}_\lambda(\left(\Psi^N * x\right)) - \mathscr{M}_\lambda(\Psi^N * r)).$$

From Lemma 3, T_{S} and N satisfying (4.13) yield,

$$||\Psi^N * x||_\infty \leq P(T_{\mathsf{S}} 2^{(P-1)} \Omega_{\mathsf{B}} e)^N ||\varphi||_\infty \leq \lambda. \tag{4.14}$$

For the *residual component*, note that $r\left[k\right] = 0$ for all $k \in [k_0 - 2NP, k_0)$. Define $\widetilde{k} = k_0 - NP$, then:

$$\begin{aligned}\left(\Psi^N * r\right)\left[\widetilde{k}\right] &= \sum\nolimits_{|p| \leq \left\lfloor \frac{NP}{2} \right\rfloor} r\left[\widetilde{k} - p\right] \Psi^N\left[p\right] \\ &= r\left[k_0\right] \Psi^N\left[-NP\right]. \end{aligned} \tag{4.15}$$

Since Ψ^N is known, we can normalize it such that $\Psi^N\left[-NP\right] = 1$. Because $r\left[k\right] \in 2\lambda\mathbb{Z}$ we have $\mathscr{M}_\lambda(\left(\Psi^N * r\right)\left[\widetilde{k}\right]) = \mathscr{M}_\lambda(r\left[k_0\right]) = 0$. Combining with (4.14), we get $\mathscr{M}_\lambda(\left(\Psi^N * y\right)\left[\widetilde{k}\right]) = \left(\Psi^N * x\right)\left[\widetilde{k}\right]$. Hence,

$$r\left[k_0\right] = \mathscr{M}_\lambda(\left(\Psi^N * y\right)\left[\widetilde{k}\right]) - \left(\Psi^N * y\right)\left[\widetilde{k}\right], \tag{4.16}$$

and the recovered sample is $x\left[k_0\right] = y\left[k_0\right] + r\left[k_0\right]$.

3) $\mathbf{k > k_0}$**:** Given $r\left[k_0\right]$, define the corrected signal $y^{(k_0)} \stackrel{\text{def}}{=} (y + r\left[k_0\right]\delta\left[m - k_0\right])$. The first fold in $y^{(k_0)}$ occurs at $k > k_0$. Thus, applying step 2) recursively to $y^{(k_0)}$, with $\widetilde{k} = k_0 - NP + 1$, yields $r\left[k_0 + 1\right]$. Repeating steps 2) and 3) results in $x\left[k\right]$. ■

Algorithm 5: Unlimited Sampling of Multiband Signals (Single-Channel)

Input: $y, \Omega_{\mathsf{C}}, \lambda, N$ (computed in (4.13)).
Result: x, unfolded amplitudes of a multiband signal.

1) Compute the FIR filter Ψ^N of length $NP+1$ using (4.5).
2) Normalize $\Psi^N[k] \leftarrow \Psi^N[k] / (\Psi^N\left[-\left\lfloor \frac{NP}{2} \right\rfloor\right])$.
3) Initialize $y_\Psi^{(0)} \leftarrow \Psi^N * y$.
4) For $k \leq 2NP$, set $x[k] = y[k]$, $y_\Psi^{(k+1)} = y_\Psi^{(k)}$.
5) For $k > 2NP$, perform:
   $x[k] = y[k] + \mathscr{M}_\lambda(\left(y_\Psi^{(k)}\right)[k-NP]) - y_\Psi[k-NP]$.
   $y_\Psi^{(k+1)} \leftarrow y_\Psi^{(k)} + (x[k] - y[k])\left(\Psi^N * \delta[m-k]\right)$.

Starting from the modulo samples of a multiband signal x, Algorithm 3 recovers the undersampled sequence[5] x. If T_{S} is also an "alias-free rate" [71], recovery of x is possible. Starting with the modulo samples of a multiband signal $x(t)$, Algorithm 5 provides the undersampled sequence x. In the cases where T_{S} is also an alias-free rate of the spectral support, or for systems based on multiple uniform samplers [41, 10], recovery of $x(t)$ is possible.

4.2.3 Experimental Validation

Performance. We numerically validate our method over 621 random realizations with $P = 6$ bands of width $f_{\mathsf{B}} = 400$ Hz, generated per [42]. The modulation frequencies randomly span from f_{B} to $\frac{12.5}{T_{\mathsf{S}}} - f_{\mathsf{B}}$. Signals are sampled at $T_{\mathsf{S}} = 2.5 \times 10^{-5}$ s, satisfying (4.13), with a modulo threshold $\lambda = 0.01 = \frac{\|x\|_\infty}{100}$. All recoveries achieve machine-precision MSE. Fig. 4.4 illustrates the diversity of the spectrum that can be handled.

[5] The condition on k_0 is discussed in [77].

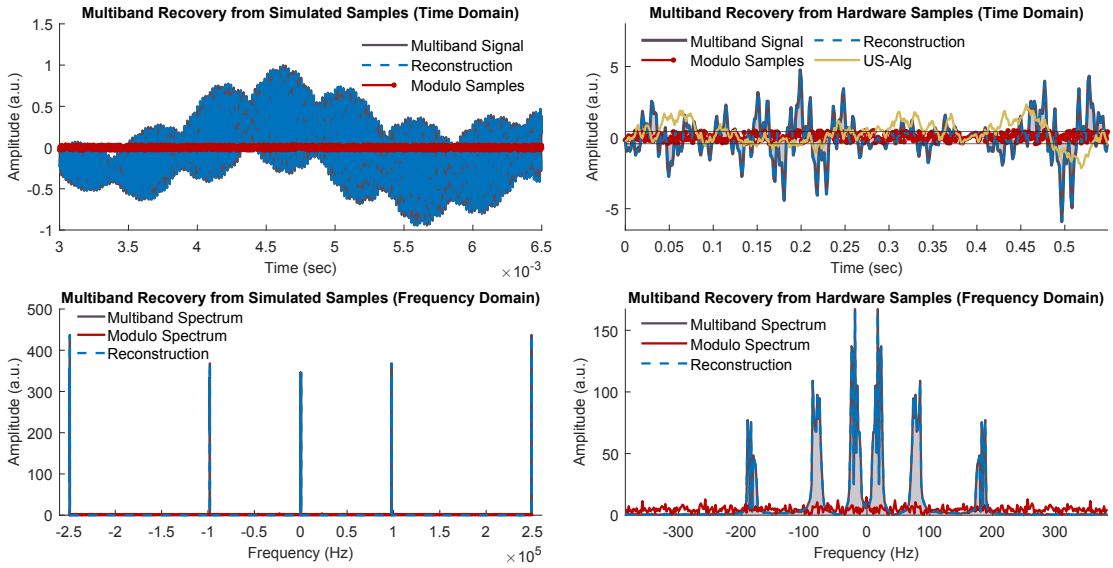


Figure 4.4: Reconstruction of a multiband signal. Left: numerical experiment. The sampling rate approaches the Nyquist rate of the multiband signal. Right: reconstruction from 7-bit quantized samples collected via hardware. The dynamic range improvement is $13.7\times$, and the reconstruction MSE is 2.7×10^{-3}. As shown (yellow ink), recovery using US-Alg for the given sampling rate T_{S} fails.

Stability. To empirically test the noise sensitivity of the proposed algorithm, we fix $f_{\mathsf{C}} = \{\pm 9.7, \pm 15.5, \pm 23.5\}$ kHz with $f_{\mathsf{s}} = 20$ kHz and set the dynamic range gain to $\approx 6.6\times$. We add gradually increasing white Gaussian noise η to the modulo samples from level 50 to 5 dB. The filter order is chosen such that $||\varphi * (x + \eta)||_\infty \leq \lambda$ for each noise level. The average MSE over 200 experiments is plotted versus SNR in Fig. 4.5, showing low MSE up to a noise level of 15 dB.

Hardware Experiment. We validate our algorithm via hardware experiments. The multiband signal x is parametrized by $f_{\mathsf{C}} = \{25.64, 79.77, 182.34\}$ and $f_{\mathsf{B}} = 22.04$ Hz, and is digitised with 7-bit resolution, as in [100]. The maximum amplitude is $||x||_\infty = 5.91 = 13.7\lambda$ with modulo threshold $\lambda = 0.43$. The choice of sampling period $T_{\mathsf{S}} = 1.3\times10^{-3}$ s $\approx 0.5T_{\mathsf{NS}}$ compensates for quantization noise and distortion. Reconstruction results are shown

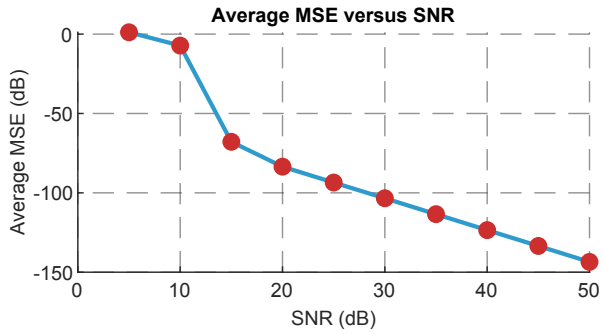


Figure 4.5: Reconstruction performance under additive white Gaussian noise. The proposed algorithm maintains stable recovery down to 20 dB.

in Fig. 4.4, achieving an MSE of 2.7×10^{-3} while US-Alg [48] fails under the same setting.

4.3 Multiphase Acquisition and Recovery

The term multiphase refers to a periodic nonuniform sampling pattern obtained by sampling the waveform at several known temporal phases. In practice, this work implements this pattern using multiple time-delayed acquisition branches; These branches should not be interpreted as independent signal channels.

The deployment of the single-channel method presented in Chapter 4.2 would either require additional demodulation hardware [69, 9], or satisfying a set of constraints that can be challenging to meet at sub-Nyquist sampling rates [65].

Another route to introduce redundancy at sub-Nyquist rates (Fig. 4.2) is to sample the same modulo-folded waveform at several known temporal phases. This leads to a multiphase sampling architecture: each phase is sampled uniformly with period T_S, while the collection of phases forms a denser nonuniform sampling pattern over one period. The redundancy required for modulo unfolding is therefore obtained across the phase/delay index. This design is closely related to the classical multi-coset architecture for multiband sampling, grounded

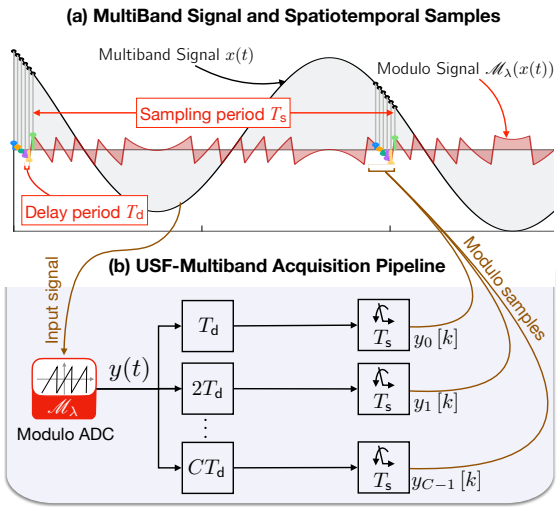


Figure 4.6: Multiphase Unlimited Sensing Framework sampling architecture. The high-dynamic-range input signal $x(t)$ is being folded in the analog-domain, yielding the low-dynamic-range signal $\mathscr{M}_\lambda(x(t))$ as shown in (a). Subsequently, the folded signal $\mathscr{M}_\lambda(x(t))$ is sampled pointwise at period T_S through multiple channels with time-delays T_d.

in Landau's density criterion [7, 101] and periodic nonuniform sampling (see Chapter 2.2.3), and it retains the simplicity and efficiency reported in [9].

Forward Model. We consider the multiband signal model (2.2), where $x(t) \in \mathbb{R}$. To describe multiphase modulo sampling, we introduce the spatiotemporal sampling model

$$y[c,k] = \mathscr{M}_\lambda(x(t+s))|_{t=kT_\mathsf{S}, s=cT_\mathsf{d}}, \quad k \in \mathbb{Z},\ c \in \mathbb{I}_C, \tag{4.17}$$

where $T_\mathsf{S}, T_\mathsf{d} \in \mathbb{R}^+$ and we assume $T_\mathsf{S} \leq \frac{\pi}{2\Omega_\mathsf{B}}$. Here, c is the phase index, which in practical implementation is referred to as the channel. Vectorization of the two-dimensional sequence (4.17) yields a periodic, nonuniform sampling pattern, so the model is compatible with techniques such as multi-coset sampling and can be implemented as a time-delayed multi-channel architecture. This is illustrated in Fig. 4.6.

Solution Approach. The parameters $\{T_{\mathsf{S}}, T_{\mathsf{d}}\}$ in (4.17) control the sampling density along the temporal and spatial indices k and c, respectively. Considering a sub-Nyquist setup where $T_{\mathsf{S}} > T_{\mathsf{NS}}$ [40], the condition (2.19) is not satisfied along the index k[6]. Therefore, applying a finite differences operator along the temporal dimension of x in the spirit of US-Alg would not result in amplitude shrinkage. On the other hand, the parameter T_{d} in (4.17) can be set to yield amplitude shrinkage and make the value $||\Delta_{T_{\mathsf{d}}} x||_{\infty}$ arbitrarily small, where $\Delta_{T_{\mathsf{d}}}$ denote the finite difference operator along the spatial dimension, even when T_{S} is relatively large. This idea extends the principle used in [102], which is described in Chapter 5.2.

To see this approach in action, we begin with the modulo decomposition (4.18), followed by the application of the N^{th} order operator $\Delta_{T_{\mathsf{d}}}^{N}$,

$$y\left[c,k\right] = x\left[c,k\right] - r\left[c,k\right] \Rightarrow \Delta_{T_{\mathsf{d}}}^{N} y = \Delta_{T_{\mathsf{d}}}^{N}(x - r). \tag{4.18}$$

For a suitable choice of $\{T_{\mathsf{d}}, N\}$, we have $\mathscr{M}_{\lambda}(\Delta_{T_{\mathsf{d}}}^{N} y) = \Delta_{T_{\mathsf{d}}}^{N} x$. Despite the similarity to the case of bandlimited inputs, our approach recovers x directly from $\Delta_{T_{\mathsf{d}}}^{N} x$. This avoids the ambiguity caused by anti-difference operations used in [48, 23, 26], where x is recovered by inverting $\Delta_{T_{\mathsf{d}}}^{N} r$. The solution steps are detailed below.

Recovery Guarantees

To separate $\Delta_{T_{\mathsf{d}}}^{N} x$ and $\Delta_{T_{\mathsf{d}}}^{N} r$ in (4.18), the following bound will be used.

Lemma 2. *Let* $x(t) = \sum_{p=0}^{P-1} \varphi_p(t) e^{\jmath \omega_p t}$, $\text{supp}\left(\widehat{\varphi}_p\right) \in \mathcal{D}_{2\Omega_{\mathsf{B}}}$, $||\varphi||_{\infty} = \max_p ||\varphi_p||_{\infty}$,

[6] See proof of Lemma 2 in [48] and its following discussion.

$\omega_{\mathsf{U}} \stackrel{\text{def}}{=} \max\{\omega_p\}_{p=0}^{P-1}$. *Moreover, let* $x[k] = x(t)|_{t=kT},\ k \in \mathbb{Z}$, *and* $T \leq \frac{\pi}{\omega_{\mathsf{U}}+\Omega_{\mathsf{B}}}$. *Then,*

$$||\Delta^N x||_\infty \leq P\left(\frac{\omega_{\mathsf{U}}}{\Omega_{\mathsf{B}} e}+1\right)^N (Te\Omega_{\mathsf{B}})^N ||\varphi||_\infty. \tag{4.19}$$

Proof. Define $\widetilde{\varphi}_p[k] = \varphi_p(t)\, e^{\jmath\omega_p t}|_{t=kT_{\mathsf{S}}}$. We prove via induction that $\Delta^N\widetilde{\varphi}_p$ satisfies,

$$\left[\Delta^N\widetilde{\varphi}_p\right]_k = e^{\jmath\omega_p kT_{\mathsf{d}}}\sum_{n=0}^{N} h_N[n]\left[\Delta^n\varphi_p\right]_{k+N-n}, \quad h_N[n] \stackrel{\text{def}}{=} \binom{N}{n}\left(e^{\jmath\omega_p T_{\mathsf{d}}}-1\right)^{N-n}. \tag{4.20}$$

Base $N = 1$

$$\begin{aligned}\left[\Delta\widetilde{\varphi}_p\right]_k &= \left[\varphi_p\right]_{k+1} e^{\jmath\omega_p(k+1)T} - \left[\varphi_p\right]_k e^{\jmath\omega_p kT} = e^{\jmath\omega_p kT}\left(\left(e^{\jmath\omega_p T}-1\right)\left[\varphi_p\right]_{k+1} + \left[\Delta\varphi\right]_k\right)\\ &= e^{\jmath\omega_p kT}\left(h_1[0]\left[\varphi_p\right]_{k+1} + h_1[1]\left[\Delta\varphi_p\right]_k\right).\end{aligned}$$

Assume (4.20) holds for $N-1$. **Prove** for N:

$$\left[\Delta^N\widetilde{\varphi}_p\right]_k = \left[\Delta\left(\Delta^{N-1}\widetilde{\varphi}_p\right)\right]_k = \left[\Delta^{N-1}\widetilde{\varphi}_p\right]_{k+1} - \left[\Delta^{N-1}\widetilde{\varphi}_p\right]_k.$$

Using the induction assumption,

$$\left[\Delta^{N-1}\widetilde{\varphi}_p\right]_{k+1} = e^{\jmath\omega_p T}\sum_{n=0}^{N-1} h_{N-1}[n]\left[\Delta^n\varphi_p\right]_{k+1+N-1-n} e^{\jmath\omega_p kT},$$

and similarly for the term $\left[\Delta^{N-1}\widetilde{\varphi}_p\right]_k$. Combining the terms,

$$\begin{aligned}\left[\Delta^N\widetilde{\varphi}_p\right]_k &= e^{\jmath\omega_p kT}\sum_{n=0}^{N-1} h_{N-1}[n]\left(\left[\Delta^n\varphi_p\right]_{k+N-n} e^{\jmath\omega_p T} - \left[\Delta^n\varphi_p\right]_{k+N-1+n}\right) \qquad (4.21)\\ &= e^{\jmath\omega_p kT}\sum_{n=0}^{N-1} h_{N-1}[n]\left(\left[\Delta^n\varphi_p\right]_{k+N-n} h_1[0] + \left[\Delta^{n+1}\varphi_p\right]_{k+N-n-1} h_1[1]\right).\end{aligned}$$

Splitting the sum and using a change of variables $\widetilde{n} = n+1$,

$$\begin{aligned}\left[\Delta^N\widetilde{\varphi}_p\right]_k &= e^{\jmath\omega_p kT}\left(\sum_{n=0}^{N-1} h_{N-1}[n]h_1[0]\left[\Delta^n\varphi_p\right]_{k+N-n}\right.\\ &\qquad \left.+\sum_{\widetilde{n}=1}^{N} h_{N-1}[\widetilde{n}-1]h_1[1]\left[\Delta^{\widetilde{n}}\varphi_p\right]_{k+N-\widetilde{n}}\right)\\ &= e^{\jmath\omega_p kT}\sum_{\widetilde{n}=0}^{N}\left(h_{N-1}[\widetilde{n}]h_1[0] + h_{N-1}[\widetilde{n}-1]h_1[1]\right)\left[\Delta^{\widetilde{n}}\varphi_p\right]_{k+N-\widetilde{n}},\end{aligned}$$

with the convention $h_{N-1}[-1] = h_{N-1}[N] = 0$. Using the binomial recursion

$$\begin{aligned}h_N[n] &\stackrel{\text{def}}{=} \binom{N}{n}(e^{j\omega_p T}-1)^{N-n} = \left(\binom{N-1}{n} + \binom{N-1}{n-1}\right)(e^{j\omega_p T}-1)^{N-n}\\ &= \binom{N-1}{n}(e^{j\omega_p T}-1)\,(e^{j\omega_p T}-1)^{N-1-n} + \binom{N-1}{m-1}(e^{j\omega_p T}-1)^{N-1-(n-1)}\\ &= h_{N-1}[n]\,(e^{j\omega_p T}-1) + h_{N-1}[n-1] = h_{N-1}[n]\;h_1[0] + h_{N-1}[n-1]\;h_1[1],\end{aligned}$$

we get (4.20) and the induction is complete.

As shown in [48], for bandlimited functions we have $||\Delta^n\varphi_p||_\infty \leq (T\Omega e)^n$. To upper bound (4.20), we use this result along with $\left|\left(e^{\jmath\omega_p T}-1\right)\right| = 2\left|\sin\left(\frac{\omega_p T}{2}\right)\right| \leq \omega_p T$. This

yields:

$$\begin{aligned}
\left|\left[\Delta^N \widetilde{\varphi}_p\right]_k\right| &\leq \sum_{n=0}^{N} |h_N[n]| \left|\left[\Delta^n \varphi_p\right]_{k+N-n}\right| \\
&\leq \sum_{n=0}^{N} \binom{N}{n} \left|\left(e^{\jmath\omega_p T} - 1\right)\right|^{N-n} (T\Omega_{\mathsf{B}} e)^n \left|\left|\varphi_p\right|\right|_\infty \\
&= \sum_{n=0}^{N} \binom{N}{n} (\omega_p T)^{N-n} (T\Omega_{\mathsf{B}} e)^n \left|\left|\varphi_p\right|\right|_\infty \\
&= \left(\omega_p T \left(1 + \tfrac{\Omega_{\mathsf{B}} e}{\omega_p}\right)\right)^N \left|\left|\varphi_p\right|\right|_\infty .
\end{aligned}$$

The final result follows from the triangle inequality

$$\left|\left|\Delta^N x\right|\right|_\infty \leq \sum_{p=0}^{P-1} \left|\left|\Delta^N \widetilde{\varphi}_p\right|\right|_\infty \leq P \max_p \left(\left|\left|\Delta^N \widetilde{\varphi}_p\right|\right|_\infty\right).$$

■

Our result is backwards-compatible with the known USF result for the bandlimited class, as can be verified by setting $P = 1$, and $\omega_0 = 0$, yielding the bound in [20], as expected.

The upper bound in Lemma 2, given by 4.19, depends on the maximum frequency of the multiband signal, ω_{U}. This limitation comes from not fully exploiting the signal's Fourier structure. In Section 4.2, we replace the difference filter Δ with a frequency-aware filter $\Psi_{\Omega_{\mathsf{C}}}$ that leverages this structure, yielding an upper bound that is independent of ω_{U}.

Exact Multiband Recovery via Sub-Nyquist USF. The upper bound in Lemma 2 can be applied along the spatial dimension of our `USF-MC` architecture, with respect to the delay T_{d}.

For $x[c,k]$ in (4.18) we have,

$$||\Delta^N_{T_\mathsf{d}} x||_\infty \leq P\left(\frac{\omega_\mathsf{U}}{\Omega_\mathsf{B} e}+1\right)^N (T_\mathsf{d} e \Omega_\mathsf{B})^N ||\varphi||_\infty. \tag{4.22}$$

Therefore, by choosing sufficiently small T_d we "oversample" x along its spatial dimension, which leads to the LHS of (4.22) being arbitrarily small. The exact recovery of $x\,(t)$ from $y\,[c,k]$ is then achievable under the conditions in the next theorem.

Theorem 4.2 [Exact Multiband Recovery]

Let $x(t) = \sum_{p=0}^{P-1} \varphi_p(t) e^{\jmath\omega_p t}$, *where* $\operatorname{supp}(\widehat{\varphi}_p) \in \mathcal{D}_{2\Omega_\mathsf{B}}$, $||\varphi||_\infty = \max_p ||\varphi_p||_\infty$, $\omega_\mathsf{U} \overset{\text{def}}{=} \max\{\omega_p\}_{p=0}^{P-1}$, *and* $x(t) \in \mathbb{R}$. *Let* $y\,[c,k]\,,\ c \in \mathbb{I}_C,\ k \in \mathbb{Z}$ *be its modulo samples obtained by the model* (4.17) *with* $T_\mathsf{S} = LT_\mathsf{d}$, *where* L *is prime and* $\widehat{x}\,(\omega) = 0$, $\forall|\omega| < \frac{\pi}{T_\mathsf{S}}$. *If,*

$$T_\mathsf{d} < \frac{1}{\omega_\mathsf{U}+\Omega_\mathsf{B} e}, \quad N \geq \left\lceil \frac{\log\lambda - \log P||\varphi||_\infty}{\log T_\mathsf{d}\,(\omega_\mathsf{U}+\Omega_\mathsf{B} e)} \right\rceil, \quad C = P+N, \tag{4.23}$$

Then $x\,(t)$ *can be perfectly recovered.*

Proof. Let $\mathbf{x}_k, \mathbf{y}_k \in \mathbb{R}^C$ be the vectors with elements $[\mathbf{x}_k]_c = x\,[c,k]$, and $[\mathbf{y}_k]_c = y\,[c,k]$, respectively, corresponding to C samples at rate T_d. From (4.18), $\Delta^N \mathbf{y}_k = \Delta^N \mathbf{x}_k - \Delta^N \mathbf{r}_k$, where $\mathbf{r}_k \overset{\text{def}}{=} \mathbf{x}_k - \mathbf{y}_k$. The choice of $T_\mathsf{d} < \frac{1}{\omega_\mathsf{U}+\Omega_\mathsf{B} e}$ guarantees that $T_\mathsf{d}\,(\omega_\mathsf{U}+\Omega_\mathsf{B} e) < 1$. Therefore, the amplitudes of $\mathbf{x}_k$ shrink with the filter order N based on Lemma 2. For N that satisfies (4.23), the upper bound on x leads to

$$||\Delta^N \mathbf{x}_k||_\infty \leq \lambda \;\Rightarrow\; \mathscr{M}_\lambda(\Delta^N \mathbf{y}_k) = \Delta^N \mathbf{x}_k, \tag{4.24}$$

because $\left[\Delta^N \mathbf{r}_k\right]_c \in 2\lambda\mathbb{Z},\ \forall c \in \mathbb{I}_{C-N}$. The principle in (4.24) is then applied for every vector of c samples, indexed by k. Let $\mathbf{X}, \mathbf{Y}$ be the concatenation of vectors $\mathbf{x}_k, \mathbf{y}_k$, respectively:

$$\mathbf{X} \stackrel{\text{def}}{=} \begin{bmatrix} \mathbf{x}_0 & \mathbf{x}_1 & \cdots & \mathbf{x}_k \cdots \end{bmatrix}, \quad \mathbf{Y} \stackrel{\text{def}}{=} \begin{bmatrix} \mathbf{y}_0 & \mathbf{y}_1 & \cdots & \mathbf{y}_k \cdots \end{bmatrix}, \quad k \in \mathbb{Z}. \tag{4.25}$$

By applying finite differences along the columns of $\mathbf{Y}$, followed by the modulo operator, we compose the matrix $\overline{\mathbf{Y}}$

$$\overline{\mathbf{Y}} \stackrel{\text{def}}{=} \begin{bmatrix} \overline{\mathbf{y}}_0 & \overline{\mathbf{y}}_1 & \cdots & \overline{\mathbf{y}}_k \cdots \end{bmatrix}, \quad \overline{\mathbf{y}}_k \in \mathbb{R}^{C-N}, \quad \overline{\mathbf{y}}_k \stackrel{\text{def}}{=} \mathscr{M}_\lambda(\Delta^N \mathbf{y}_k), \quad k \in \mathbb{Z}. \tag{4.26}$$

Based on (4.24), we write $\overline{\mathbf{Y}} = \Delta^N_{T_\mathsf{d}} \mathbf{X}$, where the subscript T_d is used to denote that the operator is column-wise. The discrete-time Fourier transform (DTFT) along the rows of $\overline{\mathbf{Y}}$ yields the vector $\widehat{\overline{\mathbf{y}}}(\omega) = \begin{bmatrix} \widehat{\overline{y}}_0(\omega) & \widehat{\overline{y}}_1(\omega) & \cdots & \widehat{\overline{y}}_{C-N}(\omega) \end{bmatrix}^\top$, where $\widehat{\overline{y}}_c : \mathbb{R} \mapsto \mathbb{C}$ is the DTFT function and it satisfies,

$$\begin{aligned} \widehat{\overline{y}}_c(\omega) &\stackrel{\text{def}}{=} \sum_{k\in\mathbb{Z}} \left[\overline{\mathbf{Y}}_c\right]_k e^{-\jmath\omega k T_\mathsf{s}} \\ &= \sum_{i=0}^{N} (-1)^{N-i} \binom{N}{i} \sum_{k\in\mathbb{Z}} \left[\mathbf{X}_{c+i}\right]_k e^{-\jmath\omega k T_\mathsf{s}} = \left[\Delta^N \widehat{\mathbf{x}}(\omega)\right]_c, \end{aligned} \tag{4.27}$$

and $\widehat{\mathbf{x}}(\omega) = \begin{bmatrix} \widehat{x}_0(\omega) & \widehat{x}_1(\omega) & \cdots & \widehat{x}_{C-1}(\omega) \end{bmatrix}^\top$. In words, at any fixed ω, the DTFT function $\widehat{\overline{y}}_c(\omega)$ is equal to the finite differences of the DTFT functions computed from the original channels $\{x[c,k]\}_{c=0}^{C-1}$. The DTFT functions $\widehat{x}_c(\omega)$ are related to the multiband

signal $x(t)$ via

$$\widehat{x}_c(\omega) = \frac{T_{\mathsf{S}}}{L} \sum_{k\in\mathbb{Z}} [\mathbf{X}_c]_k \, e^{-\jmath\omega(k+\frac{c}{L})T_{\mathsf{S}}} = T_{\mathsf{S}} \sum_{l\in\mathbb{Z}} \widehat{x}\,(\omega - l\Omega_{\mathsf{S}})\, e^{-\jmath 2\pi l \frac{c}{L}}, \tag{4.28}$$

and similarly to (2.7) , over the interval $[0, 2\Omega_{\mathsf{S}})$ the finite bandwidth of x implies that

$$\widehat{x}_c(\omega) = T_{\mathsf{S}} \sum_{l=0}^{L-1} \widehat{x}\,(\omega - l\Omega_{\mathsf{S}})\, e^{-\jmath 2\pi l \frac{c}{L}}, \quad \omega \in [0, 2\Omega_{\mathsf{S}}). \tag{4.29}$$

Using this,

$$\begin{aligned}
\left[\Delta^N \widehat{\mathbf{x}}\,(\omega)\right]_c &= \sum_{i=0}^{N} (-1)^{N-i} \binom{N}{i} \widehat{\mathbf{x}}_{c+i}\,(\omega) \\
&= T_{\mathsf{S}} \sum_{l=0}^{L-1} \widehat{x}\,(\omega - l\Omega_{\mathsf{S}}) \sum_{i=0}^{N} (-1)^{N-i} \binom{N}{i} e^{-\jmath 2\pi l \frac{c+i}{L}} \\
&= T_{\mathsf{S}} \sum_{l=0}^{L-1} \widehat{x}\,(\omega - l\Omega_{\mathsf{S}})\, e^{-\jmath 2\pi l \frac{c}{L}} \left(e^{-\jmath 2\pi \frac{l}{L}} - 1\right)^N .
\end{aligned} \tag{4.30}$$

Let $\mathbf{h}_l \in \mathbb{C}^{C-N}$ with $[\mathbf{h}_l]_c = e^{-\jmath 2\pi l \frac{c}{L}} \left(e^{-\jmath 2\pi \frac{l}{L}} - 1\right)^N$, using a vector-matrix notation

$$\widehat{\overline{\mathbf{y}}}\,(\omega) = \mathbf{H}\overline{\mathbf{x}}(\omega), \text{ where} \tag{4.31}$$

$$\mathbf{H} \stackrel{\text{def}}{=} \begin{bmatrix} \mathbf{h}_0 & \mathbf{h}_1 & \dots & \mathbf{h}_{L-1} \end{bmatrix}, \quad \overline{\mathbf{x}}(\omega) \stackrel{\text{def}}{=} \begin{bmatrix} \widehat{x}\,(\omega) \\ \widehat{x}\,(\omega - \Omega_{\mathsf{S}}) \\ \vdots \\ \widehat{x}\,(\omega - (L-1)\Omega_{\mathsf{S}}) \end{bmatrix}.$$

Since the spectrum of x is composed of $2P$ passbands of width $2\Omega_{\mathsf{B}} < \Omega_{\mathsf{S}}$, we have that $\widehat{x}\left(\omega - l\Omega_{\mathsf{S}}\right) \not\equiv 0$ only for a subset of $\mathbb{I}_L$. This subset is called the *diversity set* of $\widehat{x}(\omega)$ and defined as [42]

$$\mathcal{S} \stackrel{\text{def}}{=} \bigcup_{\omega} \mathcal{S}_{\omega}, \quad \mathcal{S}_{\omega} = \left\{ l \in [0, L-1] : \left[\overline{\mathbf{x}}(\omega)\right]_l \not\equiv 0 \right\}. \tag{4.32}$$

This reflects that only $|\mathcal{S}| \leq 2P$ sub-intervals out of L are occupied. Therefore, (4.31) can become,

$$\widehat{\overline{\mathbf{y}}}\left(\omega\right) = \mathbf{H}^{\mathcal{S}} \overline{\mathbf{x}}_{\mathcal{S}}(\omega), \tag{4.33}$$

where columns of $\mathbf{H}$ and the rows of $\overline{\mathbf{x}}(\omega)$ are restricted to the set $\mathcal{S}$. The matrix $\mathbf{H}$ can be written as the product

$$\mathbf{H} = \mathbf{V} \begin{bmatrix} 0 & \left(e^{-\jmath\frac{2\pi}{L}} - 1\right)^N & \dots & \left(e^{-\jmath\frac{2\pi(L-1)}{L}} - 1\right)^N \end{bmatrix}^{\top},$$

where $\mathbf{V} \in \mathbb{C}^{(C-N)\times L}$ is composed from the first $C - N$ rows of an $L \times L$ discrete Fourier transform matrix. As discussed in [43], this matrix has a full row rank whenever $(C - N) \geq |\mathcal{S}|$. If $0 \notin \mathcal{S}$, then $\mathbf{H}^{\mathcal{S}}$ has full row rank as well. Compute the left pseudo-inverse $\mathbf{H}^{\dagger}_{\mathcal{S}}$ and apply on both sides of (4.33),

$$\mathbf{H}^{\dagger}_{\mathcal{S}} \widehat{\overline{y}}\left(\omega\right) = \overline{\mathbf{x}}_{\mathcal{S}}(\omega). \tag{4.34}$$

Then, $x(t)$ is obtained from $\overline{\mathbf{x}}_{\mathcal{S}}(\omega)$ as in [40]. ■

In Theorem 4.2, for a fixed time delay satisfying (4.23), greater channel redundancy (C relative to P) allows a higher finite-difference order N, which in turn accelerates amplitude decay. Conversely, by adjusting T_{d} the required number of additional channels can be reduced to

Algorithm 6: Unlimited Sensing for Multiband Signals (Multiphase)

Input: $y\left[c,k\right], c \in \mathbb{I}_C,\ k \in \mathbb{Z},\ \Omega_{\mathsf{B}},\ \Omega_{\mathsf{C}} = \{\omega_p\}_{p=0}^{P-1}, \mathrm{N}$.
Result: Fourier samples of a multiband signal x.

1) Let $\mathbf{y}_k \in \mathbb{R}^C,\ \left[\mathbf{y}_k\right]_c = y\left[c,k\right]$, and $\mathbf{Y} \overset{\text{def}}{=} \begin{bmatrix}\mathbf{y}_0 & \mathbf{y}_1 & \cdots & \mathbf{y}_k \cdots\end{bmatrix}$ defined in (4.25). Compute the finite differences along the columns, denoted $\Delta_{T_{\mathsf{d}}}^N \mathbf{Y}$.
2) Apply $\mathscr{M}_\lambda(\cdot)$to the elements of $\Delta_{T_{\mathsf{d}}}^N \mathbf{Y}$, giving $\overline{\mathbf{Y}} \overset{\text{def}}{=} \mathscr{M}_\lambda(\Delta_{T_{\mathsf{d}}}^N \mathbf{Y}) = \Delta_{T_{\mathsf{d}}}^N \mathbf{X}$ from (4.26).
3) Compute the DTFT along the rows of $\overline{\mathbf{Y}}$, giving the functions $\widehat{\overline{y}}_c\left(\omega\right)$ in (4.27).
4) Let $\mathbf{h}_l \in \mathbb{C}^{C-N}$ with $\left[\mathbf{h}_l\right]_c = e^{-\jmath 2\pi l \frac{c}{L}} \left(e^{-\jmath 2\pi \frac{l}{L}} - 1\right)^N$. Construct $\mathbf{H}$ in (4.31).
5) Construct the diversity set $\mathcal{S} = \{s_0, s_1, \cdots, s_{\#\mathcal{S}}\}$ in (4.32), restrict the columns of $\mathbf{H}$ to the set $\mathcal{S}$ as in (4.33). Then, compute $\mathbf{H}_{\mathcal{S}}^{\dagger}$.
6) Let $\overline{\mathbf{x}}\left(\omega\right) : \mathbb{R}^L \mapsto \mathbb{C}^L$, with functions

$$\left[\overline{\mathbf{x}}\left(\omega\right)\right]_l = \begin{cases} \left[\mathbf{H}_{\mathcal{S}}^{\dagger} \widehat{\overline{y}}\left(\omega\right)\right]_i, & \text{if } l = s_i \in S, \\ 0, & \text{if } \ell \notin S, \end{cases} \qquad \ell = 0, \ldots, L-1. \tag{4.35}$$

7) Compute $x\left[k\right] = \mathrm{IDTFT}\left(\overline{\mathbf{x}}\left(\omega\right)\right)$.

$N = P + 1$, when T_{d} satisfies $\left|\left|\Delta_{T_{\mathsf{d}}}\mathbf{X}\right|\right|_\infty \leq \lambda$. This demonstrates that by processing along both signal dimensions, we can achieve HDR reconstruction with minimal overhead on the sampling architecture.

Furthermore, the proposed method, as summarised in Algorithm 6, reconstructs the multiband samples directly from their finite differences, eliminating the need for a minimal number of samples in the vicinity of the unfolded value, as required by other local reconstruction techniques in the USF.

Robust Recovery on Finite Intervals

The solution approach and mathematical guarantees derived in the previous section highlight the benefits of spatiotemporal processing for USF-Multiband. However, the key hypothesis $r[c,k] \in 2\lambda\mathbb{Z}$ for all $c \in \mathbb{I}_C,\ k \in \mathbb{Z}$ is challenging to satisfy in practice. Violations of this may compromise the HDR capability and recovery precision of the method. In particular, hardware experiments reveal the following challenges:

- **Measurement Noise.** System and quantization noise can be amplified by the nonlinear filter (4.24), destabilising it and distorting recovery.
- **Hardware Imperfections.** Non-ideal analog folding can produce off-grid folds $r[k] \notin 2\lambda\mathbb{Z}$, causing spikes and degrading multiband reconstruction accuracy.

Problem Formulation. Considering the above factors, the model (4.18) becomes

$$y_\eta\left[c,k\right] = x\left[c,k\right] - r\left[c,k\right] + \eta\left[c,k\right], \tag{4.36}$$

where $\eta\left[c,k\right]$ accounts for noise and hardware imperfections. As noted, applying Algorithm 6 directly to the noisy modulo measurements $y_\eta\left[c,k\right]$ may fail under these conditions. To improve robustness, an optimization-based recovery algorithm has been proposed. Consider the first K columns of the matrix $\mathbf{Y}$, defined in (4.25). Applying the first-order finite differences (N=1) along the columns, we get

$$\overline{\mathbf{y}}_k = \overline{\mathbf{x}}_k - \overline{\mathbf{r}}_k, \quad k \in \mathbb{I}_K,$$

where $\overline{\mathbf{x}}_k, \overline{\mathbf{r}}_k$ are the corresponding first-order differences of the multiband and the residual samples, respectively. The problem to be solved is to find estimates for $\overline{\mathbf{x}}_k$ and $\overline{\mathbf{r}}_k$ via

$$\min_{\overline{\mathbf{x}}_k, \overline{\mathbf{r}}_k} \|\overline{\mathbf{y}}_k - (\overline{\mathbf{x}}_k - \overline{\mathbf{r}}_k)\|_{\ell^2}^2, \quad \text{for a fixed } k \in \mathbb{I}_K. \tag{4.37}$$

To relax the ill-posedness, priors reflecting the signal model are utilised. The smoothness of x is exploited by approximating its samples with a modulated polynomial model, that is

$$[\overline{\mathbf{x}}_k]_c \approx \sum_{p=0}^{P-1} \mathsf{H}(c; [\mathbf{q}_k]_p) e^{\jmath \omega_p T_{\mathsf{d}} c}, \tag{4.38}$$

where $\mathsf{H}(t; \boldsymbol{\tau})$ is a polynomial at variable t, and its coefficients are the elements of the vector $\boldsymbol{\tau} \in \mathbb{C}^P$. The error $\left| [\overline{\mathbf{x}}_k]_c - \sum_{p=0}^{P-1} \mathsf{H}(c; [\mathbf{q}_k]_p) e^{\jmath \omega_p T_{\mathsf{d}} c} \right|$ can be bounded on a finite interval of length $(C-1)T_{\mathsf{d}}$, and it decays rapidly w.r.t. the polynomial order. For r, we exploit the sparsity of $\overline{\mathbf{r}}_k$, that is [23],

$$[\overline{\mathbf{r}}_k]_c = \sum_{m=0}^{M_k - 1} [\boldsymbol{\alpha}_k]_m \, \delta\left[c - [\boldsymbol{\beta}_k]_m\right], \quad [\boldsymbol{\alpha}_{\boldsymbol{k}}]_m \in 2\lambda\mathbb{Z}, \quad [\boldsymbol{\beta}_{\boldsymbol{k}}]_m \in \mathbb{I}_{C-1}, \tag{4.39}$$

where $\{[\boldsymbol{\alpha}_k]_m, [\boldsymbol{\beta}_{\boldsymbol{k}}]_m\}_{m=0}^{M_k}$ are pairs of the amplitudes and folding instants, respectively, and $\delta[k]$ is the Dirac delta function. Adding the priors (4.38) and (4.39) to (4.37) we arrive at

the optimization problem

$$\min_{\mathbf{q}_k,\boldsymbol{\alpha_k},\boldsymbol{\beta_k}} \|\overline{\mathbf{y}}_k - (\overline{\mathbf{x}}_k - \overline{\mathbf{r}}_k)\|_{\ell^2}^2, \text{ s.t. } [\overline{\mathbf{x}}_k]_c = \sum_{p=0}^{P-1} \mathsf{H}(c; [\mathbf{q}_k]_p) e^{\jmath\omega_p T_{\mathrm{d}} c}, \tag{4.40}$$
$$[\overline{\mathbf{r}}_k]_c = \sum_{m=0}^{M_k-1} [\boldsymbol{\alpha}_k]_m \, \delta\left[c - [\boldsymbol{\beta}_k]_m\right], \quad [\boldsymbol{\alpha_k}]_m \in 2\lambda\mathbb{Z}, \quad [\boldsymbol{\beta_k}]_m \in \mathbb{I}_{C-1}.$$

Solution Strategy. The constrained problem (4.40) is non-convex and challenging to solve. To address this, we decompose the problem into two tractable sub-problems and solve them by alternating minimisation:

1. In P1, we retrieve $\boldsymbol{\alpha}_k, \boldsymbol{\beta}_k$ using sparse approximation.

2. In P2, we fit the modulated polynomial model (4.38) to the estimate of $\overline{\mathbf{x}}_k$.

Sub-problem P1. Assuming that $\overline{\mathbf{x}}_k$ is known, we estimate $\overline{\mathbf{r}}_k$ by minimizing,

$$\text{(P1)} \qquad \min_{\boldsymbol{\alpha_k},\boldsymbol{\beta_k}} \left\|\widetilde{\overline{\mathbf{r}}}_k - \overline{\mathbf{r}}_k\right\|_{\ell^2}^2, \text{ s.t. } \widetilde{\overline{\mathbf{r}}}_k = \overline{\mathbf{x}}_k - \overline{\mathbf{y}}_k$$
$$[\overline{\mathbf{r}}_k]_c = \sum_{m=0}^{M_k-1} [\boldsymbol{\alpha}_k]_m \, \delta\left[c - [\boldsymbol{\beta}_k]_m\right], \quad [\boldsymbol{\alpha_k}]_m \in 2\lambda\mathbb{Z}, \quad [\boldsymbol{\beta_k}]_m \in \mathbb{I}_{C-1}, \tag{4.41}$$

which is a non-convex problem. To find the solution to (4.41), we leverage the following continuous-time, sparse parametrisation as the ratio of two polynomials [49]:

$$[\overline{\mathbf{r}}_k]_c = \frac{\mathsf{P}_k([\boldsymbol{\zeta}_{C-1}]_c)}{\mathsf{Q}_k([\boldsymbol{\zeta}_{C-1}]_c)}, \qquad \begin{matrix} \mathsf{P}_k \in P_{M_k-1} \\ \mathsf{Q}_k \in P_{M_k} \end{matrix}, \quad [\boldsymbol{\zeta}_{C-1}]_c = e^{\jmath\frac{2c\pi}{C-1}}. \tag{4.42}$$

The roots of Q_k uniquely determine the spike locations $\boldsymbol{\beta}_k$ as $\mathsf{Q}_k([\mathbf{u}_k]_m) = 0 \iff [\mathbf{u}_k]_m =$

$e^{\jmath 2\pi[\boldsymbol{\beta}_k]_m/(C-1)}$, $m \in \mathbb{I}_{M_k}$. Consequently, (4.41) can be equivalently re-formulated as,

$$\min_{\mathsf{Q}_k,\mathsf{P}_k} \sum_{c=0}^{C-2} \left| [\overline{\mathbf{r}}_k]_c - \frac{\mathsf{P}_k(\left[\boldsymbol{\zeta}_{C-1}\right]_c)}{\mathsf{Q}_k(\left[\boldsymbol{\zeta}_{C-1}\right]_c)} \right|^2. \tag{4.43}$$

The numerator P_k can be found exactly by solving a linear system of equations, as soon as the denominator Q_k is known. Hence, (4.43) can be considered as minimizing on Q_k alone. Still (4.43) is non-convex, it is solved iteratively, where we construct a collection of estimates for Q_k and choose the one that leads to the minimal mean-squared error on the measurements $\mathbf{y}$ via (4.43).

Sub-problem P2**.** With $\mathbf{r}$ known, finding $\mathbf{q}_k$ boils down to a linearly constrained quadratic minimization problem, which is formulated as,

$$(\mathsf{P2}) \qquad \min_{\mathbf{q}_k} \ \|\widetilde{\mathbf{x}} - \mathbf{x}\|_{\ell^2}^2, \ \text{ s.t. } \ \widetilde{\mathbf{x}} = \mathbf{y} + \mathbf{r}, \quad [\overline{\mathbf{x}}_k]_c = \sum_{p=0}^{P-1} \mathsf{H}(c; [\mathbf{q}_k]_p) e^{\jmath \omega_p T_{\mathsf{d}} c}. \tag{4.44}$$

The procedure of solving the sub-problems P1 and P2 is carried out iteratively, ultimately yielding $C-1$ unfolded estimates of the vector $\widetilde{\overline{\mathbf{x}}}_k$ for a given k. By repeating it for all $k \in \mathbb{I}_K$, we get the first K columns of the matrix $\mathbf{X}$ in (4.25).

Interpolation. By following the logic as steps 3)-7) in Algorithm 6 while operating in the discrete Fourier domain rather than the discrete-time Fourier domain, the sequence $x\,(t)\,|_{t=kT_{\mathsf{d}}}$ is recovered on the dense grid $t = kT_{\mathsf{d}}$, for $k \in \mathbb{I}_{KL}$.

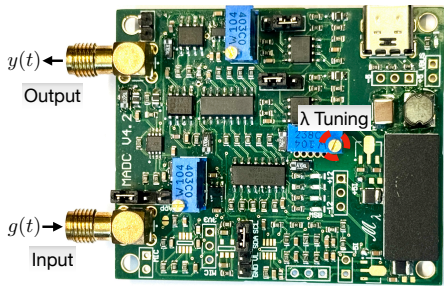


Figure 4.7: $\mathscr{M}$ –ADC hardware prototype. The testbed is designed such that experimental parameters, including the sampling step T_{S}, time delay T_{d}, and threshold λ, are tunable.

Hardware Experiments

The translation of theory into practice was evaluated by assessing the algorithmic performance under synthetic noise (see [100]) and real hardware experiments.

Experimental Protocol. The analog, HDR signal x is fed to the `USF-MC` hardware, as depicted in Fig. 4.7. The original HDR input as ground truth and $\mathscr{M}$ –ADC outputs are simultaneously recorded on the `PicoScope 3406D` oscilloscope at 8 bits and 4 bits resolution, respectively. The performance of the method is compared with that of the conventional multichannel pipeline[42], using the same 4 bits quantization as the $\mathscr{M}$ –ADC.

Weak-Strong Mixtures. The coexistence of weak and strong targets in multiband sensing is a long-standing challenge: reliable recovery must deliver both HDR and HDRes. In the experiment, the ratio between the dynamic range of the two signal components is set to: $\|\varphi_3\|_\infty / \|\varphi_2\|_\infty = 100$, as shown in Fig. 4.8(c). As shown in Fig. 4.8(b–c), the conventional method misses the weak component, whereas the proposed algorithm reconstructs both components with MSE $\approx 10^{-3}$ using as few as 4- bit quantization. Both the strong and weak signal components match the 8-bit ground truth data.

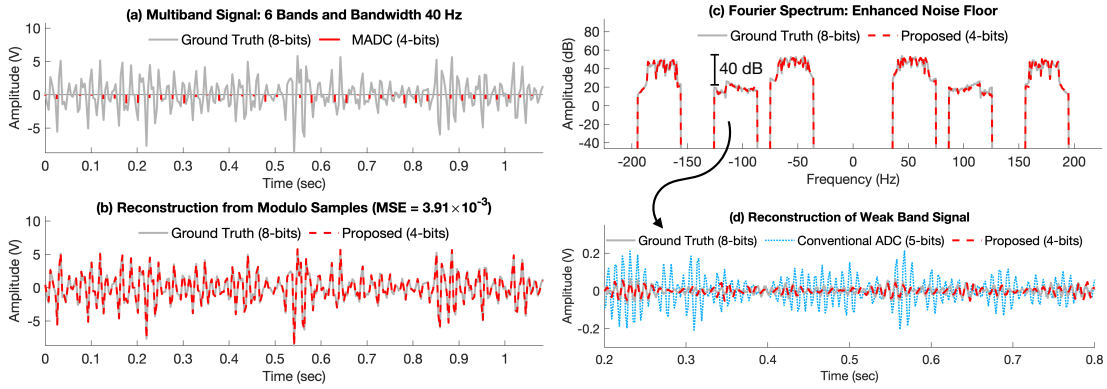


Figure 4.8: Hardware experiment: weak-strong mixtures ($\|x\|_\infty = 13.64\lambda$). (a) Input signal and measurements. (b) Signal reconstruction. (c) Recovered spectrum. (d) Recovered weak signal components. The input signal x consists of 6 bands ($\{\varphi_i\}_{i=1}^6$), with a DR ratio of $\|\varphi_3\|_\infty / \|\varphi_2\|_\infty = 100$. Under 5 bits quantization, a conventional ADC avoids clipping φ_3 but fails to capture φ_2 due to coarse quantization step (≈ 0.56), which far exceeds the DR of φ_2, as shown in (d). In contrast, the proposed method precisely recovers both strong and weak components using a reduced quantization budget of 4 bits.

Spectral Super-Resolution. In practice, noise limits how closely spaced spectral bands can be separated. In a band super-resolution experiment, a case with bands only 4.46 Hz apart is evaluated. The input dynamic range is $15.71\times$ the ADC's dynamic range, and sampling is performed with a downsampling factor of 9.44, and $\approx 4-$bit quantization. Despite these constraints, the proposed method achieves a recovery with MSE 2.06×10^{-2}.

Dense Spectrum Sensing. Considering a spectral support where the number of bands is large, and band separation is small, the input signal in this experiment has $K = 16$ bands with separation of 51.24 Hz, covering the spectrum from 46.33 Hz to 663.24 Hz. In this setup, the `USF-MC` attains $7.61\times$ dynamic range extension and $36.95\times$ downsampling, using a 4.25-bit quantization budget, which pushes the algorithm's stability and robustness limits. The precise signal reconstruction with an MSE $\approx 10^{-2}$ together with the low sampling rate and bit budget demonstrates the potential of the `USF-MC` pipeline to expand the sensing capability for multiband signal detection.

Multiband Separation from a Strong Tone. The presence of a strong jamming signal within the multiband signal spectrum is a known issue in RF communications. Conventionally, this requires designated hardware or expansion of the ADC's dynamic range, which leads to coarser quantization. Due to the amplitude folding, the USF can accommodate such interference even at an unknown frequency. To test this, the signal in the designed experiment has a strong tone with an unknown frequency around 100 Hz, present within the multiband spectrum. We set $\lambda = 0.66$ and $f_s = 40.21$ Hz, leading to 15.47-fold dynamic range extension and a downsampling factor of 9.84. In the presence of measurement noise and folding non-idealities, the method accurately separates the multiband signal and the tone using only 3 bits, matching the result from high-resolution (8 bits) ground truth.

4.4 Conclusion

In this chapter, the Unlimited Sensing Framework (USF) was extended to multiband acquisition under high dynamic range and high digital resolution constraints. We demonstrated how the spectral structure of multiband signals can be coupled with modulo folding to enable stable recovery at sub-Nyquist rates, without incurring the prohibitive bit-depth requirements typically associated with classical sub-Nyquist methods. Building on this perspective, we introduced recovery guarantees, algorithms, and validations that together form a practical USF-Multiband pipeline.

The first insight is that exploiting the Fourier structure of multiband signals is possible even within the Unlimited Sensing Framework. This leads to the recovery guarantee for uniform sampling, which decouples the required sampling rate from the maximum carrier frequency and ties it to the occupied spectrum alone. To translate this into practice, we derived a single-

channel algorithm operating directly on frequency-aware differences.

To address spectral aliasing and practical nonidealities, including noise, quantization, and non-ideal modulo behaviour, we introduce a multiphase sampling approache. Carefully chosen phases (as time-delays) create spatial redundancy, enabling effective modulo unfolding while maintaining sub-Nyquist rates. The unfolded channels are then combined in a high-order difference domain to cancel aliasing effects. We emphasise that a multiphase model is not the most general multichannel form. A genuinely multichannel USF model, involving distinct input channels and possible inter-channel dependencies, remains an interesting direction for future work.

Finally, we instantiate a practical, quantization-aware reconstruction algorithm that is robust to common non-idealities. In hardware tests, the algorithm reconstructs weak and strong signal components, operates reliably on densely occupied spectra, and achieves spectral super-resolution while maintaining sub-Nyquist sampling rates.

5

Unlimited Sensing for Continuous-wave Time-of-Flight and Second Order Bandpass Sampling

5.1 HDR-ToF: HDR Time-of-Flight Imaging via Modulo Acquisition

5.1.1 Motivation and Contributions

Continuous-wave Time-of-Flight (CW-ToF) imaging is a compact and efficient consumer-grade 3D imaging technology [103, 104, 105, 106, 19, 107, 108]. The dynamic range bottleneck of conventional ADCs limits the ability to recover both the amplitude and phase parameters when signals of the form in (5.1) are sampled. This raises an issue, because with the widespread applications of 3D imaging in areas such as robotics, surveillance, remote sensing [109], scientific imaging, and autonomous navigation [110], reliability and stability are required; hence, the development of 3D HDR imaging solutions. While pure algorithmic solutions [111, 112, 113] lack guarantees for errorless recovery, other solutions based on advanced hardware design [114, 115], are often complex and impractical for off-the-shelf products.

Mathematically, the signals that are utilised in CW-ToF systems belong to the class of single-tone signals $x_{\mathsf{ST}}(t) = Ae^{\jmath(\omega_0 t+\theta)}$. This can be derived by setting $P = 1$ and $\varphi(t) = Ae^{\jmath\theta}$, $A \in \mathbb{R}, \theta \in [0, 2\pi)$ in (2.2). We consider real-valued signals corresponding to $P = 2$ and $\Omega_{\mathsf{C},0} = -\Omega_{\mathsf{C},1}$ so the mathematical model becomes

$$x_{\mathsf{ST}}(t) = \frac{A}{2}\left(e^{\jmath(\omega_0 t+\theta)} + e^{-\jmath(\omega_0 t+\theta)}\right) = \cos(\omega_0 t + \theta). \tag{5.1}$$

Using a $\mathscr{M}$–ADC can prevent saturation, but sampling of signals of the form (5.1) based on the bandlimited model (Theorem 2.5) is sub-optimal as it requires samples on the real line and does not leverage the parametric structure of (5.1). The sum-of-sines model considered in [81] is a related problem; however, the technique requires unfolding of the modulo signals,

which necessitates a suboptimal sampling rate and number of measurements.

This work develops a USF-based acquisition technique for single-shot HDR ToF imaging that operates at a moderate oversampling factor. The main contributions are:

1) Novel architecture for HDR ToF imaging. The proposed camera utilises modulo non-linearity in the acquisition stage. The inverse problem of recovering the ToF image from folded measurements is formulated.

2) Sampling density criterion. A mathematical guarantee for ToF recovery from modulo samples is derived, showing a factor of $\frac{2\pi e}{3}$ reduction compared to the USF Theorem 2.5.

3) Recovery algorithm. The proposed algorithmic procedure directly recovers a 3D image from finitely many modulo ToF samples *without* the requirement for inversion or unfolding of modulo samples.

5.1.2 HDR CW–ToF Imaging via Unlimited Sensing

Conventional CW–ToF imaging is based on lock-in sensor-based homodyne detection [106]. Depth imaging is accomplished by probing the scene with a sinusoidal illumination (hence CW–ToF). This strategy is the workhorse of ToF systems such as the Microsoft Kinect [106] and photonic mixer devices [116]. Mathematically, the scene is illuminated with a *probing signal* $p(t) = 1 + \rho_0 \cos(\omega_0 t), \rho_0 < 1$ where ω_0 is the modulation frequency, typically in MHz. The interaction of $p(t)$ with the scene $h_{\mathbf{r}}(t)$ results in the *back-scattered* signal $q_{\mathbf{r}}(t) = (p * h_{\mathbf{r}})(t)$. Let $\overline{p}(t) = p(-t)$. The amplitude at the scene point and the distance from the sensor are encoded in the signal $q_{\mathbf{r}}(t)$, illustrated in Fig. 5.1. The lock-in sensor

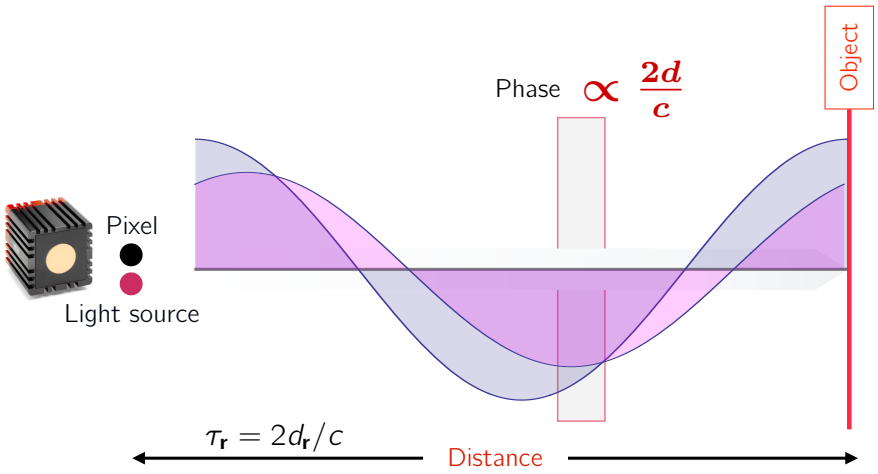


Figure 5.1: An illustration of the probing and the back-scattered waveforms in a continuous wave time-of-flight sensor.

cross-correlates $q_{\mathbf{r}}(t)$ with $p(t)$ resulting in the ToF measurements $(q_{\mathbf{r}} * \overline{p})$ that simplify to,

$$m_{\mathbf{r}}(t) = \Gamma_{\mathbf{r}}\left(1 + \frac{\rho_0^2}{2}\cos(\omega_0 t + \theta_{\mathbf{r}})\right), \theta_{\mathbf{r}} = \omega_0 \tau_{\mathbf{r}} \in [0, 2\pi], \tag{5.2}$$

where the phase $\theta_{\mathbf{r}}$ encodes the depth information. The parameters $\{\Gamma, \tau = 2z/c\}$, where c is the velocity of light, are efficiently recovered from the samples of $m_{\mathbf{r}}(t)$ via the "Four Bucket Method" [106, 116] summarised below.

Four Bucket Method (FBM)

1. Starting with 4 measurements, $m_{\mathbf{r}}[k] = m_{\mathbf{r}}\left(\frac{\pi k}{2\omega_0}\right), k \in [0, 3]$,

$$\begin{bmatrix} m_{\mathbf{r}}[0] & m_{\mathbf{r}}[1] \\ m_{\mathbf{r}}[2] & m_{\mathbf{r}}[3] \end{bmatrix} = \frac{\Gamma_{\mathbf{r}}}{2}\begin{bmatrix} 2 + \rho_0^2\cos(\theta_{\mathbf{r}}) & 2 - \rho_0^2\sin(\theta_{\mathbf{r}}) \\ 2 - \rho_0^2\cos(\theta_{\mathbf{r}}) & 2 + \rho_0^2\sin(\theta_{\mathbf{r}}) \end{bmatrix} \tag{5.3}$$

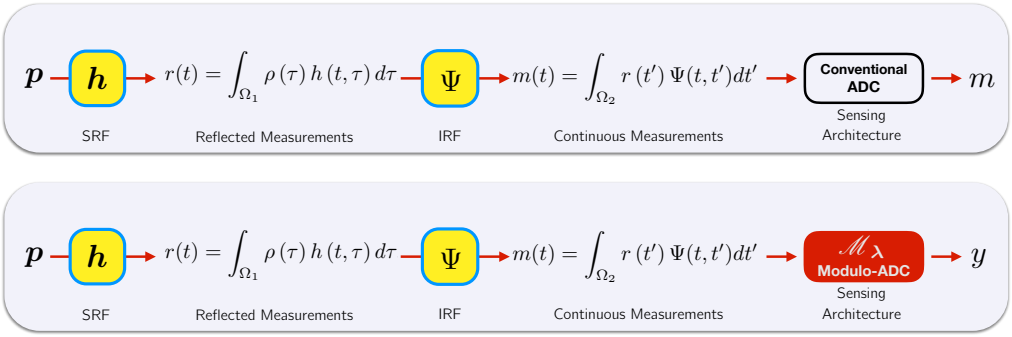


Figure 5.2: The sampling pipeline of: (Upper) a conventional continuous-wave time-of-flight sensor, and (Lower) our proposed HDR-ToF system

2. a complex-valued phasor is constructed from $m_{\mathbf{r}}[k] \in \mathbb{R}$,

$$\mathsf{c}_{\mathbf{r}} \overset{\text{def}}{=} \underbrace{(m_{\mathbf{r}}[0] - m_{\mathbf{r}}[2])}_{\rho_0^2 \Gamma_{\mathbf{r}} \cos(\theta_{\mathbf{r}})} + \jmath \underbrace{(m_{\mathbf{r}}[3] - m_{\mathbf{r}}[1])}_{\rho_0^2 \Gamma_{\mathbf{r}} \sin(\theta_{\mathbf{r}})} \equiv \underbrace{\rho_0^2 \Gamma_{\mathbf{r}} e^{\jmath \omega_0 \frac{2z_{\mathbf{r}}}{c}}}_{\text{ToF Phasor}} \tag{5.4}$$

3. the albedo and depth are estimated via $\widetilde{\Gamma}_{\mathbf{r}} = |\mathsf{c}_{\mathbf{r}}| / \rho_0^2$ and $\widetilde{z}_{\mathbf{r}} = (c/2\omega_0) \angle \mathsf{c}_{\mathbf{r}}$, respectively.

Problem Formulation

To enable HDR functionality in ToF imaging, the cross-correlation function in (5.2) is sampled using the $\mathscr{M}$–ADC. The resulting samples are given by,

$$y[k] \overset{(2.10)}{=} \mathscr{M}_\lambda(m_{\mathbf{r}}(kT_{\mathsf{S}})) \equiv \left(\tfrac{\lambda}{\pi}\right) \angle e^{\jmath \left(\frac{\pi}{\lambda}\right) m_{\mathbf{r}}(kT_{\mathsf{S}})}, \quad \lambda \in \mathbb{R}_{>0} \tag{5.5}$$

where $T_{\mathsf{S}} \in \mathbb{R}^+$ is the sampling period. The goal is to recover $\Gamma_{\mathbf{r}}, \theta_{\mathbf{r}}$ from the modulo samples. Due to the modulo folding, applying the FBM method on $y[k]$ would not recover the desired parameters. As mentioned, a possible recovery strategy is to first unfold $y[k]$ to $m_{\mathbf{r}}[k]$, but

this does not leverage the parametric structure of (5.2).

Recovery Strategy

Let $m_{\mathbf{r}}[k] = m_{\mathbf{r}}(kT_{\mathsf{S}})$, $T_{\mathsf{S}} > 0$. Then, we have,

$$(\Delta m_{\mathbf{r}})[k] = -\Gamma_{\mathbf{r}}\rho_0^2 \sin\left(\frac{\omega_0 T_{\mathsf{S}}}{2}\right) \sin\left(\frac{\omega_0 T_{\mathsf{S}}}{2} + kT_{\mathsf{S}}\omega_0 + \theta_{\mathbf{r}}\right). \tag{5.6}$$

For $N > 1$, recursively applying the above yields,

$$\begin{aligned}\left(\Delta^N m_{\mathbf{r}}\right)[k] &= \Delta\left(\Delta^{N-1} m_{\mathbf{r}}\right)[k] \\ &\Rightarrow\ 2^N \left(\tfrac{\Gamma_{\mathbf{r}}\rho_0^2}{2}\right) \sin^N\left(\tfrac{\omega_0 T_{\mathsf{S}}}{2}\right) \cos\left(k\omega_0 T_{\mathsf{S}} + \tfrac{N}{2}\left(\omega_0 T_{\mathsf{S}} + \pi\right) + \theta_{\mathbf{r}}\right).\end{aligned} \tag{5.7}$$

From the above, we note that $\|\Delta m_{\mathbf{r}}\|_\infty \leq |\Gamma_{\mathbf{r}}\rho_0^2/2|\,|2\sin(\omega_0 T_{\mathsf{S}}/2)|^N$ and *amplitude shrinkage* is achieved via oversampling, whenever

$$\sin\left(\frac{\omega_0 T_{\mathsf{S}}}{2}\right) < \frac{1}{2} \Rightarrow 0 < T_{\mathsf{ToF}} < \frac{\pi}{3\omega_0}. \tag{5.8}$$

Hence, choosing T_{ToF} as above, we can upper bound $\|\Delta m_{\mathbf{r}}\|_\infty$ by the modulo threshold $\lambda \in \mathbb{R}_{>0}$, whenever,

$$N \geqslant \left\lceil \frac{\log(\lambda) - \log\left(\beta_\rho^\Gamma\right)}{\log\left(2\sin\left(\omega_0 T_{\mathsf{S}}/2\right)\right)} \right\rceil, \quad \beta_\rho^\Gamma \geqslant \left|\frac{1}{2}\Gamma_{\mathbf{r}}\rho_0^2\right|. \tag{5.9}$$

Equations (5.8) and (5.9) prescribe how to choose T_{S} and N such that the commutativity in a certain sense [20] of $\mathscr{M}_\lambda(\cdot)$ and Δ^N as in (5.10), holds. Using this, we can access the higher

order differences of $m_{\mathbf{r}}$ because,

$$\mathscr{M}_\lambda(\Delta^N \mathscr{M}_\lambda(m_{\mathbf{r}})) = \mathscr{M}_\lambda(\Delta^N y) = \Delta^N m_{\mathbf{r}}, \qquad N > 0. \tag{5.10}$$

Recovery Algorithm. The proposed algorithm directly recovers the ToF parameters from higher-order differences samples $\Delta^N m_{\mathbf{r}}$. Under the conditions in (5.8) and (5.9), we compute,

$$y\left[k\right] \xrightarrow{\Delta^N} \boxed{\overline{y} = \Delta^N y} \xrightarrow{\mathscr{M}_\lambda(\cdot)} \boxed{\mathscr{M}_\lambda(\overline{y})} \xrightarrow{(5.10)} \overline{m}_{\mathbf{r}}\left[k\right] \tag{5.11}$$

where $\overline{m}_{\mathbf{r}}\left[k\right] = \left(\Delta^N m_{\mathbf{r}}\right)\left[k\right]$ is vectorized as $\overline{\mathbf{m}} \in \mathbb{R}^{(K-N)\times 1}$ with vector element $\left[\overline{\mathbf{m}}\right]_k = \overline{m}_{\mathbf{r}}\left[k\right]$. Let us define,

$$\psi^N_{\omega_0 T_{\mathsf{S}}}\left[k\right] \stackrel{\text{def}}{=} \left(k\omega_0 T_{\mathsf{S}} + \tfrac{N}{2}\left(\omega_0 T_{\mathsf{S}} + \pi\right)\right), \quad T_{\mathsf{S}} < \tfrac{\pi}{3\omega_0}.$$

Using the identity $\cos\left(\psi^N_{\omega_0 T_{\mathsf{S}}}\left[k\right] + \theta_{\mathbf{r}}\right) = \cos\left(\theta_{\mathbf{r}}\right)\cos\left(\psi^N_{\omega_0 T_{\mathsf{S}}}\left[k\right]\right) - \sin\left(\theta_{\mathbf{r}}\right)\sin\left(\psi^N_{\omega_0 T_{\mathsf{S}}}\left[k\right]\right)$ we can now isolate $\theta_{\mathbf{r}}$. For $k \in [0, L-1]$ with $L \geq K - N$ and N given in (5.9), the unknowns $\{\Gamma_{\mathbf{r}}, \theta_{\mathbf{r}}\}$ can now be estimated via *least-squares solution* to the system of equations $\overline{\mathbf{y}}_\lambda = \mathbf{DTp}$,

$$\underbrace{\begin{bmatrix} \mathscr{M}_\lambda(\overline{y}\left[0\right]) \\ \vdots \\ \mathscr{M}_\lambda(\overline{y}\left[L-1\right]) \end{bmatrix}}_{\overline{\mathbf{y}}_\lambda} = \kappa^N_{T_{\mathsf{S}}} \underbrace{\left[\begin{array}{c|c} \cos\left(\psi^N_{\omega_0 T_{\mathsf{S}}}\left[0\right]\right) & -\sin\left(\psi^N_{\omega_0 T_{\mathsf{S}}}\left[0\right]\right) \\ \vdots & \vdots \\ \cos\left(\psi^N_{\omega_0 T_{\mathsf{S}}}\left[L-1\right]\right) & -\sin\left(\psi^N_{\omega_0 T_{\mathsf{S}}}\left[L-1\right]\right) \end{array}\right]}_{\mathbf{T}} \underbrace{\begin{bmatrix} \Gamma_{\mathbf{r}}\cos\left(\theta_{\mathbf{r}}\right) \\ \Gamma_{\mathbf{r}}\sin\left(\theta_{\mathbf{r}}\right) \end{bmatrix}}_{\mathbf{p}} \tag{5.12}$$

where,

- $\overline{\mathbf{y}}_\lambda \in \mathbb{R}^{L\times 1}$ is the vector of modulo measurements such that $[\overline{\mathbf{y}}_\lambda]_l = (\Delta^N m_{\mathbf{r}})\,[l]$ (cf. (5.11)).
- $\mathbf{D} \in \mathbb{R}^{L\times L}$ is a diagonal matrix with elements given by $[\mathbf{D}]_{l,l} = \kappa_{T_\mathsf{S},N} \overset{\text{def}}{=} \frac{\rho_0^2}{2}\left(2\sin\left(\frac{\omega_0 T_\mathsf{S}}{2}\right)\right)^N$ with N in (5.9).
- $\mathbf{T} \in \mathbb{R}^{L\times 2}$ is a matrix of sinusoids defined in (5.12).
- $\mathbf{p}^{2\times 1}$ is the unknown vector from which ToF phasor is constructed via $\mathsf{c}_{\mathbf{r}}^{\lambda} = [\mathbf{p}]_1 + \jmath\,[\mathbf{p}]_2 = \Gamma_{\mathbf{r}} e^{\jmath\theta_{\mathbf{r}}}$ yielding $\{\Gamma_{\mathbf{r}}, \theta_{\mathbf{r}}\}$.

Whenever $L > 1$ or $K > N+1$, $\mathbf{p}$ (or $\mathsf{c}_{\mathbf{r}}^{\lambda}$), is estimated via $\mathbf{p} = \kappa_{T_\mathsf{S},N}^{-1}\,(\mathbf{T}^{+}\overline{\mathbf{y}}_\lambda)$ where $\mathbf{T}^{+}$ denotes matrix pseudo-inverse. Next we provide a simplified algorithm that estimates $\{\Gamma_{\mathbf{r}}, \theta_{\mathbf{r}}\}$ from *two samples*, namely, $\mathscr{M}_\lambda(\bar{y}\,[0])$ and $\mathscr{M}_\lambda(\bar{y}\,[1])$ or $N+2$ samples $y\,[k]$.

The result is summarised in the next theorem.

Theorem 5.1 [Modulo Time-of-Flight Imaging [96]]

Let $y\,[k]$ be defined in (5.5) *be the modulo samples obtained from a lock-in sensor-based ToF imager, operating at modulation frequency ω_0. Furthermore, let us assume an upper bound $\beta_\rho^\Gamma \geqslant \left|\frac{1}{2}\Gamma_{\mathbf{r}}\rho_0^2\right|$ is known. Then, the unknown scene parameters $\{\Gamma_{\mathbf{r}}, \theta_{\mathbf{r}}\}$ in* (5.2) *can be estimated from $N+2$ modulo samples provided that the sampling time satisfies $T_{\mathsf{ToF}} < \pi/3\omega_0$ and where N is given in* (5.9).

The proof of this theorem is constructive and is based on the proposed algorithm, for which a simplified version that estimates $\{\Gamma_{\mathbf{r}}, \theta_{\mathbf{r}}\}$ from *two samples*, namely, $\mathscr{M}_\lambda(\bar{y}\,[0])$ and $\mathscr{M}_\lambda(\bar{y}\,[1])$ or $N+2$ samples $y\,[k]$, is described below.

ToF Estimation from $N+2$ Modulo Samples

1. **Step 1: Obtaining Modulo Samples.** Let $T_{\mathsf{ToF}} < \pi/3\omega_0$ and suppose an upper bound $\beta_\rho^\Gamma \geqslant \left|\frac{1}{2}\Gamma_{\mathbf{r}}\rho_0^2\right|$ is known based on which $N^\star = N$ is computed from (5.9). Using this, we get $y[k], k \in [0, K-1]$ modulo samples in (5.5) with $K > N^\star + 1$.

2. **Step 2: ToF Estimation.** Using (5.11), we compute $Y_k \overset{\text{def}}{=} \mathscr{M}_\lambda(\bar{y}[k]), k = 0, 1$. For $\mathbf{T} \in \mathbb{R}^{2\times 2}$, its inverse is given by,

$$\mathbf{T}_{\mathsf{inv}} = \frac{1}{\sin(\omega_0 T)} \begin{bmatrix} \sin(\nu_1) & -\sin(\nu_0) \\ \cos(\nu_1) & -\cos(\nu_0) \end{bmatrix}, \nu_k \overset{\text{def}}{=} \psi_{\omega_0 T}^{N^\star}[k].$$

Analogous to (5.4), we define the phasor,

$$\begin{aligned} \mathsf{c}_{\mathbf{r}}^\lambda &= \frac{(Y_0 \sin(\nu_1) - Y_1 \sin(\nu_0)) + \jmath\,(Y_0 \cos(\nu_1) - Y_1 \cos(\nu_0))}{\kappa_{T,N^\star} \sin(\omega_0 T)} \\ &\equiv \Gamma_{\mathbf{r}} \cos(\theta_{\mathbf{r}}) + \jmath \Gamma_{\mathbf{r}} \sin(\theta_{\mathbf{r}}) = \Gamma_{\mathbf{r}} e^{\jmath\theta_{\mathbf{r}}}. \end{aligned} \tag{5.13}$$

Thus, $|\mathsf{c}_{\mathbf{r}}^\lambda|$ and $\angle\mathsf{c}_{\mathbf{r}}^\lambda$ amount to $\{\Gamma_{\mathbf{r}}, \theta_{\mathbf{r}}\}$, respectively.

Numerical Demonstration

The effectiveness of the HDR ToF imaging approach is validated numerically, using a 3D bunny model from [117]. The transient image has amplitudes $\Gamma_{\mathbf{r}} \in [0, 255]$ and depth values $z_{\mathbf{r}} \in [0.1, 6]$ meters, shown in Fig. 5.3(a), where $\mathbf{r} \in \mathbb{R}^{402\times 400}$. The back-scattered signal $q_{\mathbf{r}}$ is computed and cross-correlated with a sinusoidal probing signal of angular frequency $\omega_0 = 2\pi \cdot 20 \times 10^6$ rad/s. This results in $\Gamma_{\mathbf{r}} \in [0.5, 377]$ and $\theta_{\mathbf{r}} \in [0.08, 1.6\pi]$.

Signal Acquisition. The modulo signal is generated as in (5.5) with $\lambda = 10$, and compared to a saturated signal where amplitudes are clipped to the range $[-\lambda, \lambda]$. Both signals are sam-

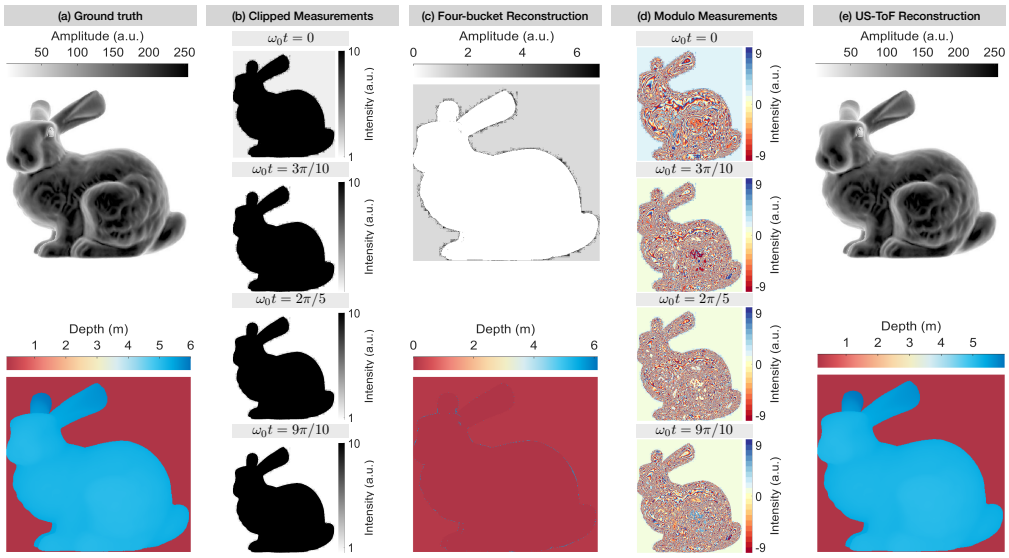


Figure 5.3: 3D imaging from simulated Time-of-Flight (ToF) measurements of the *"Stanford Bunny"* [117]. The probing sinusoidal signal frequency is $f_0 = 20$[MHz], modulo threshold is $\lambda = 10$ and the sampling rate is $T_\mathsf{S} = 1/(6.66 f_0)$. (a) Ground truth transient image composed of amplitude and depth maps. (b) Four equidistant samples of a ToF signal. Values are clipped to the range $[-\lambda, \lambda]$. (c) Reconstruction with the four-bucket algorithm using 4 equidistant samples over a period, sampled at rate $T_\mathsf{S} = 1/(4 f_0)$. (d) Four equidistant modulo samples of the ToF signal with modulo threshold λ. (e) Reconstruction from modulo samples with the US-ToF algorithm. The order of differences is $N = 27$. The mean squared error (MSE) for the amplitude and depth maps is on the order of 10^{-9} and 10^{-12}, respectively.

pled at rate $T_\mathsf{S} = \pi/(3.33\omega_0)$, just slightly below T_ToF from (5.8). The clipped measurements (Fig. 5.3(b)) exhibit information loss, while modulo acquisition (Fig. 5.3(d)) preserves unique spatiotemporal mappings due to the nonlinear modulo mapping, enabling near-exact recovery.

Algorithm Performance. Using (5.9) with $N = 27$, our algorithm achieves MSE values of 10^{-9} for $\Gamma_\mathbf{r}$ and 10^{-12} for $z_\mathbf{r}$. Non-exact recovery is attributed to the quantization error introduced by finite precision arithmetic. This result validates Theorem 5.1, and demonstrates recovery of amplitudes $\approx 19\times$ larger than the ADC range, as shown in Fig. 5.3(e), which is visually indistinguishable from the ground truth (Fig. 5.3(a)). In Fig. 5.3(c), we show the

result of applying the FBM method on the clipped signal sampled with rate $\pi/(2\omega_0)$. The method fails as saturated values in the measurements degenerate the phasor, leading to constant amplitude and depth estimation.

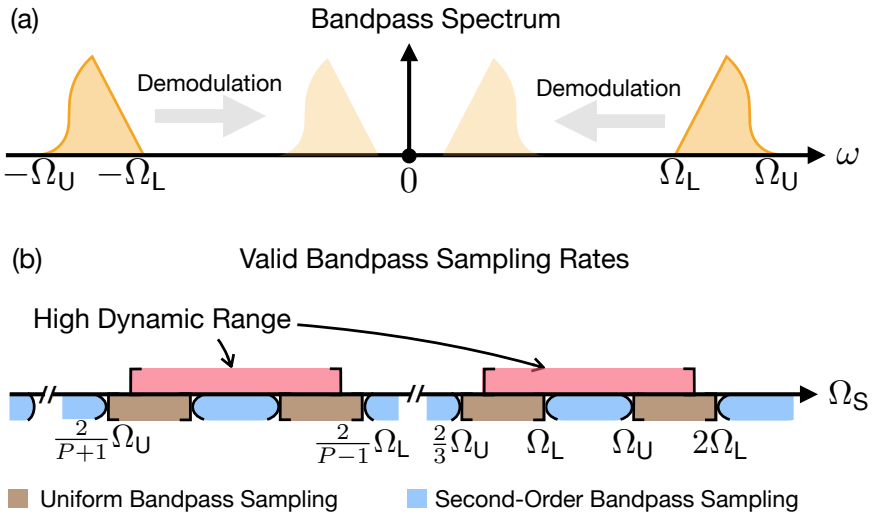


Figure 5.4: (a) The spectrum of a bandpass signal. (b) Valid sampling rates for uniform bandpass sampling (brown), second-order bandpass sampling (blue), and high-dynamic-range bandpass sampling of first- and second-order (red).

5.2 Dual-channel Unlimited Sampling for Bandpass Signals

5.2.1 Motivation and Contributions

Chapter 3 examined USF-based acquisition and reconstruction of bandpass signals, providing feasibility and mathematical guarantees for HDR bandpass sampling at sub-Nyquist rates. Nevertheless, because the approach relies on uniform sampling, the achievable sub-Nyquist rates are restricted to the intersection of the bandpass sampling theorem and USF-related constraints (see Section 2.2.3).

Periodic Nonuniform Sampling (PNS) is known to relax the "alias-free" constraint [71] in the conventional sampling case, as explained in Chapter 2.2.3, but has not been explored for modulo samples. This work presents a dual-channel architecture that integrates modulo and PNS-based sampling, and further leverages the dual-channel architecture to improve the

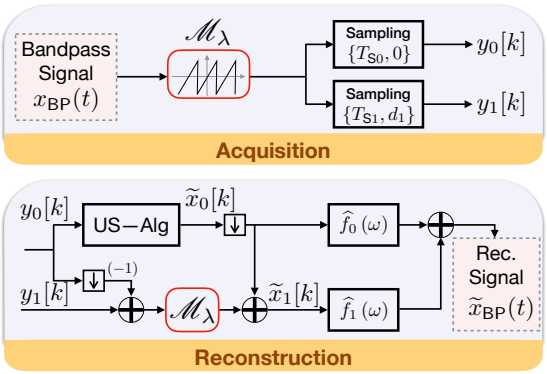


Figure 5.5: The acquisition and reconstruction pipeline of the proposed dual-channel bandpass sampling architecture.

modulo recovery conditions. The main contributions are:

1) Theoretical guarantees. Bandpass signal recovery from modulo samples compatible with second-order bandpass sampling.

2) Design principles. Provide principles for the design of a dual-rate HDR bandpass sampling system and an efficient recovery algorithm.

3) Sampling density criterion. The dual-rate design enables further sampling rate reduction, which is backed by a mathematical guarantee.

5.2.2 Second-Order Unlimited Sampling

To enhance dynamic range and resolution, the proposed architecture is composed of a $\mathscr{M}$–ADC with two sampling channels, forming the following sampling pipeline:

$$x_{\mathrm{BP}}(t) \rightarrow \boxed{\mathscr{M}_\lambda(\cdot)} \rightarrow y(t)\,|_{t=(kT_{\mathrm{S}i}+d_i)} \rightarrow y_i[k], \quad d_0 = 0, \quad k \in \mathbb{Z}.$$

The input $x_{\mathsf{BP}}(t)$ is assumed to be a real-valued bandpass signal, same as in Chapter 3. As shown in Fig. 5.5, the modulo operator $\mathscr{M}_\lambda$ folds the amplitudes of $x_{\mathsf{BP}}(t)$ into the confined range $[-\lambda, \lambda]$, and the output is sampled by the two channels at periods $T_{\mathsf{S}0}, T_{\mathsf{S}1}$ respectively. The relative inter-channel delay is d_1. Since the two channels provide uniform sampled sequences, a naive approach would be to process them independently using the existing USF methods. However, the nonuniform structure of the sampled sequence enables more efficient recovery, as we show.

Recovery Approach.

The design parameters $T_{\mathsf{S}0}, T_{\mathsf{S}1}, d_1$ shown in Fig. 5.5 provide degrees of freedom that allow reconstruction that hinges on 3 steps:

1) Recovery of $x_0[k]$ from $y_0[k]$ under a suitable choice of $T_{\mathsf{S}0}$.

2) Recovery of $x_1[k]$ from $x_0[k]$ and $y_1[k]$ under a suitable choice of $T_{\mathsf{S}1}, d_1$.

3) Recovery of $x_{\mathsf{BP}}(t)$ from the samples $x_0[k]$ and $x_1[k]$ under a suitable choice of $T_{\mathsf{S}1}, d_1$.

Step 1 Let $x_0[k] = x_{\mathsf{BP}}(t)|_{t=kT_{\mathsf{S}}}$, and denote by $\widehat{x}_{\mathsf{BP},0}(\omega)$ its discrete-time Fourier transform. The demodulation property of modulo signals explained in Chapter 3.2 implies that for $T_{\mathsf{S}} > T_{\mathsf{NS}}$, there exists a bandlimited signal $x_0(t) \neq x_{\mathsf{BP}}(t)$ which is defined via its spectrum

$$\widehat{x}_0(\omega) = \mathbb{1}_{\mathcal{D}_{\frac{\Omega_{\mathsf{S}}}{2}}}(\omega)\, \widehat{x}_{\mathsf{BP},0}(\omega), \tag{5.14}$$

where $\mathbb{1}_{\mathcal{D}}$ denotes the indicator function on the interval $\mathcal{D}_{\frac{\Omega_{\mathsf{S}}}{2}}$. Since $x_0(t)$ is a bandlimited signal, it can be recovered from its modulo samples $y_0[k]$ if Ω_{S} is sufficiently large compared to the bandwidth of $x_0(t)$ [48]. However, a unique feature of demodulated signals arises

here; if $\Omega_{\mathsf{S}} > \Omega_{\mathsf{B}}$, the support of $x_0\left(t\right)$ depends on the sampling rate Ω_{S} itself. The case of sampling rates that satisfy the bandpass sampling theorem (brown regions in Fig. 5.4) is covered in Chapter 3, including recovery guarantees for $x_{\mathsf{BP}}\left(t\right)$ from its uniform samples $x_0\left[k\right]$. Using second-order bandpass sampling (SO-BPS), a recovery guarantee for $x_0\left[k\right]$ when Ω_{S} is within the red regions in Fig. 5.4 is derived in the next lemma.

Lemma 3. *Let $x_{\mathsf{BP}}\left(t\right) \in L^2 \cap L^\infty$ be a real-valued bandpass signal with positive passband supported on $[\omega_{\mathsf{L}}, \omega_{\mathsf{U}})$. Furthermore, let $y\left[k\right] = \mathscr{M}_\lambda(x_{\mathsf{BP}}\left(kT_{\mathsf{S}}\right))$, $k \in \mathbb{Z}$ be the modulo samples of $x_{\mathsf{BP}}\left(t\right)$ at period $T_{\mathsf{S}} = 2\pi/\Omega_{\mathsf{S}}$. If there exists $M \in 2\mathbb{N}$ that satisfies*

$$\frac{4\pi e\omega_{\mathsf{U}}}{2\pi eM+1} \leq \Omega_{\mathsf{S}} \leq \frac{4\pi e\omega_{\mathsf{L}}}{2\pi eM-1}, \text{ and } \quad \frac{\omega_{\mathsf{U}}+\omega_{\mathsf{L}}}{\omega_{\mathsf{U}}-\omega_{\mathsf{L}}} \geq 2\pi eM, \tag{5.15}$$

where e denotes Euler's number, then the samples $x\left[k\right] = x_{\mathsf{BP}}\left(t\right)|_{t=kT_{\mathsf{S}}}$ can be recovered from $y\left[k\right]$ up to an additive constant of $2\lambda\mathbb{Z}$.

Proof. Let $x_{\mathrm{LP}}\left(t\right)$ denote the lowpass function defined in (5.14), and let Ω_{LP} denote its maximal frequency. Following that, $y\left[k\right]$ are the corresponding modulo samples (Chapter 3.2, [94]). First, we require that $x_{\mathrm{LP}}\left(t\right)$ is sampled above its Nyquist rate ($\Omega_{\mathrm{NQ}} > \Omega_{\mathrm{LP}}$), resulting in $\widehat{x}\left(\omega\right)|_{\omega=\Omega_{\mathsf{S}}/2} = 0$. Denote by $\mathcal{G}$ the support of the real-valued signal's spectrum, which is symmetric. Due to the symmetry, the condition translates into $M\frac{\Omega_{\mathsf{S}}}{2} \notin \mathcal{G}$ for any odd integer M. Written differently,

$$(M-1)\frac{\Omega_{\mathsf{S}}}{2} < \omega_{\mathsf{L}}, \text{ and } (M+1)\frac{\Omega_{\mathsf{S}}}{2} \geq \omega_{\mathsf{U}}, \quad \Rightarrow \quad \frac{2\omega_{\mathsf{U}}}{M+1} \leq \Omega_{\mathsf{S}} < \frac{2\omega_{\mathsf{L}}}{M-1}, \; M \in 2\mathbb{N}. \tag{5.16}$$

For Ω_{S} that satisfies (5.16), the maximum frequency Ω_{LP} is an integer shift of the passbands'

boundary frequencies $-\omega_{\mathsf{L}}$ and ω_{U} and satisfies

$$\Omega_{\mathrm{LP}} = \begin{cases} \omega_{\mathsf{U}} - \frac{M}{2}\Omega_{\mathsf{S}} & \Omega_{\mathsf{S}} \leq \frac{\omega_{\mathsf{U}}+\omega_{\mathsf{L}}}{M} \\ \frac{M}{2}\Omega_{\mathsf{S}} - \omega_{\mathsf{L}} & \Omega_{\mathsf{S}} > \frac{\omega_{\mathsf{U}}+\omega_{\mathsf{L}}}{M} \end{cases}, \tag{5.17}$$

and the condition arises when $\omega_{\mathsf{U}} - M\frac{\Omega_{\mathsf{S}}}{2} \geq -\omega_{\mathsf{L}} + M\frac{\Omega_{\mathsf{S}}}{2}$ is re-arranged into $\Omega_{\mathsf{S}} \leq \frac{\omega_{\mathsf{U}}+\omega_{\mathsf{L}}}{M}$. Based on Theorem 2.5, recovering $x\left[k\right]$ from modulo samples requires $\Omega_{\mathsf{S}} \geq 4\pi e\Omega_{\mathrm{LP}}$. Plugging the two possible values for Ω_{LP} given in (5.17), we get

$$\begin{cases} 4\pi e\left(\omega_{\mathsf{U}} - \frac{M}{2}\Omega_{\mathsf{S}}\right) \leq \Omega_{\mathsf{S}} & \Rightarrow \quad \Omega_{\mathsf{S}} \geq \frac{4\pi e\omega_{\mathsf{U}}}{2\pi eM+1} \\ 4\pi e\left(\frac{M}{2}\Omega_{\mathsf{S}} - \omega_{\mathsf{L}}\right) \leq \Omega_{\mathsf{S}} & \Rightarrow \quad \Omega_{\mathsf{S}} \leq \frac{4\pi e\omega_{\mathsf{L}}}{2\pi eM-1} \end{cases}. \tag{5.18}$$

It can be directly shown that $\frac{2\omega_{\mathsf{U}}}{P+1} \leq \frac{4\pi e\omega_{\mathsf{U}}}{2\pi eM+1}$ and $\frac{4\pi e\omega_{\mathsf{L}}}{2\pi eM-1} \leq \frac{2\omega_{\mathsf{L}}}{P-1}$. Then we write,

$$\begin{cases} \frac{4\pi e\omega_{\mathsf{U}}}{2\pi eM+1} \leq \Omega_{\mathsf{S}} < \frac{\omega_{\mathsf{U}}+\omega_{\mathsf{L}}}{2}, \\ \frac{\omega_{\mathsf{U}}+\omega_{\mathsf{L}}}{2} \leq \Omega_{\mathsf{S}} \leq \frac{4\pi e\omega_{\mathsf{L}}}{2\pi eM-1}, \end{cases} , M \leq \frac{\omega_{\mathsf{U}}+\omega_{\mathsf{L}}}{\omega_{\mathsf{U}}-\omega_{\mathsf{L}}} \tag{5.19}$$

where the RHS ensures that $\frac{\omega_{\mathsf{U}}+\omega_{\mathsf{L}}}{2} \leq \frac{2\omega_{\mathsf{L}}}{P-1}$ and $\frac{2\omega_{\mathsf{U}}}{M+1} \leq \frac{\omega_{\mathsf{U}}+\omega_{\mathsf{L}}}{2}$ so Ω_{S} satisfies (5.16). Lastly,

$$\frac{4\pi e\omega_{\mathsf{U}}}{2\pi eM+1} \leq \frac{4\pi e\omega_{\mathsf{L}}}{2\pi eM-1} \quad \Rightarrow \quad 2\pi eM \leq \frac{\omega_{\mathsf{U}}+\omega_{\mathsf{L}}}{\omega_{\mathsf{U}}-\omega_{\mathsf{L}}}, \tag{5.20}$$

and the two parts of (5.19) can be unified to get (5.15). Under the condition on Ω_{S}, the samples $x_{\mathrm{LP}}\left[k\right]$ can be recovered from the modulo measurements using Algorithm 1. ■

Fig. 5.4 illustrates the relation between the intervals in (5.15), represented by the red re-

Algorithm 7: Second-order Bandpass Recovery via Unlimited Sampling

Input: $y_0[k]$, $y_1[k]$, λ,$\alpha = ||x_{\mathsf{BP}}||_\infty$, ω_{L}, and ω_{U}.
Result: Bandpass function, $\widetilde{x}_{\mathsf{BP}}(t)$.

1) Compute the N^{th} order finite-differences $\left(\Delta^N y_0\right)[k]$, where the order is computed from $N = \left\lceil \frac{\log\lambda - \log\alpha}{\log(T_{\mathsf{S}_0}\Omega e)} \right\rceil$.

2) Compute $\left(\Delta^N r_0\right)[k] = \left(\mathscr{M}_\lambda(\Delta^N y_0) - \left(\Delta^N y_0\right)\right)[k]$.
Set $s_{(0)}[k] = \left(\Delta^N r_0\right)[k]$.

3) For $n = 0 : N-2$

   (i) $s_{(n+1)}[k] = \mathsf{S}\left(s_{(n)}\right)[k]$, $\mathsf{S} : \{s[k]\}_{k\in\mathbb{Z}^+} \to \sum_{m=1}^{k} s[m]$.

   (ii) $s_{(n+1)}[k] = 2\lambda \left\lceil \frac{\lfloor s_{(n+1)}/\lambda \rfloor}{2} \right\rceil$ (rounding to $2\lambda\mathbb{Z}$).

   (iii) Compute $\kappa_{(n)} = \left\lfloor \frac{\mathsf{S}^2(\Delta^n r)[1] - \mathsf{S}^2(\Delta^n r)[\frac{6\alpha}{\lambda}+1]}{12\alpha} + \frac{1}{2} \right\rfloor$.

   (iv) $s_{(n+1)}[k] = s_{(n+1)}[k] + 2\kappa_{(n)}$.

   end

4) Compute $\widetilde{x}_0[k] = \mathsf{S}\left(s_{(N-1)}\right)[k] + y_0[k]$.

5) Compute $\widetilde{x}_1 = \widetilde{x}_0\left[\frac{T_{\mathsf{S}_1}}{T_{\mathsf{S}_0}}k\right] + \mathscr{M}_\lambda(y_1[k] - y_0\left[\frac{T_{\mathsf{S}_1}}{T_{\mathsf{S}_0}}k\right])$.

6) Solve (2.9) to get the filters $\widehat{f_0}(\omega)$, $\widehat{f_1}(\omega)$.

7) $\widehat{\widetilde{g}}_{\mathsf{BP}}(t) = (f_0 * \widetilde{x}_0)(t) + (f_1 * \widetilde{x}_1)(t) + 2m\lambda, m \in \mathbb{Z}$.

gions, and the valid intervals for uniform HDR bandpass sampling according to Theorem 3.1, represented by the intersection between red and brown regions. To get $x_0[k]$, the result of Lemma 3 can be used directly.

Step 2 In the next step of the reconstruction pipeline, the bandlimited samples of the second channel $x_1[k]$ are recovered from their modulo samples. While this can be done under the

conditions of Lemma 3, an alternative option is to achieve this by designing the delay interval d_1 based on the next lemma. This significantly relaxes the constraint on the sampling rate of the second channel.

Lemma 4. *Let $x_{\mathsf{BP}}(t) \in L^2 \cap L^\infty$ be an ω_{U}-bandlimited signal, let $x_0[k] = x_{\mathsf{BP}}(t)|_{t=kT_{\mathsf{S}}}$, $k \in \mathbb{Z}$ be its samples at period $T_{\mathsf{S}} > 0$ and $y_1[k] = \mathscr{M}_\lambda(x_{\mathsf{BP}}(t))|_{t=kT_{\mathsf{S}}+d_1}$ be its modulo samples. If,*

$$d_1 \leq \frac{\lambda}{\omega_{\mathsf{U}} e \|x_{\mathsf{BP}}\|_\infty} \leq \frac{\pi}{\omega_{\mathsf{U}}}, \quad \frac{T_{\mathsf{S}}}{d_1} \in \mathbb{N}, \tag{5.21}$$

then the sequence $x_1[k] = x_{\mathsf{BP}}(t)|_{t=kT_{\mathsf{S}}+d_1}$ can be recovered from $y_1[k]$.

Proof. Let $\overline{x}[k] \overset{\text{def}}{=} x_{\mathsf{BP}}(t)|_{t=kd_1}$, $k \in \mathbb{Z}$, that is the sequence of samples of $x_{\mathsf{BP}}(t)$ at instances $t = kd_1$. Let $\Delta\overline{x}$ denote its first-order finite differences such that $\Delta\overline{x}[k] = \overline{x}[k+1] - \overline{x}[k]$. Since $x_{\mathsf{BP}}(t)$ is ω_{U}-bandlimited and $d_1 \leq \pi/\omega_{\mathsf{U}}$, its amplitudes are upper bounded based on Lemma 2 in [48]

$$\|\Delta\overline{x}\|_\infty \leq d_1 \omega_{\mathsf{U}} e \|x_{\mathsf{BP}}\|_\infty \overset{(5.21)}{\leq} \lambda. \tag{5.22}$$

The sequence $(x_1 - x_0)[k] = \overline{x}\left[k\frac{T_{\mathsf{S}}}{d_1} + 1\right] - \overline{x}\left[k\frac{T_{\mathsf{S}}}{d_1}\right]$ is a subset of $\overline{x}[k]$ and from (5.22), we have that $\|x_1 - x_0\|_\infty \leq \lambda$. Using modular arithmetic (Prop. 2 in [48]) we can write

$$\mathscr{M}_\lambda(y_1 - \mathscr{M}_\lambda(x_0)) = \mathscr{M}_\lambda(x_1 - x_0) \overset{(5.22)}{=} x_1 - x_0, \tag{5.23}$$

Then, computing $x_1[k] = x_0[k] + (x_1 - x_0)[k]$ yields the result. ∎

Lemma 4 indicates that the samples of a bandlimited signal can be recovered from its modulo measurements and its samples on a shifted grid, whenever the shift is sufficiently small.

Importantly, the sampling period can be any $T_{\mathsf{S}} \in d_1\mathbb{N}$ for which $T_{\mathsf{S}} \leq \frac{2\pi}{\omega_{\mathsf{U}}-\omega_{\mathsf{L}}}$.

To harness this result into our architecture, the parameters are chosen as follows. For $T_{\mathsf{S}0}$ that satisfies (5.15), we choose $T_{\mathsf{S}1}$ that satisfies $T_{\mathsf{S}1}/T_{\mathsf{S}0} \in \mathbb{N}$ and d_1 that satisfies both (5.21) and $T_{\mathsf{S}1}/d_1 \in \mathbb{Z}$. Then, $y_0[k], y_1[k]$ are obtained such that the conditions of Lemma 4 are satisfied with $x_0\left[\frac{T_{\mathsf{S}1}}{T_{\mathsf{S}0}}k\right]$ and $y_1[k]$. Finally, $\widetilde{x}_1 = \widetilde{x}_0\left[\frac{T_{\mathsf{S}1}}{T_{\mathsf{S}0}}k\right] + \mathscr{M}_\lambda(y_1[k] - y_0\left[\frac{T_{\mathsf{S}1}}{T_{\mathsf{S}0}}k\right])$.

Step 3 After $x_0[k]$ and $x_1[k]$ have been recovered, the bandpass signal $x_{\mathsf{BP}}(t)$ is reconstructed by following the SO-BPS procedure described in Section 2.2.3. The main result is summarised in the next theorem, which unifies the system design requirements that fulfil the 3 recovery steps.

Theorem 5.2 [Unlimited Second-Order Sampling of Bandpass Signals]

Let $x_{\mathsf{BP}}(t) \in L^2 \cap L^\infty$ be a real-valued bandpass signal with passband supported on $[\omega_{\mathsf{L}}, \omega_{\mathsf{U}})$. Furthermore, let its modulo samples at periods $T_{\mathsf{S}0}, T_{\mathsf{S}1} \leq 2\pi/(\omega_{\mathsf{U}} - \omega_{\mathsf{L}})$ be $y_0[k] = \mathscr{M}_\lambda(x_{\mathsf{BP}}(t))|_{t=kT_{\mathsf{S}0}}$ and $y_1[k] = \mathscr{M}_\lambda(x_{\mathsf{BP}}(t))|_{t=kT_{\mathsf{S}1}+d_1}$, respectively, and a relative delay $d_1 > 0$. If there exist $M \in 2\mathbb{N}$, $Q_1, Q_2 \in \mathbb{N}$ such that,

1. $\frac{\omega_{\mathsf{U}}+\omega_{\mathsf{L}}}{\omega_{\mathsf{U}}-\omega_{\mathsf{L}}} \geq 2\pi eM$ *and* $\frac{2\pi eM-1}{2e\omega_{\mathsf{L}}} \leq T_{\mathsf{S}0} \leq \frac{2\pi eM+1}{2e\omega_{\mathsf{U}}}$.
2. $T_{\mathsf{S}1} = Q_1 T_{\mathsf{S}0} = Q_2 d_1$, *and* $d_1 \leq \frac{\lambda}{\omega_{\mathsf{U}} e \|x_{\mathsf{BP}}\|_\infty}$.
3. $\left\lfloor \frac{2\omega_{\mathsf{L}}}{\Omega_{\mathsf{S}}} \right\rfloor \frac{d_1}{T_{\mathsf{S}1}} \notin \mathbb{N}$ *and* $\left(\left\lfloor \frac{2\omega_{\mathsf{L}}}{\Omega_{\mathsf{S}}} \right\rfloor + 1\right) \frac{d_1}{T_{\mathsf{S}1}} \notin \mathbb{N}$.

Then $x_{\mathsf{BP}}(t)$ can be recovered up to an additive constant of $2\lambda\mathbb{Z}$.

Proof. As the conditions satisfy Lemma 3, Lemma 4 and the SO-BPS recovery conditions, by following the steps described in this section, the result can be obtained. ■

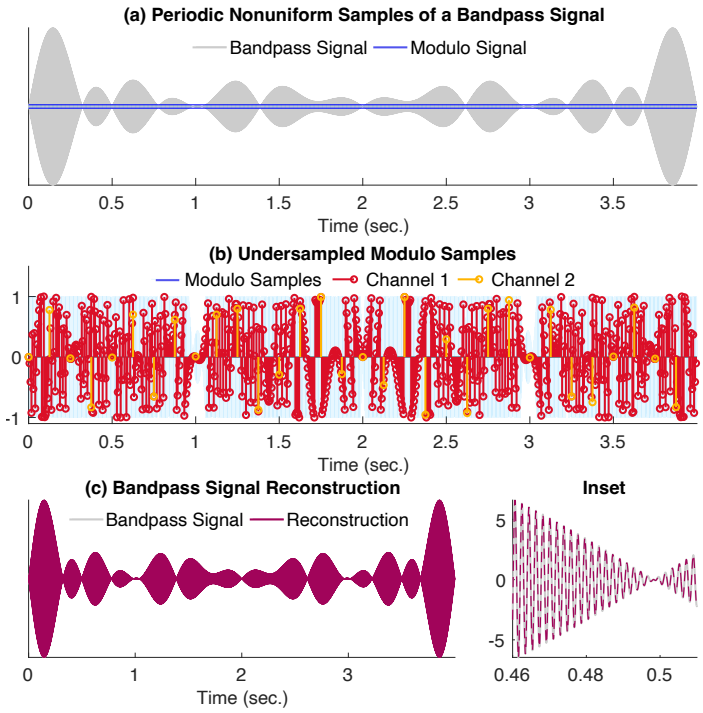


Figure 5.6: Reconstruction of a bandpass signal with modulation frequency $\omega_0 = 1054\pi(\mathrm{rad/sec})$, and maximum amplitude $\alpha = 46.33$ from its modulo samples with $\lambda = 1$. The sampling rates are $\Omega_{\mathsf{S}0} = 352\pi(\mathrm{rad/sec})$ and $\Omega_{\mathsf{S}1} = 16\pi(\mathrm{rad/sec})$ for the first and second channels, respectively. The relative delay is $d_1 = 7.57 \times 10^{-6}(\mathrm{sec})$. The error between the ground-truth bandpass samples and those recovered using Algorithm 7 is MSE $= 3.45 \times 10^{-21}$.

Numerical Experiment.

Experimental Protocol. To test our framework, bandpass signals are generated following the model in Chapter 3 and [68], which is : $x_{\mathsf{BP}}(t) = \varphi(t)\cos(\omega_0 t)$, where $\omega_0 = \frac{\omega_{\mathsf{U}}+\omega_{\mathsf{L}}}{2}$ is a modulation frequency, and $\varphi(t)$ is a lowpass signal with bandwidth $\frac{\omega_{\mathsf{U}}-\omega_{\mathsf{L}}}{2} = 5\pi(\mathrm{rad/s})$. We generate 60 random realizations of $\varphi(t)$, modulated at uniform frequency increments of $0.5\pi(\mathrm{rad/sec})$, within $\left[\frac{4\pi e\omega_{\mathsf{U}}}{2\pi eM+1}, \frac{4\pi e\omega_{\mathsf{L}}}{2\pi eM-1}\right]$ with $M = 2, M = 4$, and $M = 6$. Following Fig. 5.5, modulo samples of $y_0[k]$ and $y_1[k]$ with threshold $\lambda = 1$ are obtained. The sampling rates are $\Omega_{\mathsf{S}0} = 352\pi(\mathrm{rad/s}), \Omega_{\mathsf{S}1} = 16\pi(\mathrm{rad/s})$ and the delay is $d_1 =$

$7.5758 \times 10^{-6}(\text{sec})$, that satisfy Theorem 5.2 with integers $Q_1 = 4, Q_2 = 3 \times 10^3$ and the corresponding M. Reconstruction of $x_0[k], x_1[k]$ is performed using Algorithm 7, and evaluated using the MSE, where the additive constant of $2\lambda\mathbb{Z}$ is estimated from the ground-truth samples.

Performance Evaluation. The recovery of $x_0[k]$ is performed up to the machine precision, and this result is asserted across 3 intervals of (5.15), which further validates the theoretical bound. Then, $x_1[k]$ is recovered up to machine precision as well, showing that for the second channel, samples can be taken just above the Nyquist rate of the demodulated signal, since $\Omega_{\mathsf{S}1} = 16\pi > 10\pi = \omega_{\mathsf{U}} - \omega_{\mathsf{L}}$. Lastly, for the reconstruction of the bandpass signal, an average MSE of 6.18×10^{-21} is observed, for inputs with a maximal average amplitude of $\approx 34\lambda$. The nonexact recovery occurs due to finite precision arithmetic, and the results demonstrate the potential of the proposed framework for HDR sampling of bandpass signals. The results for one of the tested realisations are shown in Fig. 5.6.

5.2.3 Conclusion

In this chapter, the Unlimited Sensing Framework (USF) is applied to two distinct problems: high dynamic range time-of-flight (ToF) imaging and bandpass sampling. In the first part, modulo acquisition is shown to enable robust recovery of amplitude and phase parameters in ToF systems, with theoretical guarantees supported by numerical experiments. This setting is inherently parametric, therefore a natural extension would be to formulate the noisy recovery problem statistically, for instance through a maximum-likelihood estimator implemented via a low-dimensional search over the unknown amplitude and phase parameters. Such a formulation would also enable a reliability analysis based on Cramér–Rao lower bounds, as well

as systematic comparisons between the proposed estimator and statistically optimal performance limits.

In the second part, a dual-channel architecture based on Periodic Nonuniform Sampling was developed to relax the aliasing constraints of uniform USF sampling, enabling sub-Nyquist recovery of bandpass signals. Both theoretical derivations and numerical experiments confirmed the feasibility of these approaches.

Despite targeting different signal models, both studies illustrate a unifying principle: by exploiting the Fourier structure of the signals and integrating hardware-inspired architectures with practical recovery algorithms, the Unlimited Sensing Framework can reconcile dynamic range and sampling-rate limitations.

Together, these results highlight the versatility of USF across modalities and signal classes, and they lay the foundation for more general acquisition frameworks. In particular, they motivate the extension to multiband signals explored in Chapter 4, where USF-based sampling is examined in both single- and multi-channel architectures, leveraging both parametric and non-parametric models.

6

Conclusion

6.1 Motivation and Research Problem

The digitization of analog signals has long been underpinned by Shannon's sampling theory, which guarantees perfect reconstruction of bandlimited signals from uniform samples. This principle has shaped sensing and communication systems for decades and remains foundational to modern digital technology.

In practice, however, analog-to-digital converters (ADCs) deviate from the ideal assumptions of classical sampling theory. Amplitude quantization introduces clipping and quantization noise, both of which distort recorded samples. This gap has become increasingly restrictive in modern applications that demand both high dynamic range and fine digital

resolution—capabilities that conventional ADCs struggle to achieve simultaneously due to inherent trade-offs.

The Unlimited Sensing Framework (USF) offers a promising route to overcoming these hardware limitations. It effectively boosts quantization resolution under a fixed bit budget, enabling high-dynamic-range acquisition with low-resolution ADCs. Over the past few years, the practical feasibility of the USF has been demonstrated through several hardware implementations, validating its theoretical principles and showing its potential in high-dynamic-range imaging and sensing applications.

However, until now, USF has been studied primarily in the context of bandlimited signals. This focus overlooks the important signal class of multiband signals found in communications, radar, sonar, and hyperspectral imaging. Treating such signals as bandlimited to their full spectral span imposes prohibitively high sampling rates and hinders the direct application of USF ideas that were developed for bandlimited settings. This highlighted the need for new theory and methods that exploit the inherent Fourier structure of multiband signals to enable their recovery at lower sampling rates. In this context, USF's ability to improve effective digital resolution without increasing the bit budget is especially attractive; sub-Nyquist sampling sacrifices the possibility of oversampling-based noise reduction, and thus demands higher resolution measurements.

This thesis addresses that gap: It investigates how the USF can be extended to sub-Nyquist sampling of multiband signals and develops the theoretical, algorithmic, and practical foundations needed to do so.

Theory. On the theoretical front, this thesis provides the first foundations for applying the USF to Fourier-structured signals, including:

1. Formal recovery guarantees for single-tone and bandpass signals, representative of real-world sensing modalities such as time-of-flight and radar.

2. Recovery guarantees for multiband signals, based on leveraging their structured Fourier support.

3. Theoretical analysis of multi-channel USF architectures for resolving aliasing both in amplitude and frequency domains under sub-Nyquist sampling rates.

Algorithms. On the algorithmic front, this thesis develops practical recovery methods for applying the USF to Fourier-structured signals, including:

1. A constructive algorithm that exploits known structured Fourier support to enable reconstruction of multiband signals from sub-Nyquist modulo samples.

2. USF-based bandpass sampling algorithms, tailored to different modulo folding architectures, explain and accommodate device-level behaviours observed in practice.

3. An end-to-end procedure that recovers 3D depth directly from finitely many modulo ToF measurements, without explicit inversion or unfolding. This enables HDR operation under severe saturation.

Practice. On the practical front, this thesis validates the USF under realistic conditions through prototype hardware and end-to-end system experiments, including:

1. Prototype measurements that test and verify the theoretical modelling of demodulation of modulo signals across different folding architectures.

2. End-to-end experiments confirming recovery for bandpass and multiband signals based on proposed algorithms.

Taken together, the results establish a coherent pathway from theory to hardware for applying the USF to Fourier-structured signals. The thesis shows that modulo-enabled USF can turn structured spectral priors into tangible sampling and reconstruction gains, closing the gap between theory, algorithms, and practice.

6.3 Limitations and Scope

This work targets Fourier-structured signals—single-tone, bandpass, and multiband—where spectral support is known at acquisition (non-blind) or before recovery (semi-blind). The fully blind setting, in which the support is unknown, is not covered by existing results. The main challenge is that the separation between smooth and integer signal components, which is at the core of algorithmic approaches, cannot be realised directly through on spectral separation.

The modulo architectures considered are pointwise sampling schemes. Although USF has shown promise with Sigma–Delta converters, such integrations are outside the scope of this thesis and are not leveraged here.

Multi-channel guarantees and algorithms assume calibrated hardware. In uncalibrated setups, effects such as timing jitter and gain/phase mismatch can severely affect the redundancy principles these methods rely on, posing a significant challenge for direct deployment.

6.4 Open Problems and Future Work

We conclude by highlighting open questions and future directions that are both technically pressing and practically consequential.

1. Fully blind recovery. In many multiband sampling applications (e.g., spectrum sensing), the carrier frequencies are unknown a priori. It is therefore necessary to develop theory, algorithms, and guarantees that remove prior knowledge of the spectral support. The first attempt in this direction was already presented in [118], and future results can lead to further utilisation of USF-based multiband sampling.

2. Non-bandlimited Fourier-structured signals. So far, only bandlimited models of Fourier-structured signals have been considered. The framework could be broadened to other Fourier-structured classes, such as modulated splines, chirps/polynomial-phase signals, and finite-rate-of-innovation processes. Such advances could impact radar/sonar, biomedical imaging (ultrasound, magnetic resonance imaging), wireless communications, and LiDAR.

3. High-dimensional extensions. Multiband sampling has higher-dimensional formulations [119], and modern computational photography already exploits aliasing to improve reconstructions [120]. Extending the multiband-USF ideas to higher dimensions could deliver simultaneous HDR and high effective resolution with low-bit readout, while maintaining stable performance under sensor non-idealities. Promising targets include burst imaging, and active/depth sensing—e.g., ToF and FMCW LiDAR in the presence of motion and multipath. Key challenges include the derivation of the

theory for multidimensional unlimited sampling [121], stable and scalable reconstruction algorithms, and realisation of multidimensional modulo front-ends.

A

Proof of the Identity Used in Lemma 1 of Chapter 4

Let $\Omega_{\mathsf{C}}^{[p]} \stackrel{\text{def}}{=} \Omega_{\mathsf{C}} \setminus \{\omega_p\}$, and define $\widetilde{\varphi}_p[k] \stackrel{\text{def}}{=} \varphi_p[k]\, e^{-\jmath\omega_p k T_{\mathsf{S}}}$. For the filter $\Psi_{\Omega_{\mathsf{C}}}$ defined in (4.5), prove by induction the identity

$$\left(\Psi_{\Omega_{\mathsf{C}}}^{N} * \widetilde{\varphi}_p\right)[k] = \left(\Psi_{\Omega_{\mathsf{C}}^{[p]}}^{N} * \left[\left(\Delta^{N} * \varphi_p\right)[m]\, e^{-\jmath\omega_p(m)T_{\mathsf{S}}}\right]\right)[k]\,. \tag{A.1}$$

Proof. **Case $N = 1$:** The frequency response of $\Psi_{\Omega_{\mathsf{C}}}$ is $\widehat{\Psi_{\Omega_{\mathsf{C}}}}(\omega) = \prod_{p=0}^{P-1}\left(1 - e^{-\jmath(\omega-\omega_p)T_{\mathsf{S}}}\right)$. The filter coefficients are:

$$\Psi_{\Omega_{\mathsf{C}}}[k] = (-1)^k a_{\Omega_{\mathsf{C}}}^{k}, \quad a_{\Omega_{\mathsf{C}}}^{k} \stackrel{\text{def}}{=} \sum_{\substack{\mathcal{S}\subseteq\Omega_{\mathsf{C}} \\ |\mathcal{S}|=k}} \prod_{\omega\in\mathcal{S}} e^{-\jmath\omega T_{\mathsf{S}}}, \quad \left|a_{\Omega_{\mathsf{C}}}^{k}\right| \leq \binom{\#\Omega_{\mathsf{C}}}{k}, \tag{A.2}$$

where $a^k_{\Omega_\mathsf{C}}$ denotes the elementary symmetric polynomial of degree k in P frequencies Ω_C, following from Newton's identities. We also use the recursive definition $a^k_{\Omega_\mathsf{C}} = a^{k-1}_{\Omega^{[p]}_\mathsf{C}} e^{-\jmath\omega_p T_\mathsf{S}} + a^k_{\Omega^{[p]}_\mathsf{C}}$. Computing the LHS of (A.1) with Ψ_{Ω_C}:

$$
\begin{aligned}
\left(\Psi_{\Omega_\mathsf{C}} * \widetilde{\varphi}_p\right)[k] &= \sum_{n=0}^{P} (-1)^n \left(a^{n-1}_{\Omega^{[p]}_\mathsf{C}} e^{-\jmath\omega_p T_\mathsf{S}} + a^n_{\Omega^{[p]}_\mathsf{C}} \right) \varphi_p[k-n]\, e^{\jmath\omega_p (k-n) T_\mathsf{S}} \\
&\overset{\widetilde{n}=n-1}{=} e^{-\jmath\omega_p k T_\mathsf{S}} \left(\sum_{\widetilde{n}=-1}^{P-1} (-1)^{\widetilde{n}+1} a^{\widetilde{n}}_{\Omega^{[p]}_\mathsf{C}} e^{\jmath\omega_p \widetilde{n} T_\mathsf{S}} \varphi_p[k-\widetilde{n}-1] + \sum_{n=0}^{P} (-1)^n a^n_{\Omega^{[p]}_\mathsf{C}} e^{\jmath\omega_p n T_\mathsf{S}} \varphi_p[k-n] \right) \\
&= e^{-\jmath\omega_p k T_\mathsf{S}} \left(0 + \sum_{n=0}^{P-1} (-1)^n a^n_{\Omega^{[p]}_\mathsf{C}} e^{\jmath\omega_p n T_\mathsf{S}} \left(\varphi_p[k-n] - \varphi_p[k-n-1]\right) + 0 \right) \\
&= e^{-\jmath\omega_p k T_\mathsf{S}} \sum_{n=0}^{P-1} (-1)^n a^n_{\Omega^{[p]}_\mathsf{C}} e^{\jmath\omega_p n T_\mathsf{S}} (\Delta * \varphi_p)[k-n]\,.
\end{aligned}
$$

Inductive Step: Assume the identity (A.1) holds for some N.

Prove for $N+1$: From the definition $\left(\Psi^{N+1}_{\Omega_\mathsf{C}} * \widetilde{\varphi}_p\right)[k] = \left(\Psi_{\Omega_\mathsf{C}} * \Psi^N_{\Omega_\mathsf{C}} * \widetilde{\varphi}_p\right)[k]$, we compute:

$$
\begin{aligned}
\left(\Psi^{N+1}_{\Omega_\mathsf{C}} * \widetilde{\varphi}_p\right)[k] &= \sum_{n=0}^{P} (-1)^n \left(a^{n-1}_{\Omega^{[p]}_\mathsf{C}} e^{-\jmath\omega_p T_\mathsf{S}} + a^n_{\Omega^{[p]}_\mathsf{C}} \right) \left(\Psi^N_{\Omega_\mathsf{C}} * \widetilde{\varphi}_p\right)[k-n] \qquad \text{(A.3)} \\
&\overset{\widetilde{n}=n-1}{=} \sum_{\widetilde{n}=-1}^{P-1} (-1)^{\widetilde{n}+1} a^{\widetilde{n}}_{\Omega^{[p]}_\mathsf{C}} e^{-\jmath\omega_p T_\mathsf{S}} \left(\Psi^N_{\Omega_\mathsf{C}} * \widetilde{\varphi}_p\right)[k-\widetilde{n}-1] \\
&\quad + \sum_{n=0}^{P} (-1)^n a^n_{\Omega^{[p]}_\mathsf{C}} \left(\Psi^N_{\Omega_\mathsf{C}} * \widetilde{\varphi}_p\right)[k-n] \\
&= 0 + \sum_{n=0}^{P-1} (-1)^n a^n_{\Omega^{[p]}_\mathsf{C}} \left(\left(\Psi^N_{\Omega_\mathsf{C}} * \widetilde{\varphi}_p\right)[k-n] - \left(\Psi^N_{\Omega_\mathsf{C}} * \widetilde{\varphi}_p\right)[k-n-1] e^{-\jmath\omega_p T_\mathsf{S}} \right) + 0
\end{aligned}
$$

For the N^{th} order filter $\Psi^N_{\Omega_\mathsf{C}}$,

$$\Psi^N_{\Omega_\mathsf{C}}[k] = (-1)^k \sum_{\mathbf{v}\in\mathcal{V}(N,k)} \prod_{i=0}^{N-1} a^{v_i}_{\Omega_\mathsf{C}}, \quad \mathcal{V}(N,k) \stackrel{\text{def}}{=} \left\{ \mathbf{v}\in\mathbb{N}^N \mid \sum_{i=1}^{N} \mathbf{v}_i = k \right\}. \tag{A.4}$$

where the set $\mathcal{V}(N,k)$ consists of all length-N vectors of non-negative integers whose elements sum to k. Using the induction assumption, replacing $\Psi^N_{\Omega_\mathsf{C}}$ according to (A.4) and computing the convolution,

$$\begin{aligned} &(\Psi^N_{\Omega_\mathsf{C}} * \widetilde{\varphi}_p)[k-n] - (\Psi^N_{\Omega_\mathsf{C}} * \widetilde{\varphi}_p)[k-n-1]e^{-\jmath\omega_p T_\mathsf{S}} \\ &= e^{-\jmath\omega_p(k-n)T_\mathsf{S}} \sum_{l=0}^{N(P-1)} (-1)^l \sum_{\mathbf{v}\in\mathcal{V}(N,l)} \prod_{i=0}^{N-1} a^{v_i}_{\Omega^{[p]}_\mathsf{C}} e^{-\jmath\omega_p l T_\mathsf{S}} (\Delta^{N+1} * \varphi_p)[k-n-l]. \end{aligned} \tag{A.5}$$

Substituting (A.5) into (A.3) and re-arranging,

$$\begin{aligned} &\left(\Psi^{N+1}_{\Omega_\mathsf{C}} * \widetilde{\varphi}_p\right)[k] = \\ &\sum_{n=0}^{P-1} (-1)^n a^n_{\Omega^{[p]}_\mathsf{C}} e^{-\jmath\omega_p(k-n)T_\mathsf{S}} \sum_{l=0}^{N(P-1)} (-1)^l \sum_{\mathbf{v}\in\mathcal{V}(N,l)} \prod_{i=0}^{N-1} a^{v_i}_{\Omega^{[p]}_\mathsf{C}} e^{\jmath\omega_p l T_\mathsf{S}} (\Delta^{N+1} * \varphi_p)[k-n-l] \\ &= \sum_{n=0}^{(N+1)(P-1)} (-1)^n \sum_{\mathbf{v}\in\mathcal{V}(N+1,n)} \prod_{i=0}^{N-1} a^{v_i}_{\Omega^{[p]}_\mathsf{C}} (\Delta^{N+1} * \varphi_p)[k-n] e^{-\jmath\omega_p(k-n)T_\mathsf{S}} \\ &= \left(\Psi^{N+1}_{\Omega^{[p]}_\mathsf{C}} * \left[\left(\Delta^{N+1} * \varphi_p\right)[m] e^{-\jmath\omega_p(m)T_\mathsf{S}} \right] \right)[k]. \end{aligned}$$

Thus, the identity (A.1) holds for $N+1$, which completes the proof. ■

References

[1] C. Shannon, "Communication in the presence of noise," *Proceedings of the IRE*, vol. 37, no. 1, pp. 10–21, Jan. 1949.

[2] W. Brinkman, D. Haggan, and W. Troutman, "A history of the invention of the transistor and where it will lead us," *IEEE Journal of Solid-State Circuits*, vol. 32, no. 12, pp. 1858–1865, 1997.

[3] J. Kilby, "Invention of the integrated circuit," *IEEE Transactions on Electron Devices*, vol. 23, no. 7, pp. 648–654, Jul. 1976.

[4] M. Vetterli, P. Marziliano, and T. Blu, "Sampling signals with finite rate of innovation," *IEEE Transactions on Signal Processing*, vol. 50, no. 6, pp. 1417–1428, Jun. 2002.

[5] D. Donoho, "Compressed sensing," *IEEE Transactions on Information Theory*, vol. 52, no. 4, pp. 1289–1306, Apr. 2006.

[6] A. Kohlenberg, "Exact interpolation of band-limited functions," *Journal of Applied Physics*, vol. 24, no. 12, pp. 1432–1436, Dec. 1953.

[7] H. J. Landau, "Necessary density conditions for sampling and interpolation of certain entire functions," *Acta Mathematica*, vol. 117, no. 0, pp. 37–52, 1967.

[8] J. L. Brown, "On uniform sampling of amplitude modulated signals," *IEEE Trans. Aerosp. Electron. Syst.*, vol. AES-19, no. 4, pp. 633–635, Jul. 1983.

[9] M. Mishali and Y. Eldar, "Sub-Nyquist sampling," *IEEE Signal Process. Mag.*, vol. 28, no. 6, pp. 98–124, Nov. 2011.

[10] Y. C. Eldar and T. Michaeli, "Beyond bandlimited sampling," *IEEE Signal Processing Magazine*, vol. 26, no. 3, pp. 48–68, May 2009.

[11] A. Papoulis, "A new algorithm in spectral analysis and band-limited extrapolation," *IEEE Transactions on Circuits and Systems*, vol. 22, no. 9, pp. 735–742, Sep. 1975.

[12] A. Janssen, R. Veldhuis, and L. Vries, "Adaptive interpolation of discrete-time signals that can be modeled as autoregressive processes," *IEEE Transactions on Acoustics, Speech, and Signal Processing*, vol. 34, no. 2, pp. 317–330, Apr. 1986.

[13] J. Abel and J. Smith, "Restoring a clipped signal," in *IEEE Intl. Conf. on Acoustics, Speech and Signal Processing (ICASSP)*. IEEE, 1991.

[14] W. R. Bennett, "Spectra of quantized signals," *Bell System Technical Journal*, vol. 27, no. 3, pp. 446–472, Jul. 1948.

[15] L. Schuchman, "Dither signals and their effect on quantization noise," *IEEE Transactions on Communications*, vol. 12, no. 4, pp. 162–165, Dec. 1964.

[16] R. Gray and T. Stockham, "Dithered quantizers," *IEEE Trans. Inf. Theory*, vol. 39, no. 3, pp. 805–812, May 1993.

[17] F. Sun, J. Singh, and U. Madhow, "Automatic gain control for ADC-limited communication," in *2010 IEEE Global Telecommunications Conference GLOBECOM 2010*. IEEE, Dec. 2010.

[18] R. T. Yazicigil, T. Haque, P. R. Kinget, and J. Wright, "Taking compressive sensing to the hardware level: Breaking fundamental radio-frequency hardware performance tradeoffs," *IEEE Signal Process. Mag.*, vol. 36, no. 2, pp. 81–100, Mar. 2019.

[19] A. Bhandari, F. Krahmer, and R. Raskar, "On unlimited sampling," in *Intl. Conf. on Sampling Theory and Applications (SampTA)*, Jul. 2017. [Online]. Available: https://doi.org/10.1109/sampta.2017.8024471

[20] A. Bhandari, M. H. Conde, and O. Loffeld, "One-bit time-resolved imaging," *IEEE Trans. Pattern Anal. Mach. Intell.*, vol. 42, no. 7, pp. 1630–1641, Jul. 2020.

[21] S. Mann and R. W. Picard, "Being 'undigital' with digital cameras: extending dynamic range by combining differently exposed pictures," M.I.T Media Lab Perceptual Computing Section, Tech. Rep., 1994.

[22] V. Blahnik and O. Schindelbeck, "Smartphone imaging technology and its applications," *Advanced Optical Technologies*, vol. 10, no. 3, pp. 145–232, Jun. 2021.

[23] A. Bhandari, F. Krahmer, and T. Poskitt, "Unlimited sampling from theory to practice: Fourier-Prony recovery and prototype ADC," *IEEE Trans. Signal Process.*, vol. 70, pp. 1131–1141, Sep. 2021.

[24] Y. Zhu and A. Bhandari, "Unleashing dynamic range and resolution in unlimited sensing framework via novel hardware," in *IEEE SENSORS*. IEEE, Oct. 2024, pp. 1–4.

[25] D. Florescu, F. Krahmer, and A. Bhandari, "The surprising benefits of hysteresis in unlimited sampling: Theory, algorithms and experiments," *IEEE Trans. Signal Process.*, vol. 70, pp. 616–630, Jan. 2022.

[26] R. Guo and A. Bhandari, "Iter-sis: Robust unlimited sampling via iterative signal sieving," in *IEEE Intl. Conf. on Acoustics, Speech and Signal Processing (ICASSP)*. IEEE, Jun. 2023, pp. 1–5.

[27] M. Beckmann, A. Bhandari, and F. Krahmer, "The modulo Radon transform: Theory, algorithms, and applications," *SIAM Journal on Imaging Sciences*, vol. 15, no. 2, pp. 455–490, Apr. 2022.

[28] M. Beckmann, A. Bhandari, and M. Iske, "Fourier-domain inversion for the modulo radon transform," *IEEE Trans. Comput. Imaging*, vol. 10, pp. 653–665, 2024.

[29] T. Feuillen, B. M. Shankar, and A. Bhandari, "Unlimited sampling radar: Life below the quantization noise," in *IEEE Intl. Conf. on Acoustics, Speech and Signal Processing (ICASSP)*, Jun. 2023.

[30] A. Bhandari and F. Krahmer, "HDR imaging from quantization noise," in *IEEE Intl. Conf. on Image Processing (ICIP)*, Oct. 2020, pp. 101–105.

[31] Z. Liu, A. Bhandari, and B. Clerckx, "λ–MIMO: Massive MIMO via modulo sampling," *IEEE Trans. Commun.*, pp. 6301–6315, Aug. 2023.

[32] ——, "Full-duplex beyond self-interference: The unlimited sensing way," *IEEE Commun. Lett.*, vol. 29, no. 1, pp. 165–169, Jan. 2025.

[33] O. D. Grace and S. P. Piti, "Quadrature sampling of high-frequency waveforms," *The Journal of the Acoustical Society of America*, vol. 44, no. 5, pp. 1453–1454, Nov. 1968.

[34] W. Knight, R. Pridham, and S. Kay, "Digital signal processing for sonar," *Proc. IEEE*, vol. 69, no. 11, pp. 1451–1506, Nov. 1981.

[35] W. Waters and B. Jarrett, "Bandpass signal sampling and coherent detection," *IEEE Trans. Aerosp. Electron. Syst.*, vol. AES-18, no. 6, pp. 731–736, Nov. 1982.

[36] D. Rice and K. Wu, "Quadrature sampling with high dynamic range," *IEEE Trans. Aerosp. Electron. Syst.*, vol. AES-18, no. 6, pp. 736–739, Nov. 1982.

[37] J. Kang, H. Yoon, C. Yoon, and S. Y. Emelianov, "High-frequency ultrasound imaging with sub-Nyquist sampling," *IEEE Trans. Ultrason., Ferroelectr., Freq. Control*, vol. 69, no. 6, pp. 2001–2009, Jun. 2022.

[38] A. Hirabayashi, H. Ogawa, and K. Kitagawa, "Fast surface profiler by white-light interferometry by use of a new algorithm based on sampling theory," *Applied Optics*, vol. 41, no. 23, p. 4876, Aug. 2002.

[39] K. G. Larkin, "Efficient nonlinear algorithm for envelope detection in white light interferometry," *Journal of the Optical Society of America A*, vol. 13, no. 4, p. 832, Apr. 1996.

[40] Y. Bresler, "Spectrum-blind sampling and compressive sensing for continuous-index signals," in *2008 Information Theory and Applications Workshop*. IEEE, Jan. 2008.

[41] P. Feng and Y. Bresler, "Spectrum-blind minimum-rate sampling and reconstruction of multiband signals," in *IEEE Intl. Conf. on Acoustics, Speech and Signal Processing (ICASSP)*. IEEE, May 1996.

[42] M. Mishali and Y. Eldar, "Blind multiband signal reconstruction: Compressed sensing for analog signals," *IEEE Trans. Signal Process.*, vol. 57, no. 3, pp. 993–1009, Mar. 2009.

[43] R. Venkataramani and Y. Bresler, "Perfect reconstruction formulas and bounds on aliasing error in sub-Nyquist nonuniform sampling of multiband signals," *IEEE Trans. Inf. Theory*, vol. 46, no. 6, pp. 2173–2183, Sep. 2000.

[44] B. Brannon, "Wideband radios need wide dynamic range converters," *Analog Dialogue*, vol. 29, no. 2, pp. 11–12, 1995.

[45] S. Henthorn, T. O'Farrell, M. R. Anbiyaei, and K. L. Ford, "Concurrent multiband direct RF sampling receivers," *IEEE Trans. Wireless Commun.*, vol. 22, no. 1, pp. 550–562, Jan. 2023.

[46] B. Murmann, "The race for the extra decibel: A brief review of current adc performance trajectories," *IEEE Solid-State Circuits Magazine*, vol. 7, no. 3, pp. 58–66, Sep. 2015.

[47] A. Bhandari and F. Krahmer, "On identifiability in unlimited sampling," in *Intl. Conf. on Sampling Theory and Applications (SampTA)*, Jul. 2019.

[48] A. Bhandari, F. Krahmer, and R. Raskar, "On unlimited sampling and reconstruction," *IEEE Trans. Signal Process.*, vol. 69, pp. 3827–3839, Dec. 2020.

[49] R. Guo and A. Bhandari, "Unlimited sampling of FRI signals independent of sampling rate," in *IEEE Intl. Conf. on Acoustics, Speech and Signal Processing (ICASSP)*, May 2023.

[50] A. Bhandari, "Unlimited sampling with sparse outliers: Experiments with impulsive and jump or reset noise," in *IEEE Intl. Conf. on Acoustics, Speech and Signal Processing (ICASSP)*, May 2022, pp. 5403–5407.

[51] M. Unser, "Sampling–50 years after shannon," *Proceedings of the IEEE*, vol. 88, no. 4, pp. 569–587, Apr. 2000.

[52] M. W. Hauser, "Principles of oversampling A/D conversion," *journal of the audio engineering society*, vol. 39, no. 1/2, pp. 3–26, Jan. 1991.

[53] M. Mishali and Y. C. Eldar, "From theory to practice: Sub-Nyquist sampling of sparse wideband analog signals," *IEEE J. Sel. Topics Signal Process.*, vol. 4, no. 2, pp. 375–391, Apr. 2010.

[54] A. Khilo, "Integrated photonic analog-to-digital converters," Ph.D. dissertation, Massachusetts Institute of Technology, 2011.

[55] Z. J. Towfic, S.-K. Ting, and A. H. Sayed, "Clock jitter compensation in high-rate ADC circuits," *IEEE Trans. Signal Process.*, vol. 60, no. 11, pp. 5738–5753, Jul. 2012.

[56] N. Gray, "ABCs of ADCs," *National Semiconductor Corporation, Aug*, vol. 4, 2003.

[57] A. Ng and J. Swanevelder, "Resolution in ultrasound imaging," *Continuing Education in Anaesthesia Critical Care & Pain*, vol. 11, no. 5, pp. 186–192, Oct. 2011.

[58] D. F. Filipovic and C. Komninakis, "Saturation detection for analog-to-digital converter," Feb. 2 2010, U.S. Patent 7,656,327.

[59] S.-K. Ting and A. H. Sayed, "Mitigation of clipping in sensors," in *IEEE Intl. Conf. on Acoustics, Speech and Signal Processing (ICASSP)*. IEEE, May 2013.

[60] A. J. Weinstein and M. B. Wakin, "Recovering a clipped signal in sparseland," *Sampling Theory in Signal and Image Processing*, vol. 12, no. 1, pp. 55–69, Jan. 2013.

[61] Z. Chen, M. Soozande, H. J. Vos, J. G. Bosch, M. D. Verweij, N. de Jong, and M. A. P. Pertijs, "Impact of bit errors in digitized RF data on ultrasound image quality," *IEEE Trans. Ultrason., Ferroelectr., Freq. Control*, vol. 67, no. 1, pp. 13–24, Jan. 2020.

[62] M. Martone, N. Gollin, P. Rizzoli, and G. Krieger, "Performance-optimized quantization for SAR and InSAR applications," *IEEE Trans. Geosci. Remote Sens.*, vol. 60, pp. 1–22, Jun. 2022.

[63] R. Gray and D. Neuhoff, "Quantization," *IEEE Trans. Inf. Theory*, vol. 44, no. 6, pp. 2325–2383, 1998.

[64] M. Verhelst and A. Bahai, "Where analog meets digital: Analog-to-information conversion and beyond," *IEEE Solid-State Circuits Magazine*, vol. 7, no. 3, pp. 67–80, Sep. 2015.

[65] D. Akos, M. Stockmaster, J. Tsui, and J. Caschera, "Direct bandpass sampling of multiple distinct RF signals," *IEEE Trans. Commun.*, vol. 47, no. 7, pp. 983–988, Jul. 1999.

[66] C.-H. Tseng and S.-C. Chou, "Direct downconversion of multiband RF signals using bandpass sampling," *IEEE Trans. Wireless Commun.*, vol. 5, no. 1, pp. 72–76, Jan. 2006.

[67] J. A. Tropp, J. N. Laska, M. F. Duarte, J. K. Romberg, and R. G. Baraniuk, "Beyond Nyquist: Efficient sampling of sparse bandlimited signals," *IEEE Trans. Inf. Theory*, vol. 56, no. 1, pp. 520–544, Jan. 2010.

[68] A. Coulson, "A generalization of nonuniform bandpass sampling," *IEEE Trans. Signal Process.*, vol. 43, no. 3, pp. 694–704, Mar. 1995.

[69] C. Fazi and P. G. Neudeck, "Wide dynamic range RF mixers using wide-bandgap semiconductors," in *IEEE MTT-S International Microwave Symposium Digest*. IEEE, 1997.

[70] K. Ho, Y. Chan, and R. Inkol, "A digital quadrature demodulation system," *IEEE Trans. Aerosp. Electron. Syst.*, vol. 32, no. 4, pp. 1218–1227, Oct. 1996.

[71] Y.-P. Lin and P. Vaidyanathan, "Periodically nonuniform sampling of bandpass signals," *IEEE Transactions on Circuits and Systems II: Analog and Digital Signal Processing*, vol. 45, no. 3, pp. 340–351, Mar. 1998.

[72] R. Vaughan, N. Scott, and D. White, "The theory of bandpass sampling," *IEEE Trans. Signal Process.*, vol. 39, no. 9, pp. 1973–1984, 1991.

[73] M. Wahab and B. C. Levy, "Direct complex envelope sampling of bandpass signals with M-channel time-interleaved ADCs," *IEEE Trans. Signal Process.*, vol. 70, pp. 4804–4819, Oct. 2022.

[74] H. J. Landau, "On the recovery of a band-limited signal, after instantaneous companding and subsequent band limiting," *Bell System Technical Journal*, vol. 39, no. 2, pp. 351–364, Mar. 1960.

[75] A. Papoulis, "Generalized sampling expansion," *IEEE Trans. Circuits Syst.*, vol. 24, no. 11, pp. 652–654, Nov. 1977.

[76] A. Bhandari, A. Kadambi, and R. Raskar, *Computational Imaging*, 1st ed. MIT Press, Oct. 2022, OA URL: https://imagingtext.github.io/.

[77] E. Romanov and O. Ordentlich, "Above the Nyquist rate, modulo folding does not hurt," *IEEE Signal Process. Lett.*, vol. 26, no. 8, pp. 1167–1171, Aug. 2019.

[78] R. Guo, Y. Zhu, and A. Bhandari, "Sub-Nyquist USF spectral estimation: K frequencies with $6K + 4$ modulo samples," *IEEE Trans. Signal Process.*, vol. 72, pp. 5065–5076, Sep. 2024.

[79] A. Bhandari, F. Krahmer, and R. Raskar, "Unlimited sampling of sparse signals," in *IEEE Intl. Conf. on Acoustics, Speech and Signal Processing (ICASSP)*, Apr. 2018.

[80] O. Graf, A. Bhandari, and F. Krahmer, "One-bit unlimited sampling," in *IEEE Intl. Conf. on Acoustics, Speech and Signal Processing (ICASSP)*, May 2019, pp. 5102–5106.

[81] A. Bhandari, F. Krahmer, and R. Raskar, "Unlimited sampling of sparse sinusoidal mixtures," in *IEEE Intl. Sym. on Information Theory (ISIT)*, Jun. 2018.

[82] L. Gan and H. Liu, "High dynamic range sensing using multi-channel modulo samplers," in *2020 IEEE 11th Sensor Array and Multichannel Signal Processing Workshop (SAM)*. IEEE, Jun. 2020, pp. 1–5.

[83] D. Florescu and A. Bhandari, "Unlimited sampling with local averages," in *IEEE Intl. Conf. on Acoustics, Speech and Signal Processing (ICASSP)*, May 2022, pp. 5742–5746.

[84] D. Florescu, F. Krahmer, and A. Bhandari, "Event-driven modulo sampling," in *IEEE Intl. Conf. on Acoustics, Speech and Signal Processing (ICASSP)*, Jun. 2021.

[85] D. Florescu and A. Bhandari, "Modulo event-driven sampling: System identification and hardware experiments," in *IEEE Intl. Conf. on Acoustics, Speech and Signal Processing (ICASSP)*, May 2022, pp. 5747–5751.

[86] S. Fernández-Menduiña, F. Krahmer, G. Leus, and A. Bhandari, "Computational array signal processing via modulo non-linearities," *IEEE Trans. Signal Process.*, vol. 70, pp. 2168–2179, Jul. 2021.

[87] T. Feuillen, M. Alaee-Kerahroodi, A. Bhandari, B. S. M. R, and B. Ottersten, "Unlimited sampling for FMCW radars: A proof of concept," in *IEEE Radar Conf. (RadarConf22)*, Mar. 2022.

[88] L. Weiss and R. N. McDonough, "Prony's method,Z-Transforms, and padé approximation," *SIAM Review*, vol. 5, no. 2, pp. 145–149, Apr. 1963.

[89] T. Sarkar and O. Pereira, "Using the matrix pencil method to estimate the parameters of a sum of complex exponentials," *IEEE Antennas and Propagation Magazine*, vol. 37, no. 1, pp. 48–55, Feb. 1995.

[90] A. Bhandari, "Back in the US-SR: Unlimited sampling and sparse super-resolution with its hardware validation," *IEEE Signal Process. Lett.*, vol. 29, pp. 1047–1051, Mar. 2022.

[91] B. E. Boser and B. A. Wooley, "The design of sigma-delta modulation analog-to-digital converters," *IEEE Journal of solid-state circuits*, vol. 23, no. 6, pp. 1298–1308, 2002.

[92] M. S. Kappes, "A 2.2-mW CMOS bandpass continuous-time multibit Δ-Σ ADC with 68 dB of dynamic range and 1-MHz bandwidth for wireless applications," *IEEE J. Solid-State Circuits*, vol. 38, no. 7, Jul. 2003.

[93] H.-M. Seo, C.-G. Woo, and P. Choi, "Relationship between ADC performance and requirements of digital-IF receiver for WCDMA base-station," *IEEE Trans. Veh. Technol.*, vol. 52, no. 5, pp. 1398–1408, Sep. 2003.

[94] G. Shtendel, D. Florescu, and A. Bhandari, "Unlimited sampling of bandpass signals: Computational demodulation via undersampling," *IEEE Trans. Signal Process.*, vol. 71, pp. 4134–4145, Nov. 2023.

[95] M. B. Pursley, "Analog communications," in *Reference Data for Engineers*. Elsevier, 2002, pp. 23–1–23–19.

[96] G. Shtendel and A. Bhandari, "HDR-ToF: HDR time-of-flight imaging via modulo acquisition," in *IEEE Intl. Conf. on Image Processing (ICIP)*, Oct. 2022, pp. 3808–3812.

[97] C. Herley and P. W. Wong, "Minimum rate sampling and reconstruction of signals with arbitrary frequency support," *IEEE Trans. Inf. Theory*, vol. 45, no. 5, pp. 1555–1564, Jul. 1999.

[98] M. Rasti, S. K. Taskou, H. Tabassum, and E. Hossain, "Evolution toward 6G multi-band wireless networks: A resource management perspective," *IEEE Wireless Commun.*, vol. 29, no. 4, pp. 118–125, Aug. 2022.

[99] M. Susloparov, A. Krasilov, and E. Khorov, "Boosting XR capacity with multi-band multi-connectivity in 5G systems," *IEEE Commun. Lett.*, vol. 28, no. 9, pp. 2211–2215, Sep. 2024.

[100] R. Guo, G. Shtendel, and A. Bhandari, "Multiband unlimited sampling: Super-Nyquist or sub-Nyquist, that is the question!" in *IEEE Intl. Conf. on Acoustics, Speech and Signal Processing (ICASSP)*. IEEE, Apr. 2025, pp. 1–5.

[101] K. Gröchenig and H. Razafinjatovo, "On landau's necessary density conditions for sampling and interpolation of band-limited functions," *Journal of the London Mathematical Society*, vol. 54, no. 3, pp. 557–565, Dec. 1996.

[102] G. Shtendel and A. Bhandari, "Dual-channel unlimited sampling for bandpass signals," in *IEEE Intl. Conf. on Acoustics, Speech and Signal Processing (ICASSP)*. IEEE, Apr. 2024.

[103] A. Velten, T. Willwacher, O. Gupta, A. Veeraraghavan, M. G. Bawendi, and R. Raskar, "Recovering three-dimensional shape around a corner using ultrafast time-of-flight imaging," *Nature Communications*, vol. 3, no. 1, Jan. 2012.

[104] A. Kadambi, R. Whyte, A. Bhandari, L. Streeter, C. Barsi, A. Dorrington, and R. Raskar, "Coded time-of-flight cameras: Sparse deconvolution to address multipath interference and recover time profiles," *ACM Transactions on Graphics*, vol. 32, no. 6, pp. 1–10, Nov. 2013. [Online]. Available: http://dx.doi.org/10.1145/2508363.2508428

[105] A. Kirmani, D. Venkatraman, D. Shin, A. Colaço, F. N. C. Wong, J. H. Shapiro, and V. K. Goyal, "First-photon imaging," *Science*, vol. 343, no. 6166, pp. 58–61, Jan. 2014.

[106] A. Bhandari and R. Raskar, "Signal processing for Time-of-Flight imaging sensors: An introduction to inverse problems in computational 3-D imaging," *IEEE Signal Process. Mag.*, vol. 33, no. 5, pp. 45–58, Sep. 2016.

[107] F. Heide, L. Xiao, W. Heidrich, and M. B. Hullin, "Diffuse mirrors: 3D reconstruction from diffuse indirect illumination using inexpensive time-of-flight sensors," in *Proc. of IEEE Conf. on Comp. Vis. and Patt. Rec. (CVPR)*, 2014, pp. 3222–3229.

[108] A. Bhandari, C. Barsi, and R. Raskar, "Blind and reference-free fluorescence lifetime estimation via consumer time-of-flight sensors," *Optica*, vol. 2, no. 11, p. 965, Nov. 2015. [Online]. Available: http://dx.doi.org/10.1364/OPTICA.2.000965

[109] W. Kazmi, S. Foix, G. Alenyà, and H. J. Andersen, "Indoor and outdoor depth imaging of leaves with time-of-flight and stereo vision sensors: Analysis and comparison," *ISPRS Journal of Photogrammetry and Remote Sensing*, vol. 88, pp. 128–146, Feb. 2014.

[110] H. Gao, B. Cheng, J. Wang, K. Li, J. Zhao, and D. Li, "Object classification using CNN-based fusion of vision and LIDAR in autonomous vehicle environment," *IEEE Trans. Ind. Informat.*, vol. 14, no. 9, pp. 4224–4231, Sep. 2018.

[111] M. H. Conde, K. Hartmann, and O. Loffeld, "Adaptive high dynamic range for time-of-flight cameras," *IEEE Trans. Instrum. Meas.*, vol. 64, no. 7, pp. 1885–1906, Jul. 2015.

[112] J. Zhu, L. Wang, R. Yang, and J. Davis, "Fusion of time-of-flight depth and stereo for high accuracy depth maps," in *IEEE Conf. on Comp. Vis. and Pat. Recognition (CVPR)*, Jun. 2008.

[113] H.-Y. Lin and W.-Z. Chang, "High dynamic range imaging for stereoscopic scene representation," in *IEEE Intl. Conf. on Image Processing (ICIP)*, Nov. 2009.

[114] A. Payne, A. Daniel, A. Mehta, B. Thompson, and C. S. Bamji, "7.6 A 512×424 CMOS 3D time-of-flight image sensor with multi-frequency photo-demodulation up to 130MHz and 2GS/s ADC," in *IEEE Intl. Solid-State Circuits Conf. Digest of Technical Papers (ISSCC)*, Feb. 2014.

[115] S. Yu, Y. Zhang, F. Zhou, W. Lu, S. Lei, and Z. Chen, "A CMOS time-of-flight image sensor with high dynamic range digital pixel," in *Intl. Conf. on ASIC (ASICON)*, Oct. 2021.

[116] A. Bhandari, A. Kadambi, R. Whyte, C. Barsi, M. Feigin, A. Dorrington, and R. Raskar, "Resolving multipath interference in time-of-flight imaging via modulation frequency diversity and sparse regularization," *Optics Letters*, vol. 39, no. 6, p. 1705, Mar. 2014.

[117] Stanford University Computer Graphics Laboratory, "The Stanford 3D Scanning Repository," [Online] http://graphics.stanford.edu/data/3Dscanrep/, 1994.

[118] R. Guo and A. Bhandari, "Spectrum blind unlimited sampling of multi-band signals," in *IEEE Intl. Conf. on Acoustics, Speech and Signal Processing (ICASSP)*. IEEE, Apr. 2025, pp. 1–5.

[119] R. Venkataramani and Y. Bresler, "Further results on spectrum blind sampling of 2d signals," in *Proceedings 1998 International Conference on Image Processing. ICIP*, vol. 2, 1998, pp. 752–756 vol.2.

[120] B. Wronski, I. Garcia-Dorado, M. Ernst, D. Kelly, M. Krainin, C.-K. Liang, M. Levoy, and P. Milanfar, "Handheld multi-frame super-resolution," *ACM Trans. Graph.*, vol. 38, no. 4, Jul. 2019. [Online]. Available: https://doi.org/10.1145/3306346.3323024

[121] D. Florescu and A. Bhandari, "Multi-dimensional unlimited sampling and robust reconstruction," *Applied and Computational Harmonic Analysis*, vol. 79, p. 101796, Oct. 2025.